N° Ordre...../FT/UMBB/2024

PEOPLES DEMOCTRATIC REPUBLIC OF ALGERIA

MINISTERY OF HIGHER EDUCATION AND SCINETIFIC REASERACH

M'HAMED BOUGARA UNIVERSITY BOUMERDES

Faculty of Technology

Doctorate Thesis

Presented by:

Khalida KHODJA

In view of obtaining the degree of **DOCTORAT - LMD** in**:**

Field: Telecommunications

Specialty: Networks and telecommunications

Contribution to the Design of New Antenna Structure more Efficient for 5G Communications Systems

Before the jury composed of :

Mr	HAMADOUCHE	M'Hamed	Professor	University of Boumerdes	Chairman
Mr	ATIA	Salim	MCA	University of BBA	Supervisor
Mr	MESSAOUDENE	Idris	MCA	University of BBA	Co-supervisor
Mr	MESSAOUDI	Noreddine	Professor	University of Boumerdes	Examiner
Mr	BAICHE	Karim	MCA	University of Boumerdes	Examiner
Mr	AIDEL	Salih	Professor	University BBA	Examiner
Mr	BELAZZOUG	Massinissa	MCB	University of BBA	Invited

Academic year 2024/2025

Abstract

This thesis explores key advancements and challenges in telecommunications and antenna design, focusing on the evolution towards 5G networks and the utilization of millimeter-wave (MMW) frequencies. The first chapter provides a comprehensive overview of 5G networks, emphasizing the unique propagation characteristics and transformative potential of MMW technology. It investigates the technological innovations required to optimize MMW spectrum for ultra-high-speed data transmission. The second chapter presents a comprehensive overview of the evolution of wave guiding techniques including their fundamental principles and common applications, detailing their historical development, advantages, and drawbacks. It traces the advancements from traditional hollow waveguides to more recent innovations designed to meet the increasing demands of high-frequency communication systems, particularly in the MMW band. It also explores the limitations of these conventional techniques that have spurred the development of novel waveguide technologies. Among the various emerging techniques, this chapter highlights the Ridge Gap Waveguide (RGW) technology as the most promising solution for MMW applications and discusses in detail its main characteristics, while displaying its key advantages. Actually, the RGW's ability to overcome many of the challenges faced by traditional waveguides are emphasized, showing that the RGW's unique ridge structure offers a significant improvement in performance and versatility, which makes it a superior candidate for next-generation communication systems. Additionally, this chapter addresses the current drawbacks of RGWs and it concludes with a critical evaluation of RGW technology in the context of its application to advanced communication network. This overview establishes a foundational understanding of wave guiding techniques and positions RGW technology as a leading candidate for addressing the demands of modern high-frequency communication systems. The third chapter introduces a novel antenna design tailored for the Ka-band frequency range, featuring both dual-band and dual-beam radiation capabilities. This dual-band functionality is realized through a carefully engineered radiating structure that accommodates the different wavelength requirements of each band, ensuring optimal performance and minimal interference. In addition to its dual-band capability, the antenna features a dual-beam radiation pattern; this design innovation allows for simultaneous coverage of two separate spatial regions, enhancing the system's flexibility and efficiency. Chapter “four” introduces a miniaturized, high-gain, and highly efficient antenna designed for operation at 60 GHz, leveraging the innovative Double Printed

Ridge Gap Waveguide (D-PRGW) technology. The proposed antenna utilizes D-PRGW technology to achieve exceptional performance while maintaining a compact size factor. This design innovation allows for a significant reduction in antenna dimensions without compromising gain or efficiency. By employing a dual-ridge configuration, the antenna effectively mitigates signal losses and enhances power handling capabilities, making it well-suited for high-frequency applications where space constraints are a major concern. The chapter provides a detailed analysis of the antenna's design, including its geometric parameters, simulation results and experimental measurements that demonstrate the antenna's excellent performance metrics, such as gain, beam width, and efficiency.

Key words: 5G, Millimeter wave antenna, Gidge Gap Waveguide, miniaturization, DRA

Résumé

Cette thèse explore les avancées et les défis clés dans le domaine de télécommunications et la conception d'antennes, en se concentrant sur l'évolution vers les réseaux 5G et l'utilisation des fréquences à ondes millimétriques (MMW). Le premier chapitre fournit un aperçu complet des réseaux 5G, en soulignant les caractéristiques de propagation uniques et le potentiel de transformation de la technologie MMW. Il étudie les innovations technologiques nécessaires pour optimiser le spectre MMW pour la transmission de données à très haut débit. Le deuxième chapitre présente un aperçu complet de l'évolution des techniques de guide d'ondes, y compris leurs principes fondamentaux et leurs applications courantes, en détaillant leur développement historique, leurs avantages et leurs inconvénients. Il retrace les avancées des guides d'ondes creux traditionnels jusqu'aux innovations plus récentes conçues pour répondre aux demandes croissantes des systèmes de communication à hautes fréquences, en particulier dans la bande MMW. Il explore également les limites de ces techniques conventionnelles qui ont stimulé le développement de nouvelles technologies de guides d'ondes. Parmi les différentes techniques émergentes, ce chapitre met en évidence la technologie Ridge Gap Waveguide (RGW) comme la solution la plus prometteuse pour les applications MMW et discute en détail de ses principales caractéristiques, tout en affichant ses principaux avantages. En fait, la capacité du RGW à surmonter de nombreux défis auxquels sont confrontés les guides d'ondes traditionnels est soulignée, montrant que la structure de crête unique du RGW offre une amélioration significative des performances et de la polyvalence, ce qui en fait un candidat supérieur pour les systèmes de communication de nouvelle génération. De plus, ce

chapitre aborde les inconvénients actuels des RGW et se termine par une évaluation critique de la technologie RGW dans le contexte de son application aux réseaux de communication avancés. Cette vue d'ensemble établit une compréhension fondamentale des techniques de guidage d'ondes et positionne la technologie RGW comme un candidat de premier plan pour répondre aux exigences des systèmes de communication haute fréquence modernes. Le troisième chapitre présente une nouvelle conception d'antenne adaptée à la gamme de fréquences de la bande Ka, dotée de capacités de rayonnement à double bande et à double faisceau. Cette fonctionnalité à double bande est réalisée grâce à une structure rayonnante soigneusement conçue qui s'adapte aux différentes exigences de longueur d'onde de chaque bande, garantissant des performances optimales et des interférences minimales. En plus de sa capacité à double bande, l'antenne présente un diagramme de rayonnement à double faisceau ; cette innovation de conception permet une couverture simultanée de deux régions spatiales distinctes, améliorant ainsi la flexibilité et l'efficacité du système. Le chapitre « quatre » présente une antenne miniaturisée, à gain élevé et à haut rendement, conçue pour fonctionner à 60 GHz, exploitant la technologie innovante D-PRGW (Double Printed Ridge Gap Waveguide). L'antenne proposée utilise la technologie D-PRGW pour atteindre des performances exceptionnelles tout en conservant un facteur de taille compact. Cette innovation de conception permet une réduction significative des dimensions de l'antenne sans compromettre le gain ou l'efficacité. En utilisant une configuration à double crête, l'antenne atténue efficacement les pertes de signal et améliore les capacités de gestion de la puissance, ce qui la rend bien adaptée aux applications haute fréquence où les contraintes d'espace sont une préoccupation majeure. Le chapitre fournit une analyse détaillée de la conception de l'antenne, y compris ses paramètres géométriques, les résultats de simulation et les mesures expérimentales qui démontrent les excellentes mesures de performance de l'antenne, telles que le gain, la largeur du faisceau et l'efficacité.

Mots clés : 5G, Antenne à ondes millimétriques, Guide d'ondes Gidge Gap, miniaturisation, DRA

ملخص

يستكشف هذا البحث التطورات والتحديات الرئيسية في مجال الاتصالات وتصميم الهوائيات، مع التركيز على التطور نحو شبكات الجيل الخامس واستخدام ترددات الموجات المليمترية. يقدم الفصل الأول نظرة عامة شاملة على شبكات الجيل الخامس، مع التركيز على خصائص الانتشار الفريدة والإمكانات التحويلية لتكنولوجيا الموجات المليمترية. كما يبحث في الابتكارات التكنولوجية المطلوبة لتحسين طيف الموجات المليمترية لنقل البيانات بسرعة فائقة. يقدم الفصل الثاني نظرة

عامة شاملة على تطور تقنيات توجيه الموجات بما في ذلك مبادئها الأساسية وتطبيقاتها الشائعة، مع تفصيل تطورها التاريخي ومزاياها وعيوبها. ويتتبع التقدم من الموجهات المجوفة التقليدية إلى الابتكارات الأحدث المصممة لتلبية المتطلبات المتزايدة لأنظمة الاتصالات عالية التردد، وخاصة في نطاق الموجات المليمترية. كما يستكشف قيود هذه التقنيات التقليدية التي حفزت تطوير تقنيات الموجات الجديدة. من بين التقنيات الناشئة المختلفة، يسلط هذا الفصل الضوء على تقنية Ridge Gap Waveguide (RGW) باعتبارها الحل الأكثر وعدًا لتطبيقات الموجات الدقيقة ويناقش بالتفصيل خصائصها ، مع عرض مزاياها الرئيسية. كما يتم التأكيد على العديد من التحديات التي تواجهها الموجهات الموجية التقليدية، مما يدل على أن البنية الفريدة لـ RGW تقدم تحسنًا كبيرًا في الأداء والتنوع، مما يجعلها مرشحًا متفوقًا لأنظمة الاتصالات من الجيل التالي. بالإضافة إلى ذلك، يتناول هذا الفصل العيوب الحالية لـ RGW ويختتم بتقييم نقدي لتقنية RGW في سياق تطبيقها على شبكة الاتصالات المتقدمة. تؤسس هذه النظرة العامة فهمًا أساسيًا لتقنيات توجيه الموجة وتضع تقنية RGW كمرشح رائد لتلبية متطلبات أنظمة الاتصالات الحديثة عالية التردد. يقدم الفصل الثالث تصميمًا جديدًا للهوائي مصممًا خصيصًا لنطاق ترددKa-band ، يتميز بقدرات إشعاع ثنائية النطاق وثنائية الحزمة. يتم تحقيق هذه الوظيفة ذات النطاق المزدوج من خلال هيكل إشعاعي مصمم بعناية يستوعب متطلبات الطول الموجي المختلفة لكل نطاق، مما يضمن الأداء الأمثل والحد الأدنى من التداخل. بالإضافة إلى قدرته على الإشعاع في النطاق المزدوج، يتميز الهوائي بنمط إشعاع ثنائي الشعاع؛ يسمح هذا الابتكار في التصميم بتغطية متزامنة لمنطقتين مكانيتين منفصلتين، مما يعزز مرونة النظام وكفاءته. يقدم الفصل "الرابع" هوائيًا مصغرًا وعالي الكسب وعالي الكفاءة مصممًا للعمل عند 60 جيجاهرتز، مستفيدًا من تقنية Double Printed Ridge Gap Waveguide (D-PRGW) المبتكرة. يستخدم الهوائي المقترح تقنية D-PRGW لتحقيق أداء استثنائي مع الحفاظ على عامل الحجم الصغير. يسمح هذا الابتكار في التصميم بخفض كبير في أبعاد الهوائي دون المساس بالكسب أو الكفاءة. من خلال استخدام تكوين مزدوج ، يخفف الهوائي بشكل فعال من خسائر الإشارة ويعزز قدرات التعامل مع الطاقة، مما يجعله مناسبًا تمامًا للتطبيقات عالية التردد حيث تكون قيود المساحة مصدر قلق كبير. يقدم الفصل تحليلاً مفصلاً لتصميم الهوائي، بما في ذلك معلماته الهندسية ونتائج المحاكاة والقياسات التجريبية التي توضح مقاييس الأداء الممتازة للهوائي، مثل المكسب وعرض الشعاع والكفاءة.

الكلمات الرئيسية: 5G، هوائي الموجة المليمترية، موجه الموجات Gidge Gap، التصغير، DRA

Acknowledgment

I would like to express my profound gratitude to “ALLAH”, whose guidance and blessings have been the cornerstone of my journey. His holey presence has provided me with strength, wisdom, and resilience, allowing me to overcome challenges and achieve my goals. I am deeply thankful for the grace and support that have illuminated my path.

To my family and friends, your unwavering support and encouragement have been invaluable. Your belief in me, along with your constant love and motivation, has been a source of immense strength. I am incredibly grateful for your presence in my life, as it has helped me persevere through difficult times and celebrate the successes along the way.

I also wish to extend my heartfelt thanks to my supervisors and co-authors. Your guidance, insightful feedback, and dedication have been instrumental in shaping my academic and professional growth. Your mentorship has provided me with the tools and knowledge needed to excel, and I am sincerely appreciative of the time and effort you have invested in my development. Your support has been crucial to my achievements, and I am deeply grateful for your commitment.

Table Contents

List of figures

List of tables

List of Symbols

$\boldsymbol{Pr}$	Radiated power
$\boldsymbol{G_r}$	Receiver gain
$\boldsymbol{G_T}$	Transmitter gain
$\boldsymbol{P_T}$	Transmitted power
$\boldsymbol{W_e}$	Stored energy
$\boldsymbol{\eta}$	Radiation efficiency
$\boldsymbol{P_{dis}}$	Dissipated power
$\boldsymbol{D}$	Directivity
$\boldsymbol{G}$	Gain
$\boldsymbol{L_{fs}}$	Free space loss
$\boldsymbol{d}$	Link distance
$\boldsymbol{\lambda}$	Wavelength
$\boldsymbol{\varepsilon_r}$	Dielectric constant of the material
$\boldsymbol{f}$	Frequency of the signal
$\boldsymbol{f_c}$	Cut-off frequency
$\boldsymbol{f_r}$	Resonant frequency
$\boldsymbol{Q}$	Quality factor
$\boldsymbol{Q_{rad}}$	Radiation *Q* factor
$\boldsymbol{Q_{dis}}$	Dissipation *Q* factor
$\boldsymbol{S}$	Complex Poynting vector at the Surface
$\hat{\boldsymbol{t}}$	Tangential vector
$\hat{\boldsymbol{l}}$	Longitudinal vector
$\hat{\boldsymbol{n}}$	Surface normal
$\boldsymbol{E}$	Electric field
$\boldsymbol{E_t}$	Tangential component of E-field
$\boldsymbol{E_l}$	Longitudinal component of E-Field
$\boldsymbol{E_n}$	Normal component of E-field
$\boldsymbol{H}$	Magnetic field
$\boldsymbol{H_t}$	Tangential component of H-field
$\boldsymbol{H_l}$	Longitudinal component of H-field
$\boldsymbol{H^*}$	Complex conjugate of H-field
$\boldsymbol{Z_s}$	Surface impedance

Z_t	Tangential component of impedance
Z_l	Longitudinal component of impedance
r	Radius
$\bar{\bar{\varepsilon}}$	Permittivity tensor
q_z	Z-component of the wave vector q
k	Propagation constant
k_p	Plasma wave number accounting for the local spatial dispersion
η_0	Intrinsic impedance at free space
β_h	Wave number in the host material
β	Wavenumber in free space
k_y	Propagation constant in y-direction
d	Height of the conducting pins
h	Height of the air gap
W_{eff}	Effective propagation width
p	Periodicity
Γ	Reflection coefficient
$VSWR$	Voltage Standing Wave Ratio

List of Acronyms

AMC	Artificial Magnetic Conductor
BW	Band Width
CDMA	Code Division Multiple Access
CPW	Coplanar Waveguide
CST	Computer Simulation Technology
D-PRGW	Double Printed Ridge Gap Waveguide
DRA	Dielectric Resonator Antenna
EM	Electro Magnetic
EBG	Electromagnetic Band-Gap
EHF	Extremely High Frequency
FCC	Federal Communications Commission
FM	Frequency Modulation
FPC	Fabry Perot Cavity
FSS	Frequency Selective Surfaces
GCPW	Grounded Coplanar Waveguide
GGW	Groove Gap Waveguide
GPS	Global Positioning System
GW	Gap Waveguide
HFSS	High Frequency Structure Simulator
HIS	High Impedance Surface
HP	Horizontal Polarization
HSPA	High Speed Packet Access
IMGW	Inverted Microstrip Gap Waveguide
IMT	International Mobile Telecommunication
IoT	Internet of Things
ISM	Industrial Scientific and Medical
ITU	International Telecommunication Union
LMDS	Local Multipoint Distribution System
LTE	Long Term Evolution
LWA	Leaky Wave Antenna
ME	Magneto Electric
mGbit	Multi Gigabit
MIMO	Multiple Input Multiple Output
MGW	Microstrip Gap Wavgeguide
MMW	Milli-Meter Wave

NLOS	Non-Line-Of-Sight
NRD	Non-Radiative Dielectric
OFDM	Orthogonal Frequency Division Multiplexing
PBG	Photonic Band Gap
PCB	Printed Circuit Board
PEC	Perfect Electric Conductor
PhC	Photonic Crystals
PLWA	Periodic Leaky Wave Antenna
PMC	Perfect Magnetic Conductor
PPHC	Peak Power Handling Capability
PPWG	Parallel Plate waveguide
PRGW	Printed Ridge Gap Waveguide
RF	Radio Frequency
RGW	Ridge Gap Waveguide
SIW	Substrate Integrated Waveguide
SMS	Short Message Service
SoC	System on Chip
TDMA	Time Division Multiple Access
TDRA	Triangular Dielectric Resonator Antenna
TE	Transverse Electric
TEM	Transverse Electromagnetic
TM	Transverse Magnetic
UHD	Ultra High Definition
UHF	Ultra High Frequency
VHF	Very High Frequency
VP	Vertical Polarization
VR	Virtual Reality
VSWR	Voltage Standing Wave Ratio
WCDMA	Wide bande Code Division Multiple Access
WiGig	Wireless Gigabit
WLAN	Wireless Local Area Network
1G	1st Generation
2G	2nd generation
3G	3rd generation
4G	4th generation
5G	5th generation

CHAPTER 1: GENERAL INTRODUCTION

1.1 Evolution of mobile communication

Each new generation of mobile wireless networks brings advancements in speed and functionality, significantly enhancing our smartphones beyond what previous generations offered. The journey began in the 1970s when Bell Labs pioneered a cellular system and established the first commercially viable standards. This innovation set the stage for the evolution of mobile communication. In the 1980s, the demand for more versatile and commercial applications spurred the deployment of the first generation (1G) of wireless networks. Introduced in 1980, 1G was primarily designed for voice communication and utilized analog Frequency Modulation (FM) technology [1]. This initial technology allowed for the first portable cell phones but offered much limited functionalities compared to what we have today. Ever since, the wireless communication systems have experienced an outstanding progressive revolution [2], [3].The 1990s saw the introduction of the second generation (2G) networks, which marked a significant leap forward. 2G networks improved spectral efficiency and introduced digital modulation techniques, such as Time Division Multiple Access (TDMA) and Code Division Multiple Access (CDMA). This advancement enabled data services with speeds up to 64 kbps and introduced features such as Short Message Service (SMS), conference calls, and call holding.

The early 2000s ushered in the third generation (3G) networks, which revolutionized mobile communication by providing high-speed data transmission. This era marked the beginning of mobile internet for the first time, allowing users to stream videos and audio with unprecedented ease. Technologies like Wideband Code Division Multiple Access (WCDMA) and High-Speed Packet Access (HSPA) facilitated these advancements, offering a substantial upgrade in both speed and functionality.

The 4^{th} generation (4G) mobile communication systems [4], till date, provide a significant upgrade over their predecessors. They have been designed to meet the requirements of wireless standards such as IEEE 802.16m and Long Term Evolution (LTE) advanced radio access requirements along with International Mobile Telecommunication (IMT) advanced technology to deliver the speed that we enjoy today based on Orthogonal Frequency Division

Multiplexing (OFDM) [5]. The 4G offers a Band Width (BW) up to 20 MHz with download speed of 100 Mbps. It also supports Multiple Input Multiple Output (MIMO) technology, which enables 4G systems to work with massive data transmission rates, high spectral efficiency, improved link quality, radio broadcasting and adapted radiation patterns for signal gain and interference.

Throughout this development journey [6] illustrated in Figure 1-1, the technological advancement surged to meet the high dynamic needs of consumers, while mobile communications anticipated to transition to 5G within 2020 [7]. However, the influx of new users has strained these networks, pushing them to their limits due to the escalating demand for increased data capacity.

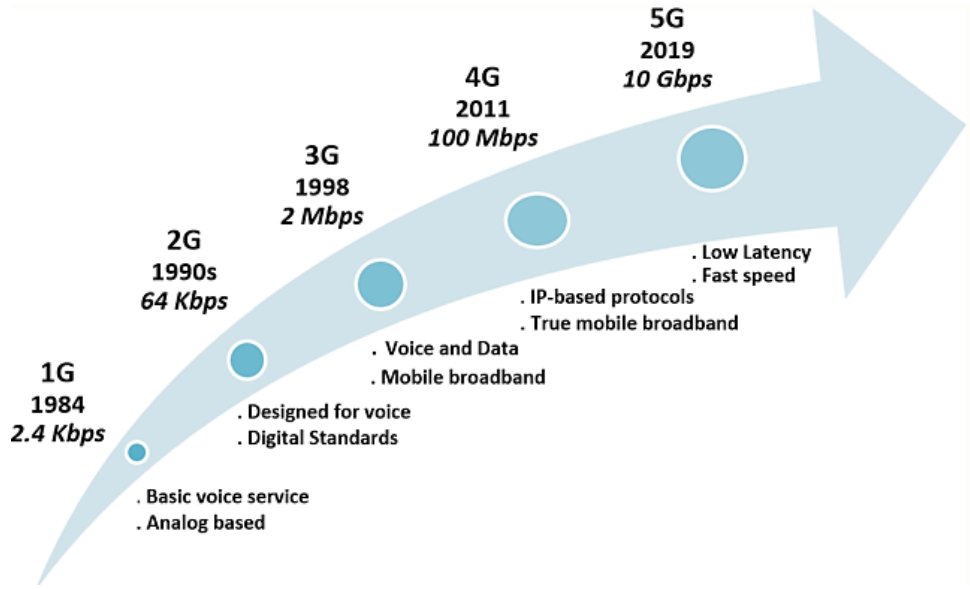

Figure 1-1 Evolution of mobile communication systems.

Nowadays, we are heading to the next future generation (5G) [8], which is expected to add more services over 4G in order to compensate for the drawbacks in the former generations, hold up the increasing number of users, and solve the growing need for higher transmission rates. Besides, it supports the BW's limitations [9] by delivering more reliable services via ultra-dense radio networking with self-backhauling, mesh-like connectivity, lower outage probability, much higher transmission bit rates in a large portion of the coverage area (>1Gbps for wireless transmission of the uncompressed high-definition video image) with lower latency, lower infrastructure cost, and more efficient spectrum reuse [10].

From the other side, the specific allocated spectrum for service providers of our mobiles and electronic devices from the International Telecommunication Union (ITU) falls typically under 6 GHz "High Frequency (HF) (3MHz to 30MHz), Very High Frequency (VHF)

(30MHz to 300MHz) and Ultra-High Frequency (UHF) (300MHz to 3GHz)". Adopting these frequency bands allows less propagation and attenuation losses and thus, long distance coverage can be assured. These bands are fragmented into disjoint frequency sub-bands with relatively limited carrier frequency BW (ranging between 700 MHz and 2.6 GHz), having different radio networks and different propagation characteristics for each technology operating within this range such as Global Positioning System (GPS), Wi-Fi, 3G, 4G, L, S and C band satellite communications … etc. So far, the 4G supports a BW up to 20 MHz. However, nowadays, mobile phones and wireless systems can be found everywhere, and as more devices come on line, these sub-bands are starting to get crowded, which would provide slower services and more dropped connections. This means that the conventional frequency bands and wireless systems will not be able to face the tremendous growth of consumers' demands. As a result, the focus of future technology is on data capacity and speed rate rather than coverage, where many users can utilize a large amount of capacity simultaneously and efficiently.

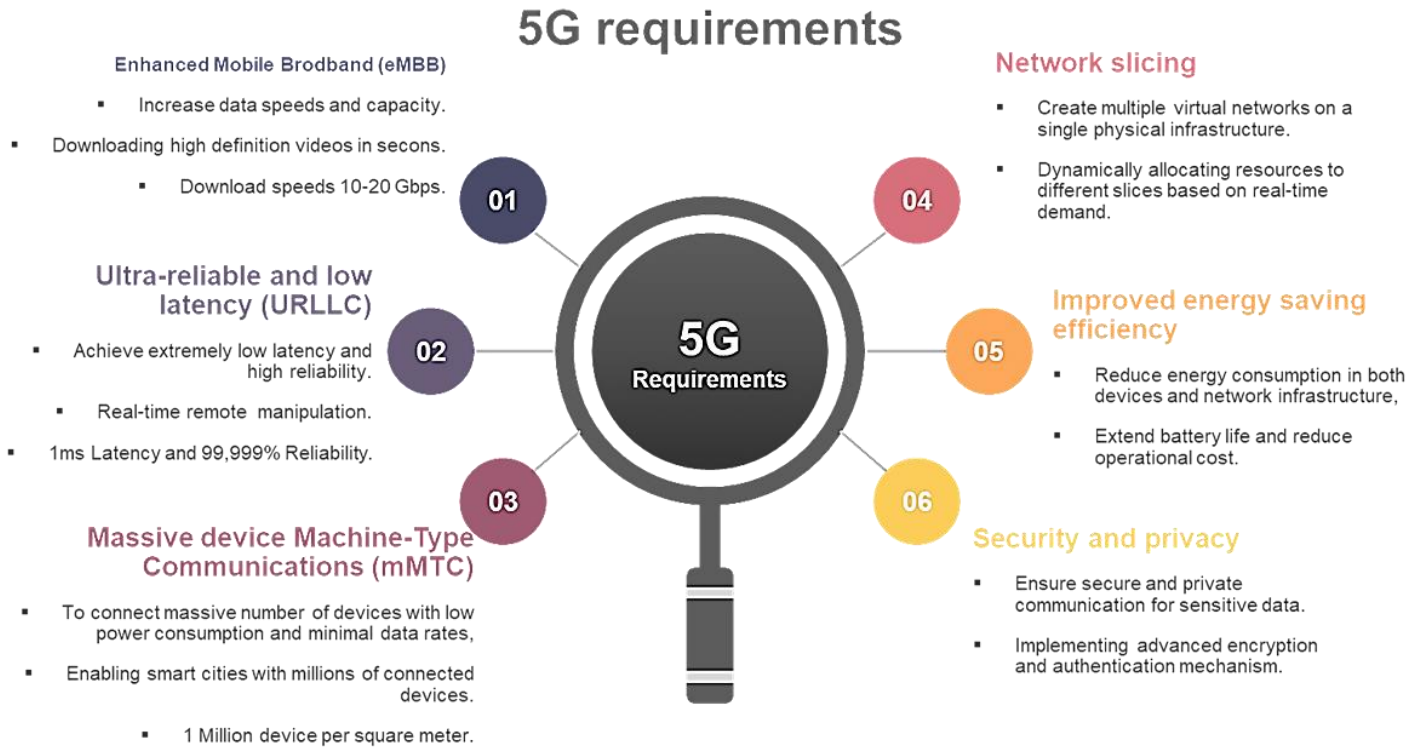

Figure 1-2 The 5G major requirements.

Among the highly anticipated solutions to meet the requirements of the upcoming 5G [11], depicted in Figure 1.2, is to go beyond the 6GHz frequency band and exploit a new frequency territory ranging from 30 GHz to 300 GHz. This is commonly referred to as Milli-Meter

Wave (MMW) or Extremely High Frequency (EHF), which presents a solution for disjoint frequency bands in the current wireless networks. The allocated frequency spectrum is depicted in Figure 1.3 and a detailed discussion on MMW sub bands will be given in the following section.

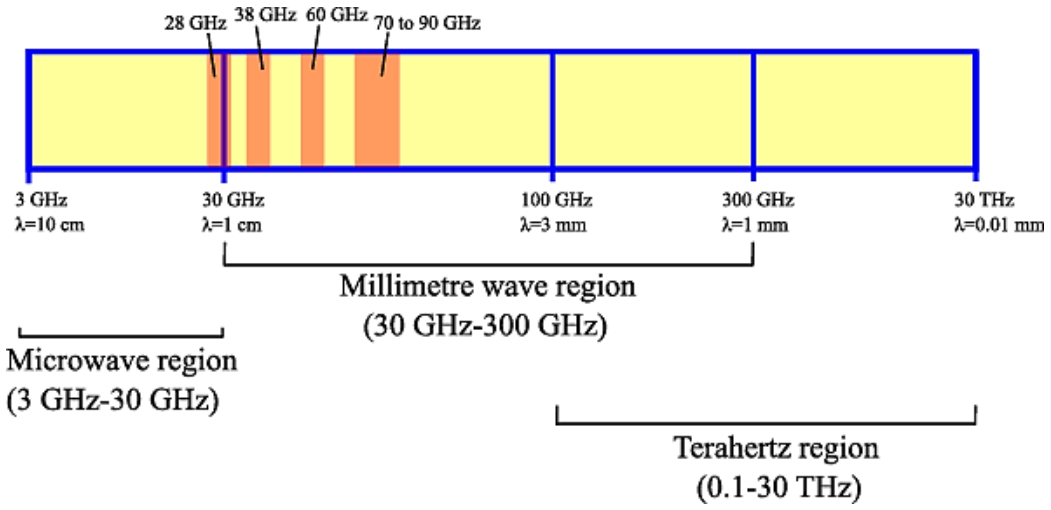

Figure 1-3 MMW band frequency spectrum.

1.2 MMW bands advantages

The unexploited MMW region occupies the range of frequency spectrum between 30 GHz and 300 GHz, which corresponds to wavelengths of from 10 to 1mm. This band is considered as a potential candidate for the upcoming 5G communication system as it supports a massive amount of unlicensed windows and provides several advantages to MMW communications including:

1. Low profile and single chip integration, since at this frequency range the guided wavelength is relatively short, resulting in planar and smaller physical dimensions of components with low insertion loss, due to the achieved compactness concerning the antenna size and integrated parts packaging, which is also crucial in low profile circuits' integration [12].
2. Extremely high transmission data rates with high security over unlicensed and exploited bands that offers low interference and high level of frequency re-use [13].
3. Much wider BW, which is mandatory for higher data transmission. In effect, the MMW frequency range helps to expand channel BWs, permitting allocation of the increasing number of services, and, thus, rising the data capacity, which solves the data congestion issue, especially for multi-Gigabit (mGbit) wireless communications.

This will also help to minimize both the cost and dimension of the system as well as its ability of minimum power consumption [14].

4. Narrow beam width, which can be obtained at this frequency spectrum. This latter can be well suited for short distance date exchange and networks topologies such as point-to-point mesh, a dense hub, spoke or even a ring. However, this still can lead to a problem in target search and acquisition, which makes MMW bands not suitable for large volume search applications [15].
5. Possibility to exploit many techniques such as a polarization converter, Frequency Selective Surfaces (FSS), metamaterials, and new spatial techniques like massive MIMO, adaptive beamforming [16], directional antennas, inherently steerable antenna arrays, higher bit rates covering larger areas, and lower infrastructure costs [9].
6. The fact that the propagation nature of MMW band is considered non-ionizing radiation, which makes the band potentially useful and safe for human and body tissue scanning.

1.3 MMW bands impairments

The MMW band has been largely ignored for wireless networks due to some concerns about drawbacks of its propagation characteristics. Usually, wireless communications systems must execute the three following stages:

- Transmission: a low frequency signal is modulated with a high frequency carrier signal and transmitted through the antenna into the space.
- Propagation: in space, the signal is propagated in the form of EM waves. At this stage, the signal can be perturbed from atmospheric conditions or other obstacles on the way and results in high losses, as there is an increase in the frequency.
- Reception: at the final stage, the signal is received and demodulated at the receiver side and the entire wireless communication process is carried out in a similar way. This implies that migrating the operating MMW frequencies will require new front-end designs for the antenna stage and feeding structures. The current focus of microwave engineers is to implement efficient microwave components and feeding structures with high-performance metrics.

Hence, enabling MMW band in 5G would require overcoming this band's impairments [17] which consist mainly of:

1.3.1 Free space path loss

Free space path loss refers to the loss in signal strength as Electro Magnetic (EM) waves propagate through the air or free space without any obstacles or reflecting surfaces. It occurs primarily due to the spreading of the signal as it expands outward from the transmitting antenna. The path loss factor in free space is directly proportional to the squared distance between the transmitter and receiver and to the squared operating frequency of the signal. According to the transmission equation formula of Friis, the received power (P_r) for a practical wireless link may be expressed as follows [18]

$$P_r[dBm] = P_T[dBm] + G_R[dB] + G_T[dB] - L_{fs}\,[dB] \quad 1.1$$

Where

$$L_{fs} = 20log_{10}\left(\frac{4\pi df}{c}\right) \quad 1.2$$

Where G_R and G_T are the receiver and transmitter gains, respectively, and P_T is the transmitted power. The last term represents the free space path loss (L_{fs}) in decibels which depends only upon the link distance d and the frequency of the signal f. It is obvious that at the MMW band, the free space path loss is highly considerable with the increase of frequency, which will drastically perturb the signal even at short distances. For this reason, MMW systems were mainly beneficial for short, mid-range, and outdoor point-to-point links with high directive antennas because of the short range of the propagating distance.

1.3.2 Conduction loss

Conduction loss at MMW bands refers to the phenomenon where EM waves encounter significant attenuation and degradation as they interact with conductive materials such as metals. This interaction occurs through several mechanisms: absorption, reflection, and surface wave propagation along the conductive surface. The absorption results in the conversion of EM energy into heat within the material, thereby reducing the signal strength. Whereas, reflection occurs when the incident wave strikes a conductive surface, causing a portion of the energy to bounce back leading to potentially multipath interference and signal cancellation in certain scenarios. Finally, surface wave propagation, which is more severe at higher frequencies, involves the EM field propagating along the metal surface, resulting in additional attenuation. In dense urban environments or areas with numerous metallic structures like buildings, vehicles, and infrastructures, conduction loss can severely limit the reach and reliability of MMW communications.

Furthermore, the antenna size is inversely proportional to its operating frequency, and at high frequencies the dimensions get narrower. As a result, the current density will increase and the higher the current density, the larger is the conductor loss.

1.3.3 Atmospheric absorption and rain loss

At MMW bands, atmospheric absorption and rain loss effects impact significantly signal propagation and reliability where only a specific part of the spectrum is suitable for wireless transmission. This is attributed to the atmospheric absorption level being small in the so-called atmospheric windows [19].

In outdoor environment, MMWs tend to be absorbed by molecules of oxygen "O_2", water vapor "H_2O" and other gaseous atmospheric constituents while travelling through the atmosphere. This absorption increases the path loss, especially in humid conditions, limiting the effective range of MMW communications. These losses are higher at certain frequencies coinciding with the mechanical resonant frequencies of the atmosphere molecules.

The H_2O and O_2 resonances have been studied extensively for predicting MMW propagation characteristics [20]. For example, at 60 GHz the O_2 absorption is very high, leading to an attenuation value of 16 dB/Km; this translates to only a 1.5 dB loss at 100m, so for indoor applications the absorption loss from oxygen is almost negligible. Moreover, attenuation varies depending on several physical factors that should be taken into account, namely pressure, temperature, and humidity.

Figure1.4 illustrates a detailed graph about the spectral regions between the absorption peaks providing windows where propagation can occur more readily with minimum potential absorption loss [20]. The frequencies around 35 GHz were extensively utilized in both commercial satellite and terrestrial communications. Likewise, the frequencies around 90 GHz have been long used for military communication purposes. It is important to avoid the molecular absorption peaks at 60, 119, 183, and 325 GHz, as these can significantly restrict transmission distances. However, the frequency ranges between these peaks, specifically around 80, 140, and 220 GHz, hold considerable promise for ultra-high data rate communications due to their potential for large BWs. It should be noted though that not all these bands are available for commercial services, except for the bands centered at 60 GHz (57–66 GHz, often referred to as V-band) and 70/80 GHz (71–76 GHz paired with 81–86 GHz, often referred to as e-band).

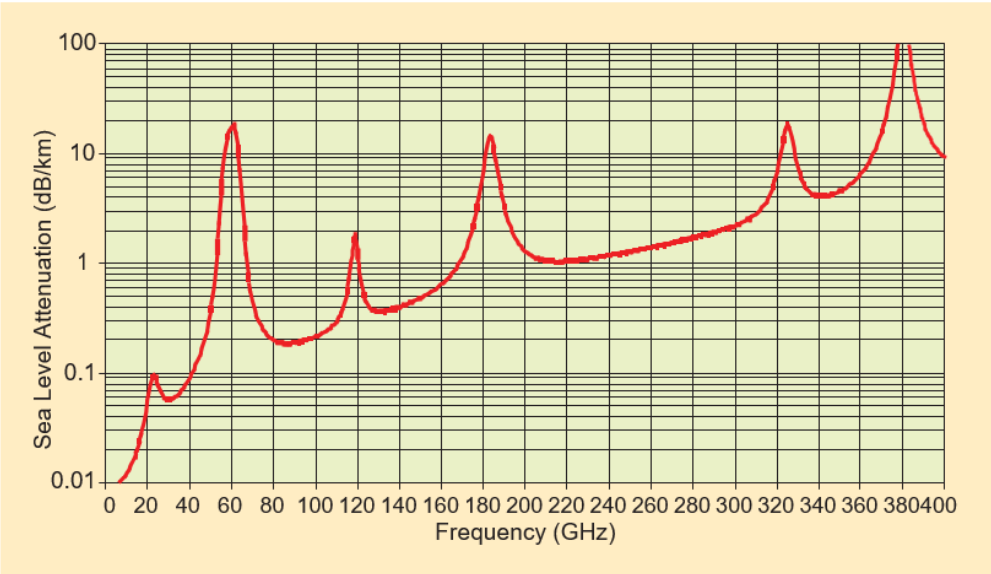

Figure 1-4 Average atmospheric absorption at MMW band [20].

From the other side, MMW signals are nearly the same size as raindrops [21], as shown in Figure1.5, resulting in reflection and scattering of radio signals, which in turn leads to multipath interference especially in heavy rain or stormy weather. This scattering has a significant impact on the propagation of MMW signals, which essentially increases the path loss with specific attenuation and time delays.

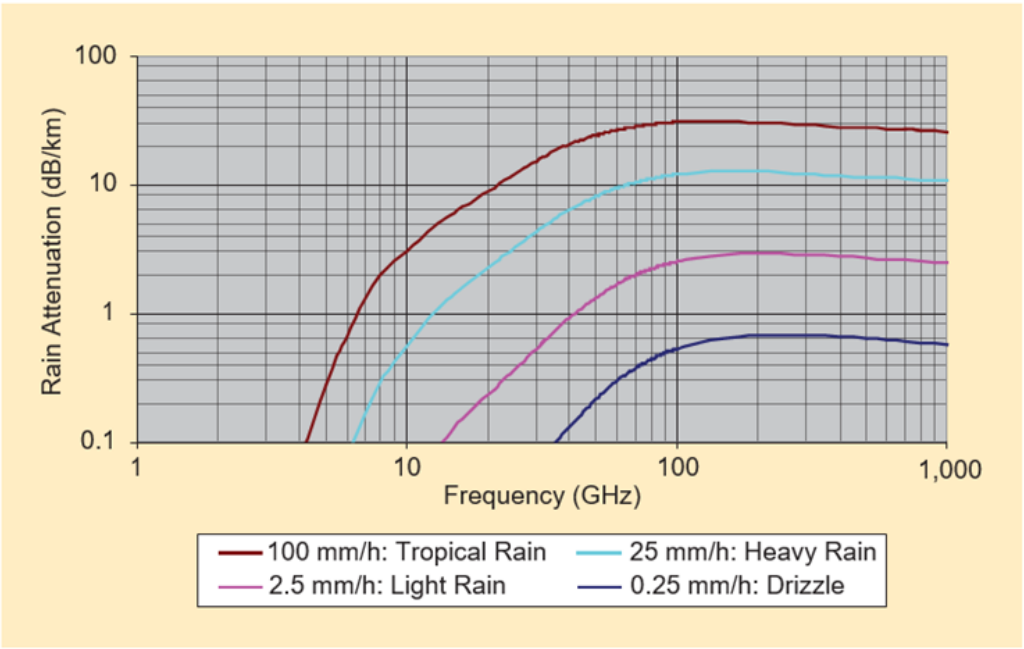

Figure 1-5 Rain attenuation at microwave and MMW frequencies [20].

1.3.4 Weak diffraction ability and foliage blockage

Diffraction is the bending of EM waves around obstacles or through apertures; it is inversely proportional to its wavelength, which makes it less effective as wavelength decreases relative to the size of the obstacle or diffracting edge.

Normally, mobile communication operates at lower frequencies between 800 MHz to 3 GHz. At this frequency band, the propagation and attenuation losses are low, which gives signals the ability to propagate for many miles and even to penetrate easily through buildings and thus ensure long-distance coverage. Whereas, in MMW bands, EM waves exhibit weak diffraction ability due to their short wavelengths, ranging typically from 1 mm to 10mm, which is relatively small compared to typical obstacles like buildings or vehicles, which makes it susceptible to blockage from any solid physical obstacles on their way. Thus, MMW signal travel by line of sight because of the short range of the propagating distance [22].

Another source for attenuation is the foliage blockage, which refers to the attenuation and signal loss that occur when MMW band EM waves encounter dense vegetation such as trees and bushes, which in some cases has as much impact as attenuation caused by atmospheric losses [23]. The interaction between MMW signals and foliage, particularly due to the water content in leaves and branches, leads to significant absorption and scattering, reducing signal strength and causing path loss [24]. This phenomenon poses challenges for outdoor MMW deployments in environments with abundant vegetation, influencing the reliability and coverage of wireless communication systems.

1.3.5 Fabrication costs

The fabrication costs pose a significant challenge in the deployment of MMW technologies due to several factors. Firstly, the design and production of MMW components, such as antennas, transceivers, and integrated circuits, require advanced manufacturing processes that are more complex and expensive compared to lower frequency counterparts [25].

Besides, due to their compact size, the implementation of passive components and interconnected transmission lines antenna would require a tighter tolerances and higher precision in fabrication and prototyping to build such a small structure and achieve the desired performance metrics while maintaining a good electrical contact with adjacent element [26], which further escalates costs. Moreover, the development of MMW systems often involves custom designs and specialized materials to mitigate propagation challenges like atmospheric

absorption and weak diffraction, adding more expense to the production. Finally, the demand for MMW equipment in new emerging applications such as 5G networks and high-speed wireless communications drives up costs as manufacturers invest in research, development, and scaling up production capacity to meet market demands.

1.3.6 Target search and acquisition

Target search and acquisition at MMW bands present significant challenges due to the characteristics of MMW frequencies, like narrow beam widths and susceptibility to attenuation by obstacles like buildings and foliage. The narrow beam widths of MMW signals from directional antennas require precise alignment between transmitter and receiver, making it difficult to maintain communication links with moving targets, dynamic environments, or large volume search [27]. Moreover, the propagation of MMW signals can be easily disrupted by environmental factors such as atmospheric conditions (e.g., rain), further complicating target acquisition.

It is worth mentioning that it is not yet clear which MMW band will be officially adopted internationally by the 5G systems once lunched [28]. Both Ka and V bands are good choice for multiple reasons.

1.4 Allocated MMW frequency bands

MMW frequency bands occupy a wide frequency portion of EM spectrum ranging from 30 GHz to 300 GHz, which corresponds to wavelengths of 10-mm to 1-mm. The overall band belongs to the EHF frequency category. The IEEE classifications of MMW frequency bands [29] are shown in Table 1. 1.

Table 1-1 MMW Bands classifications.

Specific Frequency bands based on ITU Assignments (GHz)	**Nominal Frequency bands (GHz)**	**Band Designation**
33.4 to 36	27 - 40	Ka
59 to 64	40 - 75	V
76 to 81	75 - 110	W
92 to 100		

126 to 142	110 - 300	MMW
144 to 149		
231 to 235		
238 to 248		

1.4.1 V band particularity

For many years, MMW technology has primarily been deployed for military applications only. However, in 2001, the Federal Communications Commission (FCC) [30] has designated the V band, centered around 60 GHz, as a new unlicensed frequency territory, which is free of charge for public use. This band offers a significantly greater bandwidth than the lower unlicensed bands all combined, which typically ranges from 4 to 9 GHz. As depicted in Figure 1.6, the global allocation of the 60 GHz band varies depending on the country, as way of illustration, Australia offers the lowest bandwidth with approximately 4.5 GHz large, while Europe has designated around 9 GHz. In comparison, it is worth mentioning that the 5 GHz band provides approximately 500 MHz of usable bandwidth, and the 2.4 GHz band offers less than 85 MHz in most regions. Moreover, the remaining unlicensed portions of spectrum below 6 GHz are practically non-existent, highlighting the ultimate significance of the 60 GHz allocation for future technologies.

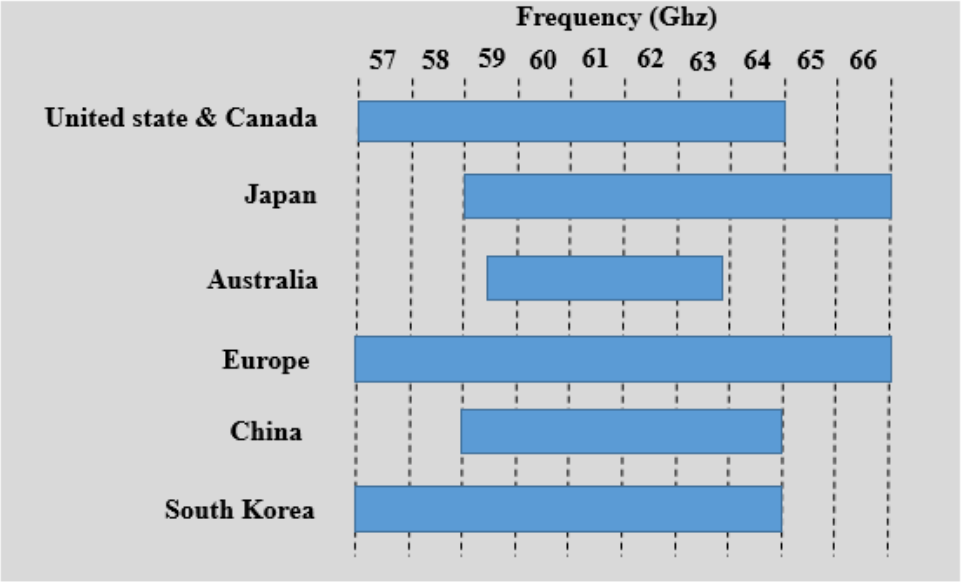

Figure 1-6 Unlicensed allocated spectrum in the V band [31].

This allocation has opened the chance and challenges for all fields of research to utilize this band in Industrial, Scientific and Medical (ISM) applications. The carrier frequency at 60

GHz has an ultra-wide BW capability that delivers unprecedented high data rates with several tens of gigabits per second and greater network capacity that are essential for supporting the massive increase in data traffic expected with 5G communication networks and high definition data (video streaming), virtual reality, and real-time gaming.

Additionally, beyond mobile broadband, the V band is suitable for providing high-capacity backhaul links between base stations as well, and for delivering fixed wireless access to homes and businesses. Also, the standards such as ECMA -387 [32] , IEEE 802.15.3c [33] and IEEE 802.11ad [34] are considered to meet the frequency spectrum requirements at MMW band especially for EPAN and WLAN.

Furthermore, the V band is well suited for deployment in dense urban environments where small cells can be strategically placed to enhance coverage and capacity. Despite their shorter range and susceptibility to blockage by obstacles, the use of small cells in these areas can ensure consistent connectivity and high performance [35].

However having access to this much wider BW spectrum does not come without challenges, and any new technology has to be also able to exploit the increased resources at a low cost.

1.4.2 Ka band particularity

The first part of this thesis was established in the Ka band because of the following reasons [36]:

a) MMW communications are very promising for the Local Multipoint Distribution System (LMDS) concept, which operates between 20 to 40 GHz.

b) Regional regulatory status and availability of (unused or underused) licensed spectrum for 28 Ghz and 38 GHz with an availability of standardized components at this frequency range [37]. This ensures consistency in spectrum allocation and usage across different countries, facilitating international roaming and interoperability of 5G networks and devices.

c) The Ka band offers substantial BW, which is crucial for supporting the high data rates and increased network capacity demanded by 5G networks. The allocated BW allows for efficient transmission of large amounts of data, enabling applications such as Ultra-High-Definition (UHD) video streaming, Virtual Reality (VR), and Internet of Things (IoT) devices.

d) Less susceptible to atmospheric absorption compared to higher MMW bands, like the V band or E band (60GHz to 90GHz) . In fact, the Ka band experiences less attenuation due to atmospheric absorption by oxygen and water vapor molecules. This characteristic makes it more suitable for deployments over longer distances and in regions with varying weather conditions, multipath environment and Non-Line-Of-Sight (NLOS) communications.

e) Adopting Ka band for 5G systems can be more cost-effective compared to higher MMW bands. It allows for the use of existing infrastructure and equipment to a certain extent, reducing deployment costs and accelerating the rollout of 5G services.

1.5 Specifications of MMW antennas

MMW antennas should acquire some specific design parameters tailored to their dedicated application. These specifications ensure that MMW antennas can effectively manage handle the particular challenges of high-frequency operation, including increased path loss, atmospheric absorption, etc.

Some key specifications can be sited in the following:

- Frequency range: the operating frequency of the antenna must fall within the MMW allocated specific sub-bands, depending on the application; for example 60GHz for WiGig [38], 77GHz for automotive radar systems [39], 94GHz for imaging applications [40].
- Gain: high gain is often required to compensate for the increased free space path loss at MMW frequencies. It can range from 5dBi for compact size antennas [41], to 40 dBi or more for large parabolic dishes or phased arrays systems [42].
- BW: MMW antennas need to support wide BW to handle high data rates and ensure efficient communication. BWs can range from a few GHz to tens of GHz [43], depending on the application.
- Dimensions: due to the small wavelength at MMW frequencies, antennas can be very compact [44]. This is advantageous for integration into small devices but requires precise fabrication techniques [45].

- Radiation pattern: MMW antennas are designed to have specific radiation patterns; such as omni-directional [46], directional [47], or multi beam (Phased array) patterns [48] based on the application needs.
- Polarization: linear [49] or circular [50] polarizations are typically used, with the choice depending on the system requirements for signal integrity and interference rejection.
- Efficiency; high efficiency is critical to minimize losses and ensure effective signal transmission and reception [51], especially important due to the higher free-space loss at MMW frequencies.

Table 1.2 describes the type of antennas that can be used for MMW applications and their respective advantages and disadvantages [12].

Table 1-2 Types of MMW antennas and their respective advantages and drawbacks .

Antenna type	Advantages	Disadvantages
Printed and planar micro strip (slot, patch ME dipole, Yagi, …etc.)	Low profile Cost effective Good integration ability Light weight Easy mass production	Small power capacity Low gain and radiation efficiency Narrow band High losses and sensitivity
On-chip integrated (phased arrays, MIMO..)	High degree of integration High reliability High gain and efficiency Compact structure Beam steering ability	Low resistivity Small metal conductivity Complex design High cost High power consumption
Reflector and lens	Wide BW High gain and directivity	High profile High cost
Horn	Wide BW High power capability Simple deign Low loss	Large size Limited portability High fabrication cost
Leaky Wave	Broad frequency range Directional radiation patter Beam scanning	Complex design and fabrication High losses

DRA	Compact size Wide BW High gain and efficiency Low loss	Material dependency Temperature sensitivity Expensive

1.6 Problematic

The progression of information and communication technology in the last decades resulted in a tremendous impact on all aspects of individual's life and on society. In the recent future, the globalization of wireless data transfer in the next generation systems is estimated to include more applications (medical, surveillance, smart homes, and radio broadcasting... etc.), and not only limited to mobile communication purposes. In view of that, wireless communication technology became one of the most competitive research topics to meet the consumer's massive demand for better quality services and higher data rates.

The frequency band under 6Ghz is already crowded and cannot support the massive amount of 5G applications whereas the unexploited frequency spectrum starting from 30GHZ to 300GHz offers a lot of sub bands such as Ka and V bands that can provide a multi-gigabit per second (Gbit/s) data rate transmission.

Historically, the era of MMW technology goes back several decades ago where it was mostly used in military (directed energy weapons), radio mining applications, space-astronomy, imaging technology, medical and security scanners, mainly because of high cost and limited availability of electronic devices. Currently, due to the rapid advancement of wireless communications compared to the past and the urgent need for MMW frequency spectrum, it can be used for applications such as short-range automotive radars [52], remote sensing, high-resolution imaging, high definition video transfer, Wireless Gigabit (WiGig) [53] and security screening. All these applications require, however, low power and low-cost wireless systems that include high gain and high efficient planar antennas to compensate for path loss.

In the context of advancing 5G networks, the deployment of MMW frequencies presents both unprecedented opportunities that make it a good candidate for future wireless communications and significant challenges as well. While MMW bands offer the potential for extraordinarily high data rates and enhanced capacity, they also pose considerable challenges that are related to signal attenuation, propagation losses, and limited coverage range.

The primary problematic aspect lies in developing antennas that effectively address these issues while maintaining compactness and high efficiency. The traditional transmission technologies used before at lower frequencies struggle to cope with the stringent requirements of MMW frequencies, they have many shortcomings related to performance or manufacturing challenges and it can not be reused at the MMW band [54]. This will open a large gate for new antenna technologies. For example, the conventional planar structures, such as the microstrip, coplanar, and Substrate Integrated Waveguides (SIW), are flexible for integrating with other printed circuits and are easy to fabricate but they suffer from high dielectric losses as the signal propagates in the dielectric substrate, especially at high frequencies. Another example is the air-filled waveguides (rectangular and circular waveguide) which are preferred for applications that require low-loss and high power handling capability [55]. However, they are bulky and difficult to integrate with planar circuits, especially at high frequencies. In addition, these technologies are hindered by the existence of the cavity resonances when using a closed structure, which has negatively influenced waveguide performance. In addition to the dielectric loss, microstrip and coplanar structures may suffer from radiation loss if they are not perfectly packaged. Furthermore, the size of an antenna is determined by the order of wavelength; for instance in the MMW frequency spectrum, the wavelength is short and more susceptible to high attenuation or blockage. Another challenge for MMW band is to realize an overall system ensuring low loss with integration between passive and active components while being cost-effective and compact size simultaneously so the antenna design would require a high level of precision in the fabrication. Surface waves are another critical issue that causes high losses when designing a microstrip network for single or multi antenna configurations. These unwanted waves have an impact on the radiation pattern of the antenna [56] and necessitate the exploration and integration of innovative solutions like Ridge Gap Waveguide (RGW) technology.

In summary, it is essential to design an optimal antenna type for the MMW frequency range, which would meet these challenges through its compactness, efficiency and gain as high as possible and bandwidth as wide as possible. This research will delve into the intricacies of these defies, aiming to devise antenna designs that not only mitigate signal degradation and interference but also adapt to the evolving demands of high-frequency communication systems.

1.7 Objectives and contributions

The objectives of this thesis are multifaceted and are essentially structured around the following three main axes:

- The development of a state of the art on the research results linked to the targeted issue,
- The presentation of a concise and coherent theory on certain techniques and tools essential to the understanding of the different proposed contributions, and finally,
- The provision of effective and convincing solutions to the targeted problems.

The effort consented in the first part of this thesis aims to provide a comprehensive overview and critical analysis of 5G networks, with a specific emphasis on exploring the capabilities and challenges posed by the MMW frequency band. This includes investigating the unique propagation characteristics of MMW signals, their potential for high-speed data transmission, and the technological advancements needed to overcome current limitations in deploying MMW networks effectively. Thereafter, exhaustive work is conducted to explore and evaluate various guiding techniques and transmission lines used in microwave engineering. This involves a thorough examination of traditional methods such as micro strip lines, as well as emerging technologies like Printed Ridge Gap Waveguide (PRGW). The goal is to assess their theoretical foundations, practical advantages, and limitations in achieving compact, low-loss microwave components suitable for modern communication devices.

The next part of the thesis presents a thorough contribution to original research and knowledge on advanced and miniaturized antenna structures dedicated to the most recent communications techniques. As first contribution [57], a deep study is conducted on DRA antennas. In effect, an investigation of their radiation characteristics, performance, and practical applications in MMW band with the exploration of recent advancements in antenna design based on novel concepts proposed in recent research literature, permitted the design of a novel miniaturized bi-band TDRA array with an upside copper metallization providing dual-beam. This structure has achieved a suitable beam pointing coverage for the desired double-beam radiation performance with a high radiation efficiency and a relatively wide impedance bandwidth.

Afterwards, other major research attempts were proposed [58]. Firstly, an enhanced version of a planar rectangular slot antenna fed by the Quazi-TEM Printed Ridge Gap Waveguide (PRGW) is proposed. Therein, a numerical study of a miniaturization procedure showed the limitations of the conventional PRGW-based antennas. Then, an innovative miniaturization solution is introduced in a pure TEM wide-band slot antenna utilizing Double PRGW (D-PRGW) technology. The high performance along with the compact size of this novel design made it a good candidate for 5G wireless communications applications centered around 60GHhz.

Overall, this work, on the one hand, contributes deeper understanding and new insights into the complex guiding techniques in microwave engineering and advanced antenna technologies; on the other hand it proposes new antenna structures with higher performance than classical ones, to encounter the propagation losses issue in the free space and satisfy the latest 5G communication technology requirements.

By addressing these objectives, the work seeks to advance knowledge in these fields and contribute practical solutions to current and future challenges in wireless communication systems and antenna design.

1.8 Thesis outlines

This work is structured into four comprehensive chapters, each meticulously exploring essential aspects of advanced telecommunications and antenna design technologies.

The first chapter provides an overview of 5G networks and their implications, focusing particularly on the utilization of MMW frequencies. This chapter explores the challenges and opportunities presented by the MMW band in modern communication systems.

The second chapter delves into guiding techniques and transmission lines, discussing conventional and emerging methods for guiding EM waves, such as waveguides, SIWs, and RGW. It highlights their advantages and limitations in various applications.

The third chapter presents a dual-beam array antenna based on Triangular Dielectric Resonator Antenna (TDRA) for Ka-band applications that consists of 2×1 radiating elements sharing a common ground plane and plated with a thin copper layer at the upper side. The antenna effectively covers two separate bands (28 GHz and 33GHz) with a double-beam radiation at both operating frequencies. This structure has achieved a very low return loss and

substantial gain at its operating frequencies, with high radiation efficiency across each band. The radiation beam is pointing at two distinct angles, with wide angular coverage in each case.

Finally, the fourth chapter starts with numerical study of a miniaturization procedure applied to a rectangular slot based on the conventional Quazi-TEM PRGW. After that a novel approach based on the wide-band pure TEM D-PRGW technology was proposed in order to overcome the impairments of the previous PRGW systems with strictly minimum elements and compact overall size. This novel approach is shown to deliver a wide BW with relatively higher gain and greater efficiency all over the operating band.

CHAPTER 2: LETERATURE OVERVIEW OF TRANSMISSION AND WAVE GUIDING TECHNIQUES

2.1 Introduction

The conventional, well-characterized transmission structures such as hollow waveguides and coplanar waveguides have been extensively exploited in the variety of complex RF components due to their well established performance characteristics. These techniques have historically provided reliable solutions for RF signal transmission, but they encounter significant challenges when operating at higher frequencies. This is largely attributed to their small physical dimensions and the resulting short and weak effective wavelengths, which lead to inefficiencies and performance degradation. As frequency requirements push beyond traditional limits, these conventional structures struggle to maintain optimal performance.

To overcome these limitations, researchers are actively exploring new technologies that seek to merge the advantageous features of existing guiding techniques. The goal is to develop a new class of transmission structures that are not only as cost-effective and flexible as micro-strip lines but also offer the low loss and robustness typically associated with metal waveguides. These advancements aim to address the frequency-dependent challenges and offer improved performance across a wider range of applications.

This chapter delves into a comprehensive literature review of existing guiding structures, providing a thorough understanding of their historical and current applications. It then transitions into an in-depth exploration of RGW background, including their propagation properties and underlying mechanisms. The discussion extends to the potential problems and challenges associated with employing RGW in the MMW band. By examining these aspects, the chapter aims to provide a detailed overview of how RGWs could potentially overcome the limitations faced by traditional transmission mechanisms, paving the way for more advanced and efficient RF component designs.

2.2 Overview of traditional guiding structures.

The propagation through a guiding structure is one of the most critical and challenging topics in the wireless communication research area. In 1864, James Maxwell discovered that EM disturbance travels with the speed of light, introducing twenty equations involving twenty variables to describe this phenomenon. After that, Hertz proved the predictions of Maxwell's equations experimentally, and drove the core principle from the original equations, which has further resumed into only four equations including four variables. These brilliant experiments managed to obtain the universal acceptance of this theory.

Based on the modified version of Maxwell's equations presented earlier by Hertz, the wave equations were then directly obtained by Helmholtz at the end of the 18th century as second order differential equations that bound the electric and the magnetic fields behavior inside any structure. Solving these differential equations in accordance with the boundary conditions of the structure will result in a full description of the EM field propagating inside, which will be presented as encapsulation of TE, TM, TEM and hybrid modes where every mode is in the form of an Eigen function. This solution is addressed in the design of all guiding structures including parallel-plate waveguides, rectangular and cylindrical waveguides… etc. [55].

The propagation modes inside the guided structure depend on the operating frequency, the fields' polarization and the waveguide's shape and dimensions. Accordingly, they can be classified into three mode types:

1. Transverse Electric (TE);
2. Transverse Magnetic (TM); and
3. Transverse Electromagnetic (TEM).

It is preferable for microwave signals to propagate in TEM mode because of its advantages over other TE and TM modes, including its immunity to any dispersion and its ability to carry any signal at any frequency since it has a zero cutoff frequency.

2.2.1 Microstrip line and stripline

Typical microstrip feeding lines are suitable for low-cost, low profile, and robust applications operating at lower frequency range since they are fabricated based on cheap Printed Circuit Board (PCB) technology. However, the transmission properties of these lines depend relatively on the substrate parameters. By definition the microstrip consists of a thin laminate of low loss insulating material called dielectric substrate that is fully covered with a

conducting plane on one side (usually referred to as the ground plane), and partially metalized on the other side as per the design of the feeding network. Figure 2.1 (a) illustrates a front view of typical microstrip line; the quasi-TEM mode propagates between the strip conductor and the ground plane through the dielectric substrate. Since the wave propagates in the dielectric material and the strip conductor is uncovered, the microstrip line suffers from three types of losses, namely dielectric, ohmic, and radiation loss. These losses become more significant at high frequency bands.

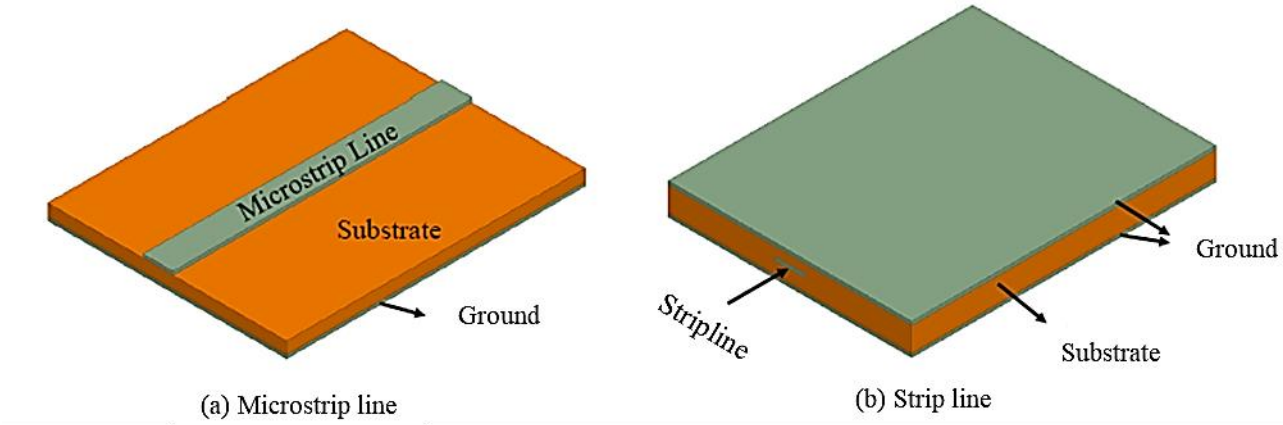

Figure 2-1 Microstrip line and strip line.

Moreover, at higher frequencies, the microstrip transmission line undergoes high cavity modes and power leakage as depicted in Figure 2.2 (a), due to the spurious radiations in the form of surface waves especially from discontinuities and borders in the feeding network of the microstrip line [59], which leads to undesirable radiation causing serious crosstalk, interference problems and coupling between adjacent circuit's components. Besides, the transmission losses increase due to medium's resistance that is linearly proportional to the square root of the frequency, so as the carrier frequency increases, the losses in the transmission lines increase as well. In addition, using a thinner substrate requires using a narrower metal strip (usually matched to 50 Ω) that causes an increase of the conduction losses due to the high resistance. These limitations considerably influence the suitability of microstrip lines for MMW frequency bands [60].

Another type of guiding structure that can also reduce the dielectric losses, referred to as microstrip line, is shown in Figure 2.1 (b). The TEM mode propagates between the strip and the top ground, similar to the coaxial transmission line, which is non-dispersive at all frequencies. Moreover, since the strip line confines wave propagation between two ground planes, there is no wave leakage as depicted in Figure 2.2 (b), which unlike the microstrip

waveguide, provides high isolation between adjacent circuits. However, the implemented two ground planes make strip narrower, being only half the width of the microstrip line for a given frequency. The narrow strip not only considerably increases conduction losses due to the higher current density and conductor roughness but also causes challenges in the fabrication at high frequencies for the required high precision. Moreover, any vertical asymmetry in the strip line can create unwanted higher order waveguide modes that will be able to propagate wherever the two ground planes exist.

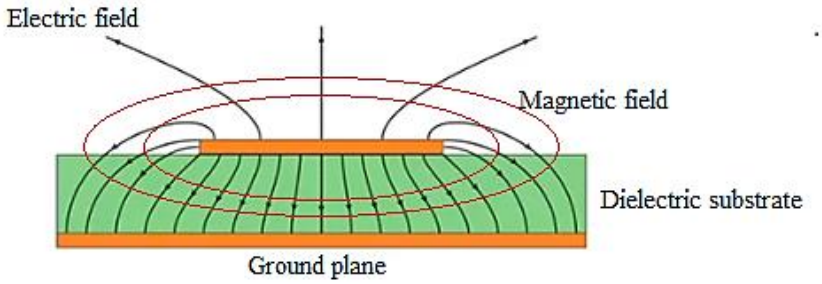

(a)

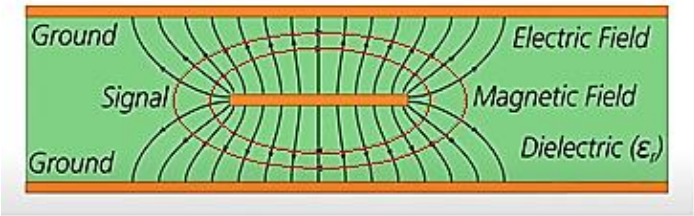

(b)

Figure 2-2 E field distribution (a) on a microstripline, (b) on strip line.

2.2.2 Coplanar and grounded coplanar waveguides

The coplanar waveguide (CPW) is another form of transmission line realized by including the conductor central strip line between two ground plane conductors with a certain width that are separated by two gaps, as shown in Figure 2.3 (a) [61]. In this technology, the fields propagate inside the dielectric substrate as a quasi-TEM mode at low frequencies and as a TE mode at high frequencies. As the fields are not totally confined within metallic boundaries, they present some energy leakage. The loss due to this leakage is partially controlled by tuning the ratio between the width of the central strip and the substrate's thickness, whose optimum ratio is 1:2. The CPW has low dispersion losses in large part because it supports

quasi-TEM mode. Moreover, it is easy to fabricate and is more flexible to design because all of the conductors are packed in the same layer. However, the CPW suffers from high dielectric losses and unwanted surface waves modes excited due to discontinuities such as T-junction. This disadvantage can be avoided by inserting air bridges over the center conductors to have the same potential on both ground planes and provide a shield over the discontinues parts [62]. These air bridges can cause a lot of difficulty in the fabrication process and make it more complicated.

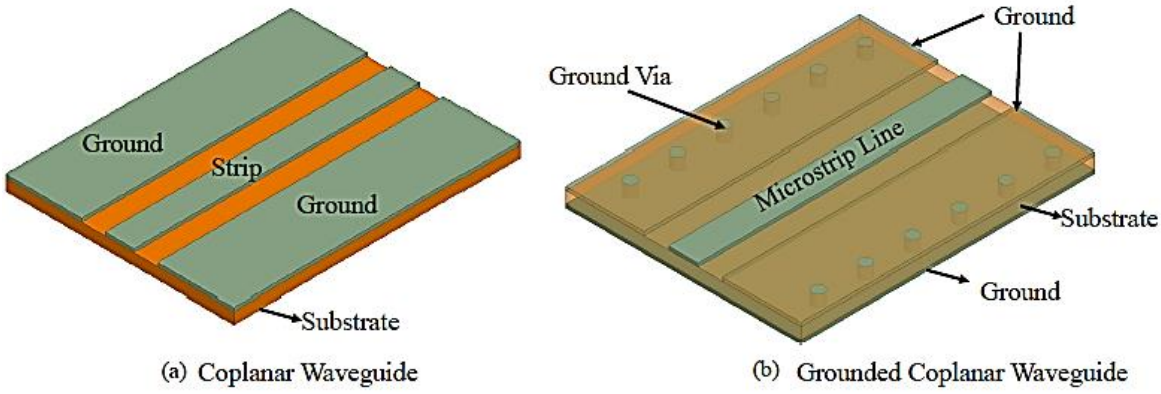

Figure 2-3 CPW and GCPW.

The Grounded Coplanar Waveguide (GCPW) is similar to the CPW, but, as shown in Figure 2.3 (b), with a ground plane at the bottom of the substrate and side strips grounded through metallic via holes [63]. The ground plane added at the bottom of the substrate acts as a bottom shield to provide isolation from any other active components in lower layers when integrated within a system. The GCPW has even lower losses compared to the CPW, although it still suffers from dielectric losses. When the GCPW is integrated and packaged inside an enclosed system, some cavity modes may propagate and affect the performance [64]. In addition, tuning the impedance of the GCPW is easily achieved by changing the space between the grounds and the signal line. The disadvantage of the GCPW is its high vulnerability to losses in the MMW frequency range, which makes it less efficient for these ranges of frequencies.

2.2.3 Hollow waveguide

Among all waveguide's implementation technologies, the hollow waveguides also called air filled waveguides, as shown in Figure 2.4, demonstrate more advantages than microstrip transmission line. For instance, they have superior electrical characteristics in terms of high

Q-factor, low insertion loss, Voltage Standing Wave Ratio (VSWR) close to 1, high power handling capability and compliance with international standard systems [65]. Cylindrical and rectangular waveguides are the most popular air filled waveguides due to their high shielding effectiveness. These waveguides are usually made of hollow metallic tubes plated from the inside with silver or copper to decrease the skin effect and are realized in separate split blocks connected by screwing, diffusion bonding or deep-brazing techniques as illustrated in Figure 2.5.

Figure 2-4 Conventional air filled waveguides.

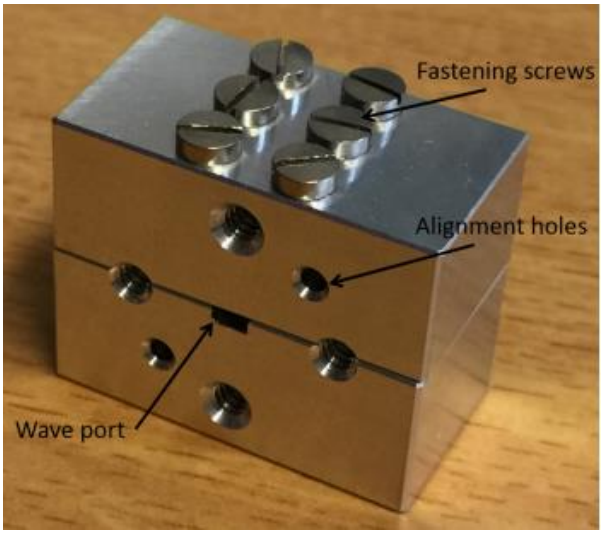

Figure 2-5 Two-blocks conventional rectangular waveguide.

These machining techniques are usually costly, complicated, less accurate and not scalable when approaching higher operating frequencies due to the considerable reduction in physical dimensions that require a high level of precision for manufacturing and assembling the

waveguide split-blocks. Hence, the intact electrical contact at the joints as well as the perfect alignment of the blocks, that are strictly needed to avoid any leakage between the waveguide segments, became more challenging and less accurate.

In addition, the width of the waveguide must be the half wavelength of the operating frequency. Therefore, the waveguide is increasingly impractical for frequencies beyond 1 GHz especially at the MMW frequencies, where the wavelength becomes very short (10 to 1 mm), and the realization with current machining techniques become very complicated and costly.

From the other hand, there is a difficulty in matching this type of waveguide with another microstrip system because of their weight and their rigid, bulky and hollow-pipe shape. Therefore, they are not suitable for compact planar circuits and low-mass productions. In order to integrate this type of waveguide in a system, it should be machined as a groove within the metal and then covered with a metal sheet that should be screwed around the groove to assure tight electrical contact, which finally end up with the hollow waveguide. The machining procedure may be accepted up to certain frequency bands, but at MMW frequencies, high accuracy is required, and the electrical contacts between two metals may not be guaranteed.

Furthermore, the conventional hollow waveguide supports TE and TM propagation modes but not a TEM mode (apart from coaxial lines). They only operate after a specific nonzero cutoff frequency, which is referred to as the dominant mode cutoff frequency. The dominant mode represents the only mode that may exist alone in the waveguide and, thus, the most usable one. Such dependency on TE and TM modes is one of the major disadvantages of air-filled waveguides because it is subjected to intra modal dispersion.

The dominant mode of the standard rectangular waveguides is the TE_{10} mode since it has the lowest cutoff frequency, while that of standard circular waveguides is the TE_{11} mode. The dominant mode of the waveguide can have practically a limited operating BW for a single-mode operation that can reach 2:1. However, the usable frequency range is typically lower then this with higher dispersion characteristics; this is mainly attributed to the fact that the allocated BW is limited to the stable band between the cutoff frequency of the dominant mode and the cutoff frequency of the next higher order mode. Typically, the practical operating BW must start higher than the lowest mode and lower than the next higher order mode to have

some safety factors. It is important to operate far from the cutoff frequency of both modes to ensure neither having an evanescent mode nor having a higher order propagating mode [66].

Many designs have been proposed as an attempt to overcome these problems. As a pioneer, the Non-Radiative Dielectric (NRD) waveguide, which consists of a dielectric rod sandwiched between two parallel plates, was invented in [67] and further improved in [68]. In this way, there will be a TEM transmission line that does not need any electrical contact and leakage is limited by using the dielectric rod and maintaining the gap between the two plates smaller than a quarter of a wavelength. However, this technology still suffers from significant dielectric loss.

All the above-mentioned drawbacks increase the complexity and the cost, making the fabrication more delicate and challenging for this kind of waveguides, which direct us towards a new type of guiding structures.

2.3 Boundary conditions principles

Boundary conditions in general are fundamental principles in EM theory that describe the behavior of electric and magnetic fields at the interface between two different media. Various boundaries can be classified as lossy, lossless, absorbing, etc.

2.3.1 Isotropic ideal boundary conditions

In this section, we will discuss the concept of isotropic ideal boundary condition [69],that is defined as a surface on which the normal component of the complex Poynting vector does not have a normal component for any time-harmonic fields with time dependence (e^{iwt}) at the boundary [70], which implies that no EM fields pass or propagate through it. In other words, at the surface the complex Poynting vector is defined as [71]

$$S = \frac{1}{2} Re\,[E \times H^*] \qquad 2.1$$

where E is the E- field vector, H^* is the complex conjugate of the H-field vector. Hence, S will have no component normal to the boundary for any possible E-fields, that is

$$\mathrm{n} \,.\, \mathrm{S} = 0 \qquad 2.2$$

It is worth mentioning here that this definition is different from that of the lossless boundary, which is related only to the real part of the Poynting vector.

The condition of no component normal to the boundary for any possible fields at its surface encounter two basic ideal boundary conditions,

- Perfect Electric Conductor (PEC) when $n \times E = 0$ and
- Perfect Magnetic Conductor (PMC) when $n \times H = 0$

For a PEC surface, the E-field has no tangential component ($E_t = 0$) and, for a PMC surface, the H-field has no tangential component ($H_t = 0$).

2.3.2 Anisotropic soft and hard surface

The core principle of Soft and Hard surface terminology is well defined in acoustics since 1944 by Cutler [72], where acoustic signals are absorbed by soft surfaces and reflected by hard surfaces. In 1988, this concept was re-introduced by Kildal to describe the EM wave propagation along a corrugated surface [73]. Fundamentally, soft and hard surfaces are classified within the metamaterials category; it is a class of artificial surfaces that demonstrate electromagnetic characteristics, such as magnetic conductivity, which are unconventional in natural materials.

Preferably, a soft-hard surface can be understood by PEC and PMC strips alternation as illustrated in Figures 2-6 and Figure 2-7, signifying the hard surface when the strips are longitudinal (oriented in the same direction as the wave propagates), and the soft surface when they are transverse (at right angles, i.e., orthogonal to the direction of propagation) [74]. The direction of the wave propagation is relative to the direction of the corrugation and determines whether it enables or prevents the wave propagation at the surface. The PEC and PMC strips can be recognized in terms of their anisotropic surface impedances which occur either by disturbing an ideal conducting surface alternately with successive transverse corrugations (Soft) and dielectric-filled longitudinal grooves (Hard), or by loading a dielectric substrate with transverse (Soft) or longitudinal (Hard) metallic strips [75] [73].
The depth of the corrugation "d" can be represented using the equation below [76],

$$d = \frac{\lambda}{4\sqrt{\varepsilon_r - 1}} \qquad 2.3$$

where λ is the free space wavelength, ε_r is the dielectric constant of the material that must be higher than the permittivity of the medium above the surface.

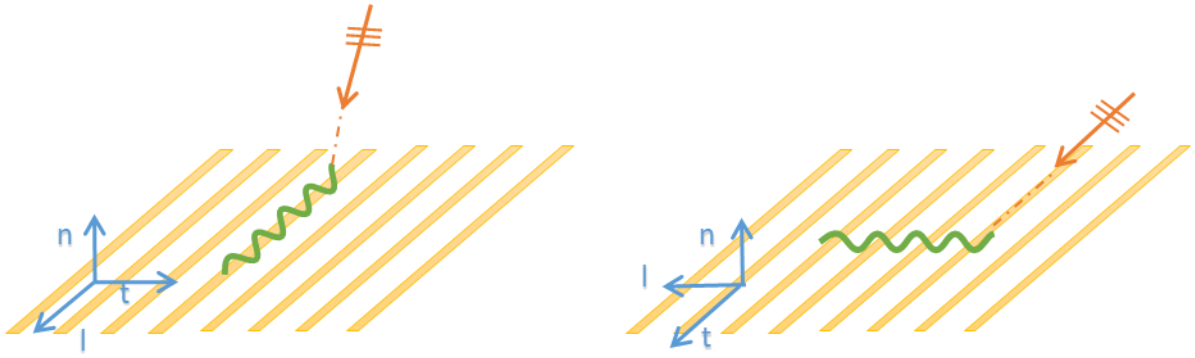

(a) (b)

Figure 2-6 PEC/PMC strip-model. (a) Soft surface and (b) Hard surface.

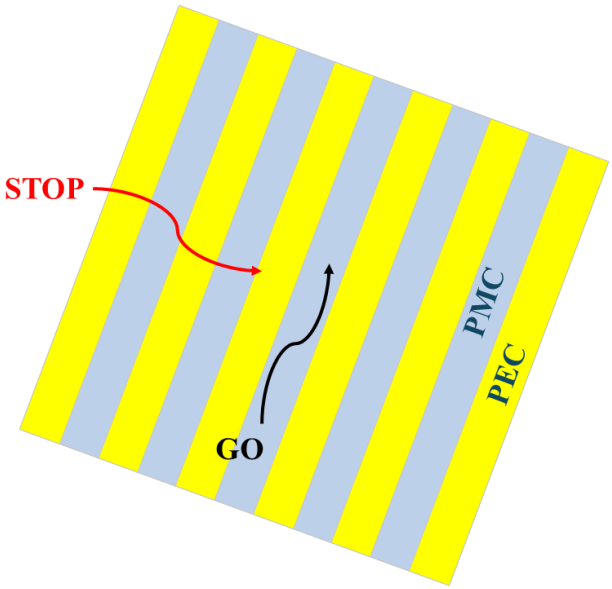

Figure 2-7 Alternation of soft and hard surfaces.

In other words, the soft surface halts the wave propagation with any polarization along the surface whereas the hard surface enhances the propagation along the surface. These characteristics are deployed in corrugated horn antennas to reduce the side-lobe level, couplings, and cross polarization.

To be more specific, the soft and hard surfaces are defined in terms of their Leontovich anisotropic surface impedances as follows [77].

$$\mathrm{E}_t\hat{\mathrm{t}} + \mathrm{E}_l\hat{\mathrm{l}} = Z_s\hat{n} \times \vec{H} = Z_s(\mathrm{H}_t\hat{\mathrm{t}} - \mathrm{H}_l\hat{\mathrm{l}})$$

$$\mathrm{E}_t\hat{\mathrm{t}} + \mathrm{E}_l\hat{\mathrm{l}} = \mathrm{Z}_t\mathrm{H}_t\,\hat{\mathrm{t}} - \mathrm{Z}_l\mathrm{H}_l\,\hat{\mathrm{l}} \qquad 2.4$$

Where Z_s is the surface impedance, $\vec{H}$ is th H-field vector, E_l, and E_t, are respectively the longitudinal and transverse components of the E-field, H_l and H_t, are the corresponding components of the H-field.

The longitudinal direction $\hat{l}$ is in the direction of the Poynting vector at the surface (i.e. the direction of the power flux), while transverse direction $\hat{t}$ is orthogonal to it. Both directions are tangential (normal) to the surface.

In light of this, the transverse and longitudinal surface impedances of corrugated texture can be defined respectively as

$$Z_t = \frac{E_t}{H_t} \quad 2.5$$

$$Z_l = \frac{-E_l}{H_l} \quad 2.6$$

It should be noted that the signs in the aforementioned equations are correct if

$$\hat{l} \times \hat{t} = \hat{n} \quad 2.7$$

with $\hat{n}$ the surface normal.

The surface impedance can also be described from transmission line concept, such that the short circuit becomes an open circuit at the top of the corrugation. As a result, a high anisotropic surface impedance in the transverse direction of the corrugation acts as an AMC and zero surface impedance along the corrugations acts as a PEC. Therefore, for narrow and smooth corrugation, there is approximately no EM wave propagation.

2.3.2.1 Hard surface

In ideal hard surface [77], the corrugations are oriented in the longitudinal direction of propagation $\hat{l}$ (strip-direction) as shown in Figure 2.8. It should be noted that the dielectric grooves must be filled with a dielectric material of dielectric constant greater than the permittivity of the medium above the surface (in free space case $\varepsilon_r > 1$).

The longitudinal metallic strips act as a PEC that imposes the annulment of E_l, so that the longitudinal impedance is $Z_l = 0$.

Simultaneously, the PMC strips annuls H_t so that the transverse impedance $|Z_t| = \square$.

The hard surface behaves like a PMC in H-plane and as a PEC in the E-plane. It prevents the propagation of only the longitudinal field component and supports the propagation of the transverse fields.

The hard surfaces suspend only the longitudinal electric and magnetic field components and thus support only TEM mode propagation [78].

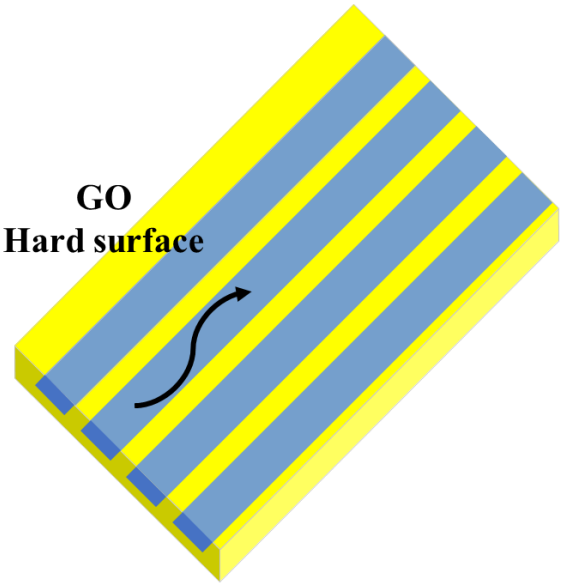

Figure 2-8 Dielectric hard surface.

Hard surfaces can be used when strong propagation among the surface is needed. It is mostly applied to the concept of the hard waveguide in which quasi-TEM modes can propagate along the longitudinally dielectric filled corrugation. This structure has also been used in horn antennas for increasing the aperture efficiency [79] and in miniaturized array elements as well for multi-frequency applications [80].

2.3.2.2 Soft surface

For modeling ideal soft surface the corrugated strips in Figure 2.9 are oriented along the transverse direction of propagation, which implies vanishing of transverse components for E-field. The transverse metallic strips act as a PEC, imposing the annulment of E_t so that the transverse impedance would be $Z_t = 0$.

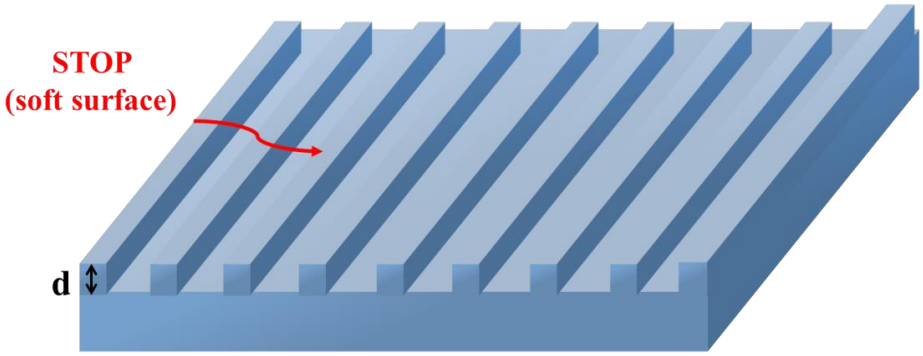

Figure 2-9 Corrugated soft surface.

Simultaneously, at the transverse strip acting as PMC, any longitudinal H-field component would be countered by induced surface currents, resulting in $H_l=0$ which implies that $|Z_l| =$ □.

The soft surface behaves like a PEC in H-plane and as a PMC in the E-plane.

Both the transverse components of electric and magnetic fields abolish. Thus, the propagation of EM wave of any polarization is annulled and the power flux density at the surface is equal to zero.

Corrugated surfaces can be considered as a 1D bandgap configuration (ground strips or corrugations with a height of quarter guided wavelength) or as 2D configuration (periodic structures) to provide a higher degree of freedom for high surface impedance implementation.

Soft surfaces are used in many applications such as corrugated horn antennas in hard waveguide horns to increase aperture efficiency as feeds for reflector antennas [81]. It can also be used as isolation between the aperture of the horn and the feeding network. In addition, it can improve the back-lobe radiation of the horn antenna.

In general, the impedances and boundary conditions of the different ideal surfaces for EM wave propagation along the surface in longitudinal $\hat{l}$, transversal $\hat{t}$, and normal $\hat{n}$ directions relative to a right-hand coordinate system as plotted in Figure 2.10 are depicted in Table 2.1.

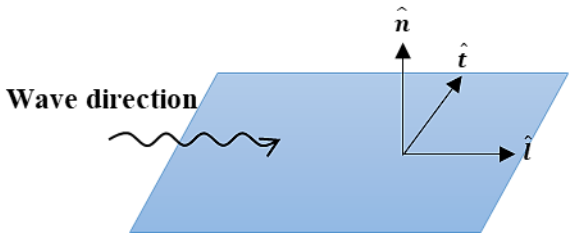

Figure 2-10 Coordinate system for waves propagating along surfaces.

Table 2-1 Impedances and boundary conditions of different ideal surfaces for waves propagation along longitudinal direction.

Surface type	**Impedance**		**Boundary conditions Transverse E components**		**Surface wave propagation E- field polarization**	
	Z_l	Z_t	Normal E_n	Tangential E_t	Vertical Polarization /TM E_n	Horizontal Polarization /TE E_t
PEC	0	0	$\frac{\partial En}{\partial n} = 0$	E_t=0	Go	Stop
PMC	∞	∞	En=0	$\frac{\partial Et}{\partial t} = 0$	Stop	Go
Soft	∞	0	En=0	E_t=0	Stop Polarization Independent	
Hard	0	∞	$\frac{\partial En}{\partial n} = 0$	$\frac{\partial Et}{\partial t} = 0$	Go Polarization Independent	

2.4 Periodic structure

The periodic structures are a very old concept in the EM field of research. When EM waves interact with a periodic structure, it results in some interesting characteristics that have several applications. The periodicity of the structure adds some features and properties for the wave propagation. One of the most famous application of periodic structure is the filter design. Besides, it can be used to improve the antenna performance in terms of gain, directivity in broadside direction, BW, and side lobe levels.

The two main categories of periodic structures were discussed in the above sub-section. There exist many types of periodic textures where some are named specially based on their corrugation, behavior or basic operation. This work focuses on the EBG type, which consists of metallic pins unit cells covered by two-conductor surfaces on top and ground planes. This bed of pins generates a high impedance surface (HIS); in other words, it generates an AMC due to the boundary condition that they provide (the tangential component of the magnetic field is zero at the surface) which has the property of preventing EM waves propagation in a specific frequency band.

2.4.1 EBG functionality

Initially, the description of EBG began as Photonic Band Gap (PBG) materials or Photonic Crystals (PhC) structures, which principally deal with type of structures and frequencies pertaining to optics field. PBG structures came in 1D, 2D, or 3D periodic profile (both dielectric and conducting) which can prevent light or wavelength of certain frequencies from propagating in any number of polarization directions within the allocated stop band. The PBG designation was extended to include other types of structures and frequencies, such as EBG structures. The terminology of EBG structures was proposed in [82] to describe 2D FSS behavior. These structures control the frequency band (stop-band, pass-band, and band-gaps) when altering the surface of a structure, by modifying its geometry, and/or adding other layers exactly as soft and hard surface principle.

The bed of nail's lattice is divided into periodic identical unit cells. The engineering of these surfaces involves altering the impedance boundary conditions of the surface of a structure and, thus, controlling the wave propagation characteristics. The unit cell dimensions, including its height, width, and top gap distance, determine the stop band provided by the periodic structure. The defined stop band is the difference between the start frequency when the parallel mode propagation stops and the end frequency when the parallel-plate modes propagate again. The stop-band provided by the periodic structure can be obtained by understanding the behavior of EBG, analyzing a single unit cell, and extracting its dispersion relation with frequency to find the solution of the fields in the three regions.
The key idea behind this technology is based on the procedure to direct the electromagnetic wave through desired directions within the gap between two metal plates and to avoid any propagation along undesired directions. Thus, any leakage occurring in between the divided blocks of a circuit with poor metal connections as well as unwanted radiations can be avoided [83] [84] [85].

A lot of work was accomplished in this research area to design and analyze the unit cell that is repeated in such a structure. In addition, much effort was done to utilize the stop band property of these cells to enhance the performance of microwave and antenna structures.

2.4.2 Metallic wires

The wire medium is an artificial material formed by parallel ideally conducting cylindrical wires arranged into periodic symmetrical lattice with radius r, height d , and with periodicity a and b relative to y and z axis respectively, as shown in Figure 2.11.

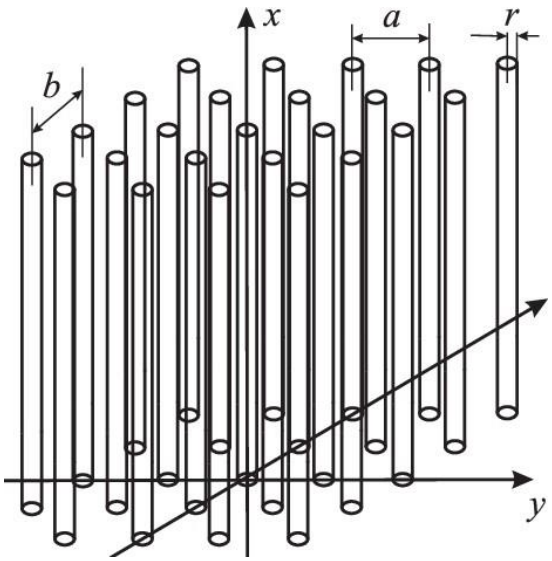

Figure 2-11 Geometry of wire media [86].

This medium has long been recognized as an artificial dielectric with plasma-like characteristics at microwave frequencies [86]**.** After that, it has been demonstrated in [87]. that the wire medium exhibits significant spatial dispersion, which means that the wire medium behaves as a non-local material, and its permittivity tensor in the spectral domain cannot be adequately described only by a frequency-dependent formulation. Instead, the permittivity tensor of the wire medium also depends on the wave vector. For E field polarization along the wires, the periodic pin lattice is regarded as a spatial and frequency dispersive slab of an anisotropic medium whose effective relative permittivity is:

$$\varepsilon(k, q_z) = 1 - \frac{k_p^2}{k^2 - q_z^2} \qquad 2.8$$

This later is characterized by a frequency dependent tensor given by [87]:

$$\bar{\bar{\varepsilon}} = \varepsilon z_0 z_0 + x_0 x_0 + y_0 y_0 \qquad 2.9$$

Here, the z-axis is oriented along the wires, q_z is the z-component of the wave vector q, $k = \omega\sqrt{\varepsilon_0 \mu_0}$ is the wave number of the host medium, and k_p is plasma wave number accounting

for the local spatial dispersion, which is only dependent on the geometrical lattice properties (periodicity of wired along y-direction “a” and periodicity along z- direction “b”), and on the radius of wires.

$$k_p = \frac{1}{a}\sqrt{\frac{2\pi}{\ln\left(\frac{a}{2\pi b}\right)+0.5275}} \qquad 2.10$$

This model is valid only when $\frac{a}{\lambda} = \frac{b}{\lambda} \ll 1$ and the dependence of dielectric permittivity on wave vector q_z does not disappear until the frequency becomes zero.

The expression (2.9) for the permittivity tensor of the wire medium described above is valid under the following specific conditions:

- Much thinner wires compared to lattice periods: meaning that the polarization across the wires is negligible compared to the longitudinal polarization.
- Significantly small lattice periods compared to wavelength of the EM waves passing through the medium: allowing the wire medium to be effectively homogenized.

The wire medium supports three types of modes:

TE Modes (Ordinary Modes): present a transverse E-field with respect to the wires, polarized across the wires (i.e $E_z=0$), and do not induce currents along them (i.e $I=0$). In the thin wire approximation, they behave similarly to modes traveling in free space and propagate without interaction with the lattice

TM Modes (Extraordinary Modes): exhibit a transverse H-field with respect to the wires, resulting in nonzero currents (i.e $I\neq0$) in the wires and nonzero longitudinal component of electric fields along them (i.e $E_z\neq0$). At frequencies below the plasma frequency, these waves are evanescent.

TEM Modes (Transmission-Line Modes): These modes involve nonzero currents (i.e $I\neq0$) in the wires but have zero E-field along the wires (i.e $E_z=0$). They propagate with the speed of light along the wires and can have any wave vector in the transverse direction. These modes resemble the behavior of a multi-conductor transmission line formed by the wires, facilitating the realization of the canalization regime.

The presence of TEM modes highlights the wire medium's significant spatial dispersion. Typically, spatial dispersion effects are observed in periodic structures at frequencies corresponding to spatial resonances, such as in photonic crystals. However, in wire media, spatial dispersion occurs at very low frequencies without resonant effects. This unique behavior distinguishes wire media from other periodic structures in electromagnetics and photonics.

2.4.3 Grounded wires

In this geometry**,** the metallic pins are grounded by a PEC plane. The related structure is called Fakir's bed of nails. This latter, was studied in [88] in order to examine the reflection properties of TE and TM modes. The reported results showed that this kind of medium is able to support three modes: TEM mode, TM-y mode, and TE-y mode. Considering the matching points at the air-medium interface, the reflection coefficients of the TE and TM modes can be calculated by exciting the surface of a Fakir's bed of nails with a plane wave, as shown in Figure 2.12.

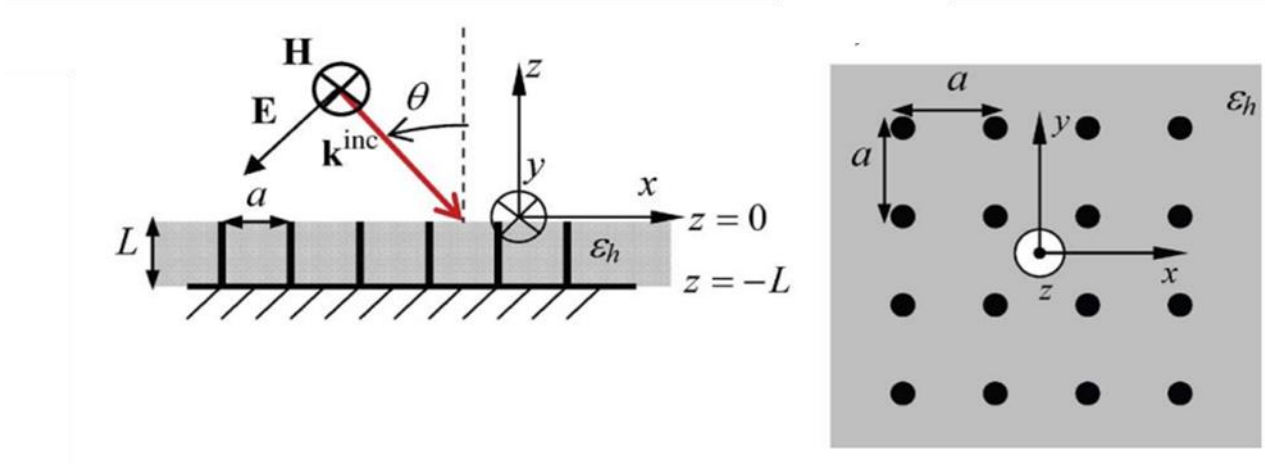

(a) (b)

Figure 2-12 Geometry of the "Fakir's bed of nails" substrate panel (a): side view; (b): top view [88].

The textured surface is formed by a square lattice of metallic pins, embedded in a dielectric substrate with permittivity ε_h and height L. The pins are connected to the PEC ground plane with periodicity spacing a, and the incident wave vector K^{inc} is shown in red line with incidance angle θ from the noraml vector z.

The surface impedance of such a structure is expressed as follows [88]

$$Z_S = j\eta_0 \frac{1}{\sqrt{\varepsilon_h}} \tan(\beta_h L) \qquad 2.11$$

Where, Z_S is surface impedance, $\beta_h = \beta\sqrt{\varepsilon_h}$ is the wave number in the host material , $\beta = \omega/c$ is the wavenumber in free space and η_0 is the intrinsic impedance. The expression for Z_S remains unaffected by the angle of incidence due to the influence of the metallic wires. It is crucial to emphasize that this significant characteristic holds true only for tightly packed wires. If the wires are not densely arranged, spatial dispersion effects must be taken into account, making the surface impedance dependent on the angle of incidence and complicating the prediction of surface impedance and EM wave behavior.

2.4.4 EBG ground + top

By enclosing the upper and lower sides of the bed of nails with metallic plates, as shown in Figure 2.13, a parallel plate waveguide (PPWG) is created. The top plate acts as a PEC, while the bed of nails along with the bottom plate act together as a homogenized surface.

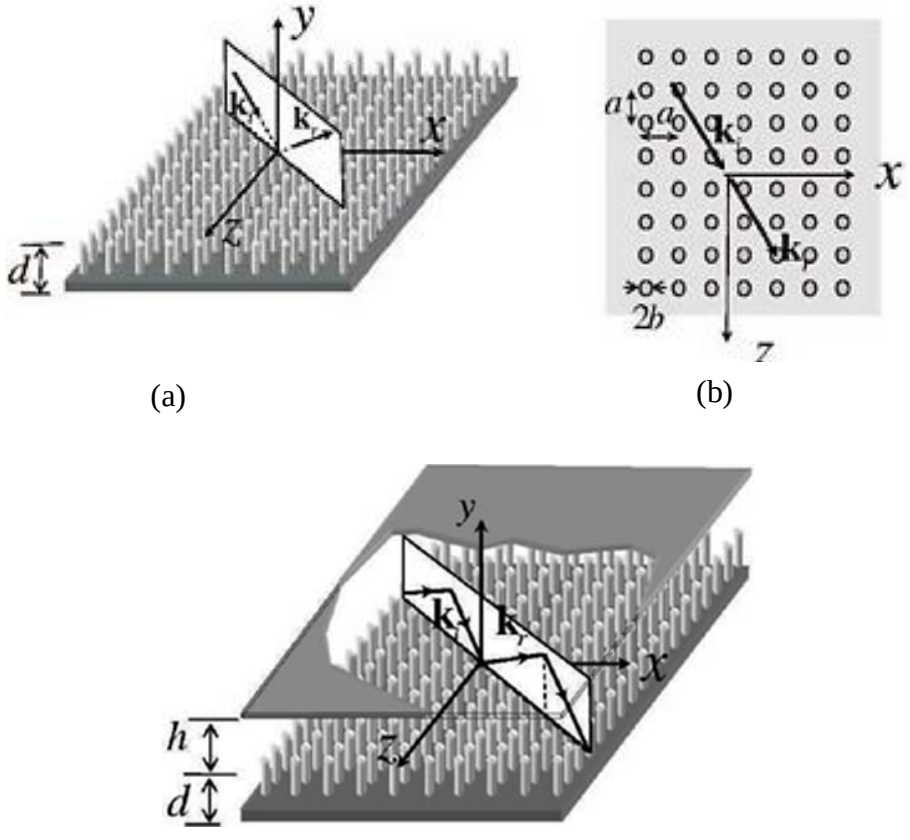

(a) (b)

(c)

Figure 2-13 Parallel plate bed of nails basic geometry. (a) 3D-view. (b) Top-view. (c) Reflection phenomenology supported by the bed of nails surface covered by a PEC plate.

The wave in such configuration bounces in the gap between the two surfaces. By applying appropriate boundary conditions, the propagation constant can be determined in the y-direction for both cases of the TE and TM modes. The TE and TM dispersion equations of this periodic structure can be expressed as follows [89]:

In absence of the dielectric background in the bed of nails, TE mode solution that is associated with the resonance between the upper and lower PEC wall is

$$\mathrm{k_y} = \frac{\pi}{\mathrm{h+d}} \qquad 2.12$$

Where k_y is the propagation constant in y-direction, d is the hight of the conducting pins and h is the air gap as described above.

Whereas, For the TM mode,

$$\frac{k_y}{k}\tan(k_h h) + \left[1 - \frac{k^2 - k_y^2}{k_p^2 + k^2 - k_y^2}\right]\tan(kd) + \frac{k^2 - k_y^2}{k_p^2 + k^2 - k_y^2}\frac{\sqrt{k_p^2 - k_y^2}}{k}\tan(\sqrt{k_p^2 - k_y^2}d) = 0 \qquad 2.13$$

Where $k_h = \sqrt{\varepsilon_h}k$ 2.14

is the wave number of the host medium and

$$k_p = \frac{1}{a}\sqrt{\frac{2\pi}{ln\frac{a}{2\pi b} + 0.5275}} \qquad 2.15$$

is the plasma wave number accounting for local special dispersion [90], only dependent on the geometrical properties.

The value of k_y is the solution of a transcendental equation which is obtained from bouncing the wave in the gap between the two surfaces. The periodic bed of nails' dimensions are chosen to be the same as the dimensions presented in [89] where the height of the unit cell is d = 7.5mm , the radius b = 0.5mm, the air gap h = 1mm and the unit cells' period a = 2mm.

The eigenvalue solution is real or imaginary in three frequency regions, separated by vertical dashed lines. Moreover, in Figure 2.14 the TE eigenvalue and light line are depicted in constant short- dashed line and long dashed line, respectively.

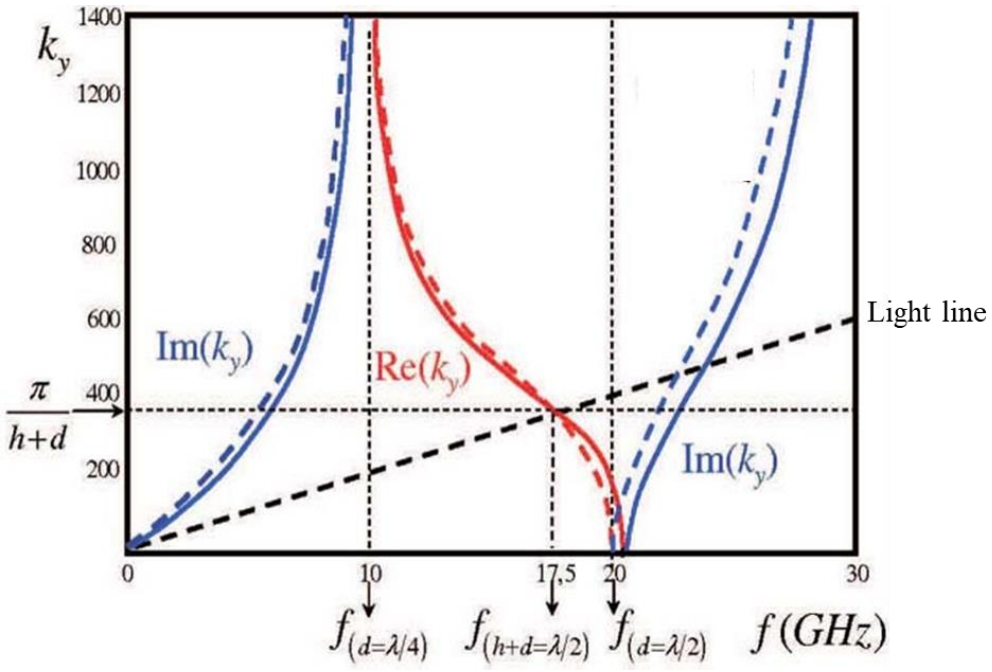

Figure 2-14 TM dispersion equation of the complete form (solid lines) and approximated form (dashed lines).

A Matlab code is then utilized to solve equation 2.13, generating the dispersion curves (k_y^{TE}, k_y^{TM}) and detailing the dimensions of the periodic bed of nails. The TE solution, shown in Figure 2.14, remains consistent across frequencies as illustrated by the constant dashed line. The light line is also displayed by the solid curved line.

Meanwhile, the TM solution exhibits three distinct regions: the first and third regions span from zero to $f_{d=\lambda/4}$ and $f > f_{d=\lambda/2}$, respectively, with k_y being purely imaginary. This indicates the presence of a TM wave propagating along the surface of the pins. The second region comprises two sub-regions, both with purely real k_y values. In the frequency region between $f_{d=\lambda/4} = 10GHz$ and $f_{d+h=\lambda/2} = 17.5GHz$,the wave vector k_y exceeds the value of the light line, indicating attenuation in all directions along the surface. This interval represents the stopband of the structure. In the second sub region between $f_{d+h=\lambda/2}$ and $f_{d=\lambda/2}$ the propagation of both TE and TM is allowed with the upper bound being the cutoff frequency of the first TE mode. In other words the upper cutoff of the stopband corresponds to the lower cutoff frequency of TE mode.

The accuracy of these dispersion equations is validated by comparing them with simulation results obtained from the HFSS Eigen mode solver. The dispersion diagram plotted in Figure

2.15 clearly confirms the stopband from 10GHz to17.5Ghz, where the dispersion relation that describes the relationship between frequency and the propagation constant in the z-direction is expressed as

$$k_z = \sqrt{k^2 - k_y^2} \qquad 2.16$$

This gap indicates the absence of wave propagation on the bed of nails within this frequency band.

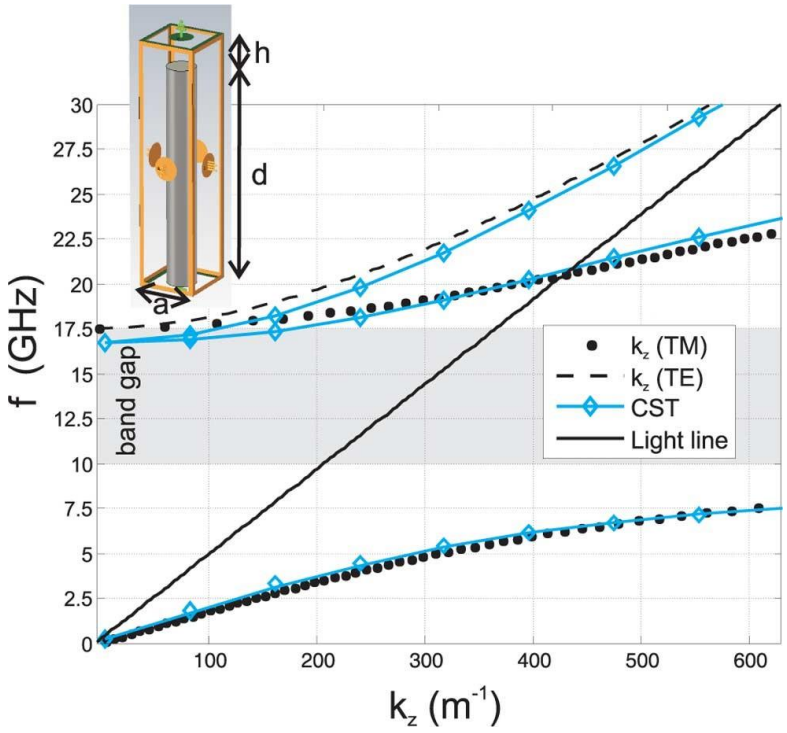

Figure 2-15 Frequency vs real part of TM (black dots) and TE (dashed line) solutions of the pertinent eigenvalues problems.

The unit cell is the basic building block of the RGW. These cells can be of many shapes to obtain different operating frequency ranges. The basic shape published in the first trials of the RGWs and which will be later used in this work, is the nail with circular and rectangular cross section [91].

2.5 Modern wave guiding technologies

In recent times, many guiding structures based on innovative technologies such as Substrate Integrated waveguides (SIW) and Gap Waveguide technology (GW) are introduced as a promising candidate to overcome the problems experienced with traditional methods cited earlier. These structures mostly emphasize the high-frequency range, such as MMW bands.

2.5.1 SIW technology

Designing microwave antennas with very low phase noise, compact size, and high-gain at high frequencies became easier due to the high Q factor of waveguides based on SIW cavity resonators. This advancement has launched as a promising start to compensate for the previous guiding techniques drawbacks.

Planar cavity SIW resonator illustrated in Figure 2.16 is a type of transmission line structure that combines the advantages of traditional rectangular waveguides with the integration benefits capabilities of planar circuits. It was first presented in [92], and further detailed in [93], gaining significant attention over the past decade in modern communication systems. This is due to its attractive system performances, such as low cost techniques (as they are buildt based on inexpensive PCB fabrication, compact size, low loss (their insertion losses are usually less than 0.4dB/m which is lower than a micro-strip line in the Ka-band [94]). SIW resonators also offer integration flexibility for designing various microwave circuit components on the same substrate, compared to traditional planar PCB microwave resonators.

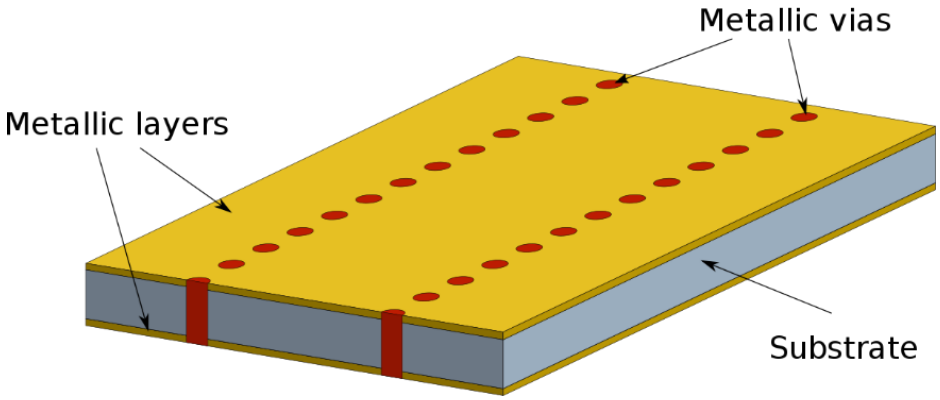

Figure 2-16 Planar cavity SIW resonator.

The main advantages of the SIW technology are due to its structure's planar form, strength of construction, high power operation capability, high efficiency, small thickness, light-weight and wide BW at higher frequencies. It was suggested in [95] to diminish the radiation loss over long distance communication sequential feeding network via-SIW, which minimized the radiation losses and showed significant improvement in terms of BW and gain. SIW can achieve the same functionality as traditional waveguides but in a lower scale dimensions, enabling integration into modern electronic devices. Besides, it offers good isolation between different circuits on the same substrate, reducing the interference and coupling effect.

The SIW structure consists of a parallel double side conducting planes on top and bottom with dielectric substrate; and grounded by metalized via holes that act as a metallic sidewall in hollow waveguides to prevent the horizontal surface currents from flowing in the SIW.
The via diameter and the spacing between them play a significant role in controlling the leakage in SIW structure. According to [96], to decrease the leakage, two conditions must be considered in the design of SIW structures: the diameter of the via (d) must be less than λ / 5 ($d < \lambda / 5$) and the periodicity of the vias (p) should be less than 2d ($p < 2d$).

Unlike solid-sided rectangular waveguides that support both TE and TM waves, SIW predominantly supports the TE wave (TE_{10} mode); this is why it is considered as an integrated alternative to the conventional bulky waveguides [97] where the cut-off frequency f_c is given by:

$$f_c(TE_{10}) = \frac{c}{2W_{eff}.\sqrt{\varepsilon_r}} \quad 2.17$$

Where W_{eff} is the effective SIW propagation width, c is the speed of light, and ε_r the permittivity of the dielectric material. The corresponding E-field of the fundamental mode is demonstrated in Figure 2.17.

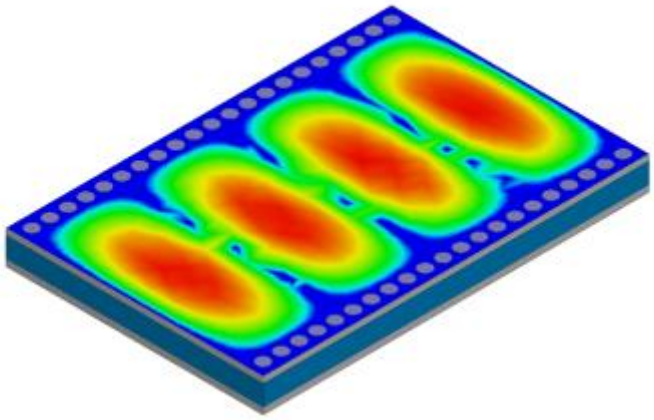

Figure 2-17: Electric fields distribution of the fundamental mode (TE_{10}) of the SIW cavity resonator [98].

While SIW exhibits similar dispersion characteristics to standard waveguides, it does not provide a perfect metal shield due to potential signal leakage through periodic gaps between adjacent conducting via sidewalls, which can lead to mode conversion losses when its fundamental TE_{10} is interfacing with other TEM or Quasi-TEM transmission lines.
At higher frequencies, the design of SIW structures encounters many challenges due to unknown dielectric characteristics that are beyond the standard lower frequency bands

covered in available laminate datasheets. Consequently, causing ambiguity and uncertainty at the design procedure since they demonstrate certainly a different behavior than the lower frequencies.

From the other side, dielectric losses increase significantly at MMW bands, affecting the average power handling capabilities compared to air-filled waveguides. To mitigate these losses at high-frequency applications, air-filled SIW structures have been proposed [99]. The latter configuration's idea consists of removing the dielectric material of the propagation medium between the via-holes. Unfortunately, there is currently no technology available to build such a structure. According to the available machining theologies, the optimum way to realize the air-filled SIW involves making an air-cut in the dielectric material of the central section, and since the copper cladding of the dielectric laminate is extremely thin, the top and the bottom ground planes are covered with thick metal plates.

The initial model was introduced in [99] based on a multilayer PCB and focused on using computational analysis to investigate the attenuation constant and cutoff frequency of the air-filled SIW. Later on, in studies conducted in [100], [101], and [102] the air-filled SIWs has been successfully implemented on multi-layer PCB and connected to a transition from a dielectric-filled SIW into microstrip line. The obtained results has proven their superiority over conventional dielectric-filled SIW in terms of loss, Q-factor, and power handling capabilities.

All PCB-based multi-layer air-filled integrated waveguides introduced so far in the literature require flawless and seamless connections on the top and bottom layers to the intermediate substrate. This is mainly due to potential wave leakage from the possible infeasible air gaps that might exist between the top and the bottom conductors and the intermediate substrate holding the via-holes. In other words, the performance of such air-filled integrated waveguides depends heavily on the quality and perfection of the top and bottom metal plates' connection to the intermediate layer, as they are prone to leakage from any discontinuity or poor connection between layers.

In the prototypes discussed in [103] and depicted in Figure 2.18, tight connections are achieved using numerous closely spaced screws around the waveguide. This mechanism of tight connection around the waveguide impedes its utilization for the designs where the SIW lines are closely located and have to be sealed to protect any leakage between the lines. This can be overcome by two alternative methods. The first technique involves connecting the

upper and lower conductors with a conducting adhesive and press firmly to assure the electric contacts. The second possible method consists of gluing the top and bottom conductors to the intermediate substrate before making the via-holes. The second method seems more realistic and assures the electrical contacts. However, achieving seamless connections between layers in multi-layer air-filled integrated waveguides remains crucial to prevent wave leakage. Current methods involve tightly connecting layers with screws or using conducting adhesive or glue, though challenges persist with adhesive leakage and manufacturing precision, particularly in wide circuits.

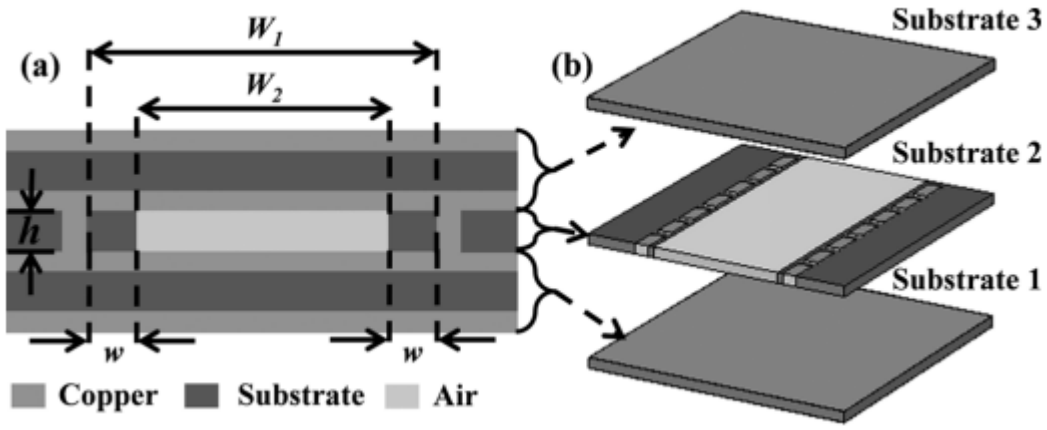

Figure 2-18 Air-filled SIW. (a) Cross-sectional view. (b) Structure.

SIWs structures offer numerous advantages over conventional waveguides, but they also come with certain disadvantages. For example, if the dielectric substrates are thick, restrictions are applied to the via-hole diameter that might make the design impossible.

In addition, utilizing glue between the layers that are partially depleted is not a reliable solution, especially for the wide circuits because there is a possibility of leaking adhesive glue inside the air-filled region, which is sometimes completely out of control and demands complex and expensive fabrication procedure with high precision. Furthermore, integrating SIWs with other components or technologies, such as transitions to microstrip lines or connectors, can pose integration challenges and require additional engineering effort. Finally, SIWs can still experience limited BW and higher propagation losses compared to conventional waveguides particularly at high frequencies, which can restrict their use in broadband applications and over longer distances. However, SIWs continue to have valuable considerations in various applications such as filters, antennas, couplers and power dividers

where their compactness, low-profile design, and unique electromagnetic properties outweigh these challenges.

2.5.2 Gap Waveguide

The idea of GW technology was introduced in early 2009 by Kildal [91] as an extension of soft and hard surface work. This new version of guiding structure offers attractive potential that can significantly overcome the problems of conventional transmission technologies. Moreover, it can be used in the design of MMW band components and antennas. The core operation principle is driven from the basic cutoff of a PEC-PMC parallel plate waveguide configuration where the EM bandgap of the structure is controlled by the PEC-PMC plates that are placed in parallel. Thus, no propagation would occur in any direction [104] .

The GW configuration principle as depicted in Figure 2.19, is completed by inserting continuous PEC guiding structures in the form of a ridge, groove, or strip inside the PMC surface bounded by the upper ground plane. This will allow a wave propagation within the PEC/PEC area only and waves in other directions are evanescent when $h < \lambda/4$ for the vertical polarization (TM_n case) and when h is $\lambda/2$ for the horizontal polarization (TEn case). Thus, the proper gap must be less than $\lambda/4$ [91] to ensure a complete stopband for any potential surface waves in the PEC-PMC region.

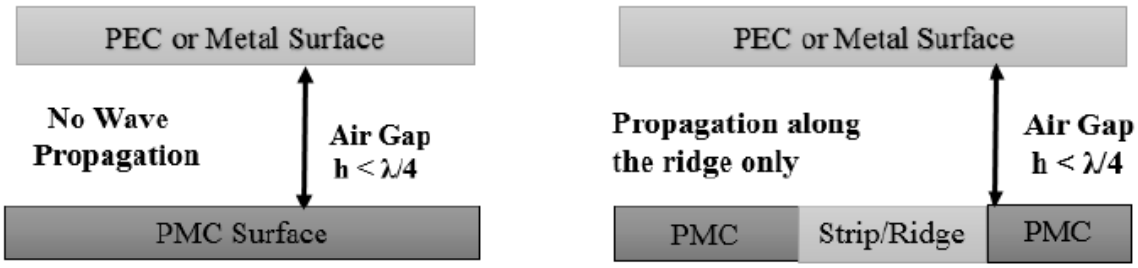

Figure 2-19 GW configuration principle.

The GW guides the wave in the form of a quasi-TEM mode , in which the PMC boundary around the ridgeline stops the leakage and confines the wave, so that the wave propagates only within the air gap between the ridgeline and the top plate. This is also the case for microstrip and Inverted Microstrip Gap Waveguides (IMGW), where the field propagates in the air gap between the upper plate and stripline as a quazi-TEM as well. In Groove Gap Waveguides (GGWs), the field propagates as a TE mode along the groove.

Since the wave is confined and propagated within the air gap, these structures avoid the dielectric losses commonly associated with microstrip and SIW technologies. In addition, unlike metal waveguides, a GW does not need any electrical contacts. Moreover, the RGW can be implemented in the printed form (PRGW) for easy integration with other planer system components.

As illustrated in Figure 2.20, the GW can be classified into the following types:

a) RGW

b) GGW

c) IMGW

d) Microstrip Ridge Gap Waveguide (MRGW)

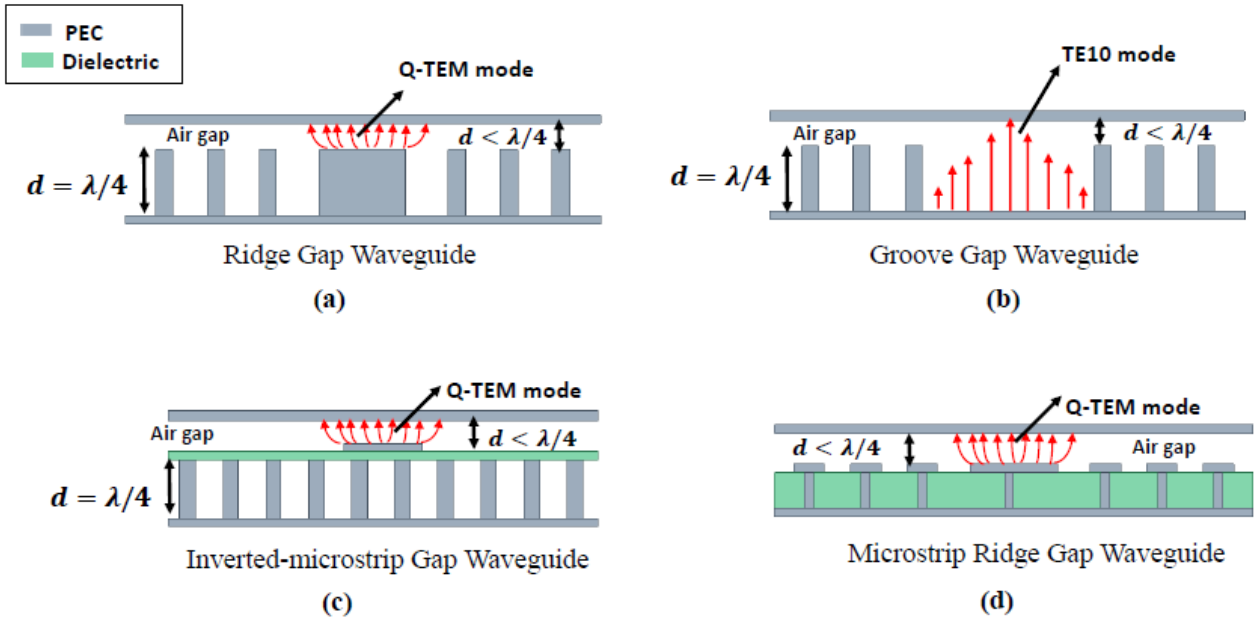

Figure 2-20 Types of PRGW.

2.5.2.1 Ridge gap wave guide

RGW technology is one of the promising guiding structures for higher frequency circuits and passive devices. It was firstly published by Kildal in 2008, and patented by the same professor later in 2010 [91]. This technology can be considered as a new type of metamaterial-based guiding structure that supports quasi-TEM mode propagation with significant low transmission and radiation losses along with a wide operational BW.

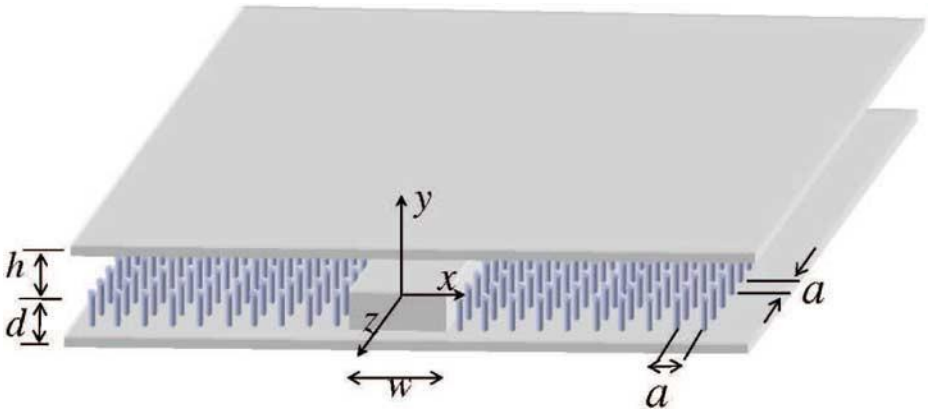

Figure 2-21 Geometry of the RGW embedded in a bed of nails.

The design procedure of RGW starts by the bed of nails unit cell. First, the dispersion diagram is established using simulator HFSS as shown in Figure 2.22.

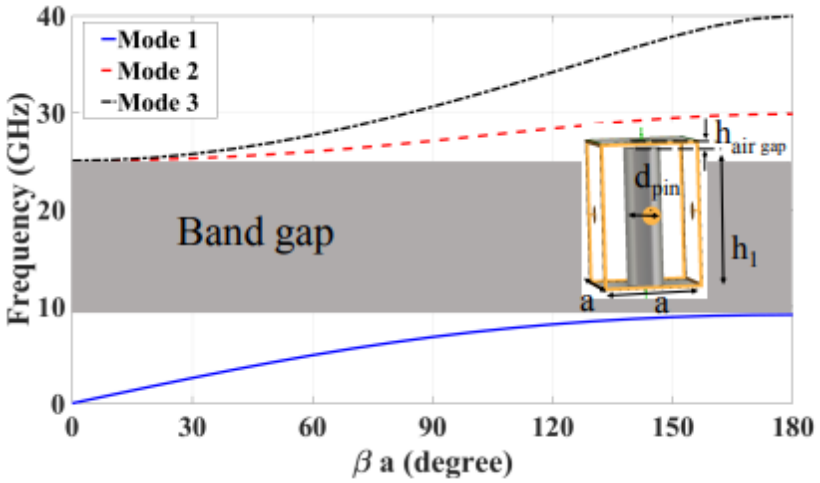

Figure 2-22 EBG unit cell dispersion diagram.

After that, parallel plate GW is realized by inserting a conducting ridge of width "w" into the bed of nails structure, thus leading to the structure in Figure 2.21. From an intuitive point of view, a quasi-TEM modal field is expected to propagate along the ridge where the bed of nail region exhibits a bandgap for surface waves. This mode will match the evanescent modes supported by the surrounding cutoff structure in which only the first TM and TE modes will be present. In particular, in order to achieve the field confinement in the ridge region, the cutoff modes will decay laterally away from the ridge; this can be clearly seen by establishing a dispersion diagram for the line segment of the structure as shown in Figure 2.23.

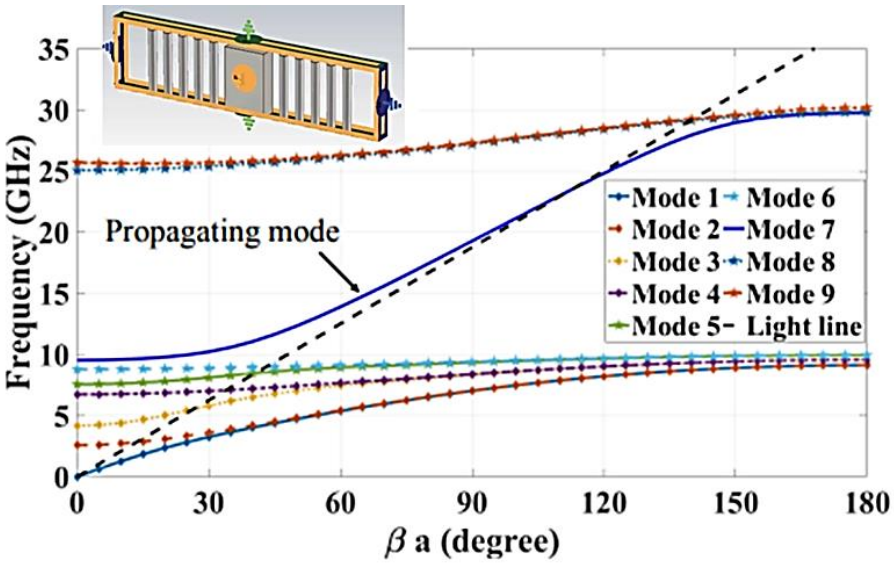

Figure 2-23 Dispersion diagram of RGW line segment.

The single dispersive-less mode propagation at the available stop band can also be extracted by the dispersion analysis of the cells in the existence of the ridge. Numerous research works has been done to acquaint with various unit cells of multiple forms to expand the operating BW [105] [106].

The E-field distribution along the line

Another level of verification for the previously introduced bandgap concept is to study the field distribution along the ridge surrounded by the bed of nails. This simulation is subjected to make sure that the EM waves of the waveguide are bounded by the ridge itself inside the operating frequency that refers to the stop band frequency provided by the bed of nails. Figures 2.24 (a) and (b) demonstrate the amplitude of the components of E-field and H-field, respectively, as taken from the work of [89]. It can be seen from this latter that the leakage occurs beyond the operating BW, while the E-field distribution is tightly bounded to the ridge at central frequency. In this example it is clearly recognized that the bed of nails surface stops propagation along the lateral direction and keeps the desired confinement of the E-field in the ridge region for frequencies within the stop band of the bed of nails region. Whereas, the H-field components appear less confined within the normalized code of the colors.

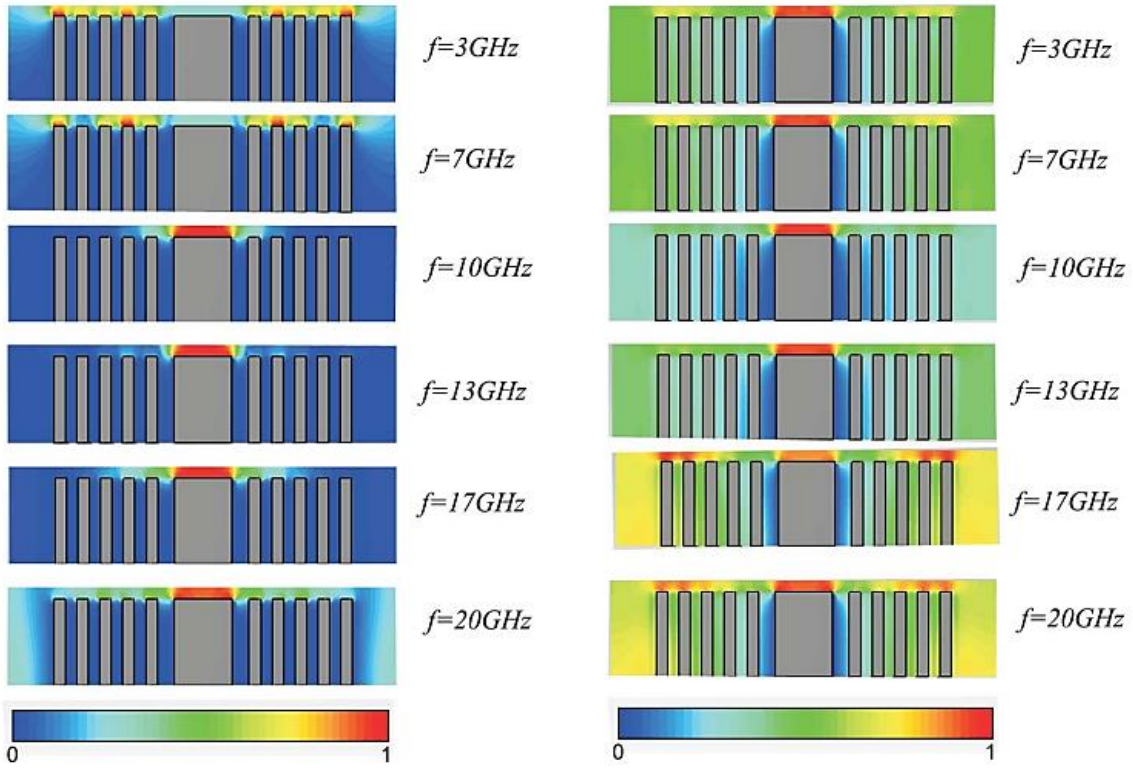

(a) (b)

Figure 2-24 Normalized field distribution in the RGW at different frequencies. (a) E-field. (b) H-field.

The basic operation principle relies on alternating PEC and PMC strips in parallel to a conducting sheet at a distance smaller than a quarter wavelength (λ/4) above them [107], so that the waves are propagating only along the longitudinal direction while they stop after placing the PEC-PMC strips along the crosswise orthogonal direction.

In modern configuration, the RGW consists of two parallel conducting plates, where one is perturbed with a textured surface of periodic unit cells on both sides of a central PEC embedded ridge to form a guiding structure for the propagating quasi-TEM wave. The main motivation for using such textured structures is to obtain a HIS boundary condition, which, together with the smooth upper plate, produce a stopband for parallel-plate modes. Consequently, potential surface waves from the dielectric substrate are eliminated and thus the signal leakage is prevented in unwanted directions except in the longitudinal direction through the air gap between the two parallel metallic plates, which significantly plummet the radiation loss. In other words, RGW structure has the ability to create a bandgap for wave propagation in the undesired direction such that the signal path is a parallel plate-like structure

surrounded by PEC-PMC parallel plate through which the propagation of the EM signal is forbidden.

This type of structures have been widely used in literature to improve the performance of devices, such as antennas, waveguide structures, filters, etc., using patches of different shapes (square, circular, hexagonal, etc.) [108], [109] and [110].

Printed Ridge Gap Waveguide PRGW

In this work, we are most interested in the PRGW micro-strip printed version which was introduced in [111] and [112] and further developed in [113], [114] and [115]. A 3D view of the PRGW conceptual geometry is shown in Figure 2.25 with the upper ground plane removed to show the configuration details. It is basically realized by two horizontal parallel PEC layers that doesn't need tight contact during assembly. Its lower layer consists of a metallic strip ridge-line printed on dielectric substrate and surrounded by a bed of nails that acts as PMC on both sides of the ridge line while the upper layer is a flat metallic PEC plate.

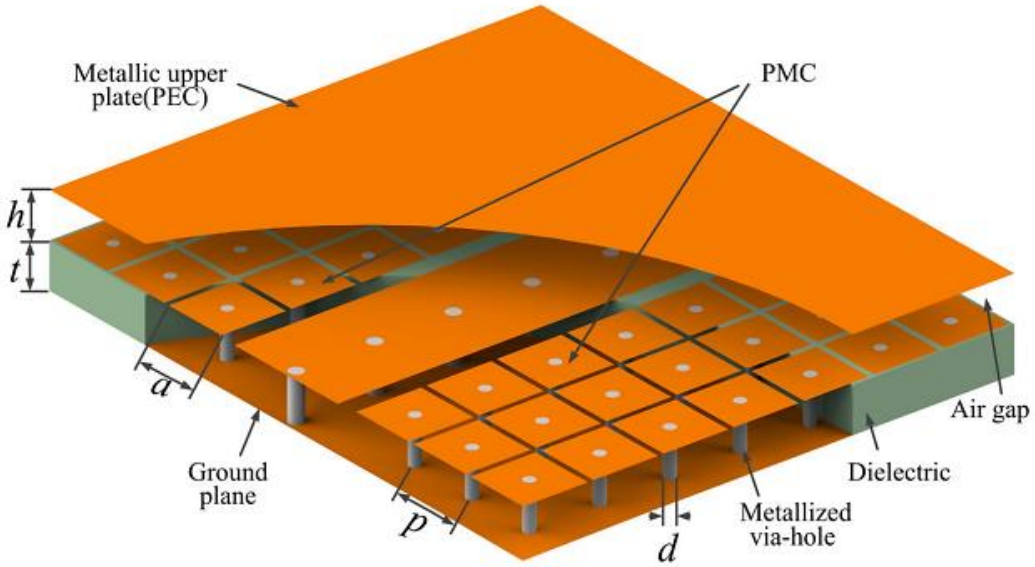

Figure 2-25 PRGW structure [116].

The design procedure of PRGW consists of two major parts. Initially, the periodic EBG structure should be designed to cover a specific frequency band as shown in Figure 2.26 that demonstrates the bandgap obtained in [117].

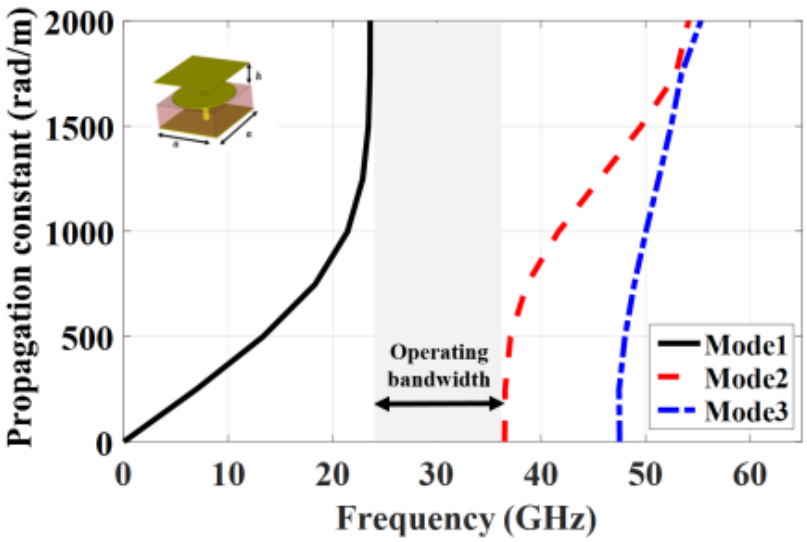

Figure 2-26 EBG unit cell dispersion diagram.

After that, the dimensions of the ridge are calculated to have a 50 Ω transmission line. Different approaches can be taken to calculate the characteristic impedance of the transmission line. A closed form equation was introduced in [118]**.** The PRGW is usually fed by microstrip line with a thickness equal to the gap height of the waveguide.

As stated earlier, the condition of the PRGW to operate is to have the gap between the top and bottom plates less than a quarter of the guided wavelength (< λ/4) at the highest operating frequency to provide a parallel-plate stopband around the ridge in order to stop the leakage outside the ridge area. Meanwhile, the Quazi-TEM mode will be totally confined and propagates along the air-gap above the ridge guided by the two horizontal PEC plates towards the desired direction instead of spreading out. It should be stated that the RGW's characteristic impedance varies versus frequency over the bandgap provided by the EBG structure. Therefore, RGW should be categorized as a quasi-TEM medium, and not TEM. Finally, in order to suppress any of the possible propagating modes under the continuous printed ridge within the substrate, a single row of metallic vias is placed under the guiding ridge connecting it to the ground. The height of the substrate is usually less than a tenth of a wavelength ($h < \lambda /10$).

To verify this conditions a dispersion diagram of the line segment of the structure had to be plotted, as displayed in Figures 2.27 to prove that only one mode is propagating inside the ridge area.

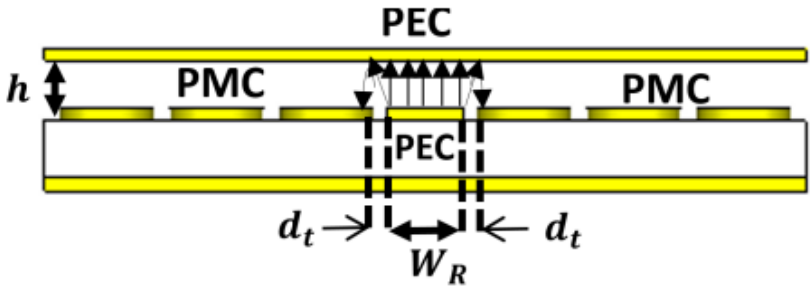

(a)

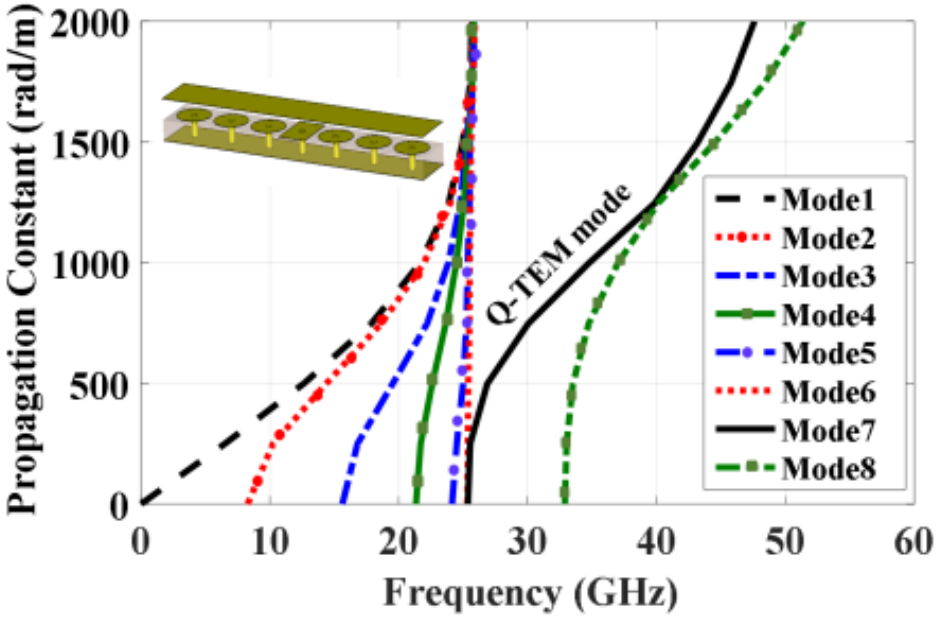

(b)

Figure 2-27 (a) Line segment of PRGW. (b) Dispersion diagram of PRGW line segment [117].

Additionally, in order to further demonstrate that the designed cell effectively confines the E-field above the ridge and minimizes leakage, the E distribution is plotted over the structure, as shown in Figure 2.28. This figure indicates that the E-field decays at a rate of approximately 60 dB/λ. For further validation, the E-field distribution was calculated and plotted across various frequency bands, as illustrated in Figure 2.29. This analysis reveals that the E-field remains confined within the intended frequency band, with leakage occurring outside this range.

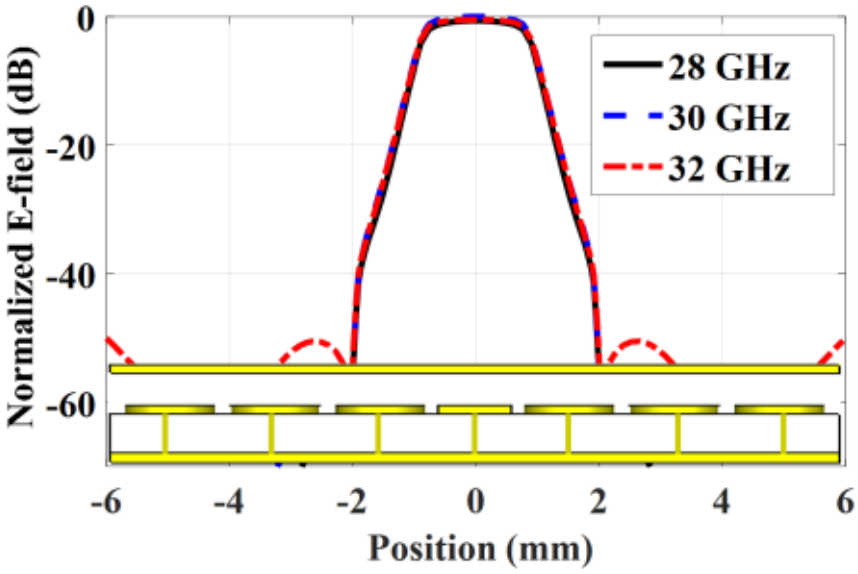

Figure 2-28 Simulated normalized field distribution of the GW in transverse plan for different frequencies [117].

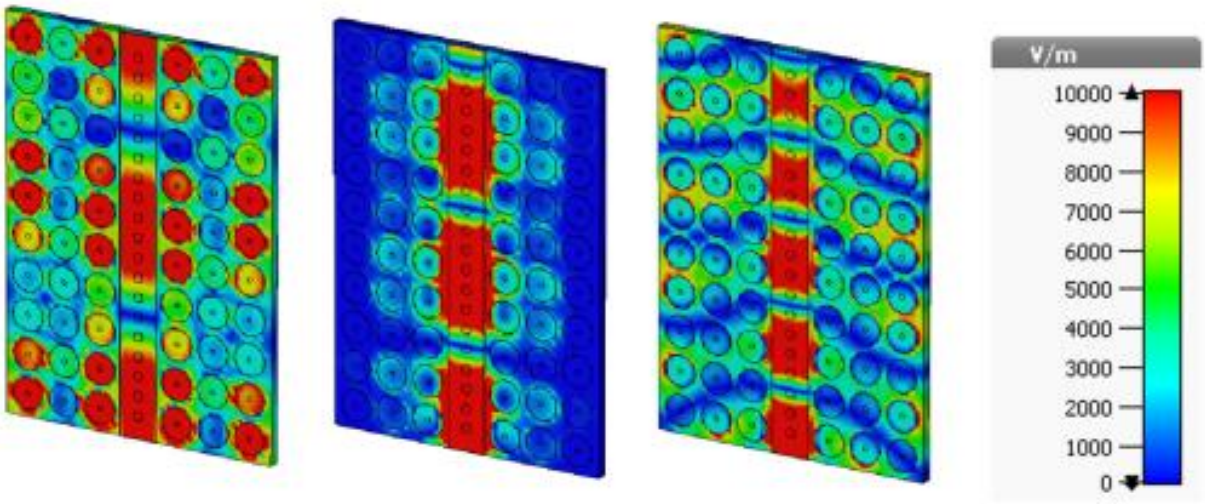

(a) (b) (c)

Figure 2-29 E-field distribution at (a) f=20 GHz, (b) f=30 GHz, and (c) f=40 GHz [117].

However, since the PMC boundary is not available in nature, it is realized as the AMC to cover a specific frequency band by using periodic structure in both two-dimensional spaces . The first AMC in the RGW is realized by the " Fakir's bed of nails" [119] [120]. In this type, the ridge is a micro-strip line printed on a dielectric substrate using available laminates of PCB technology.

The bandgap of the bed of nail's unit cell depends on four parameters: the air gap between the two conducting plates, the height of the pin, the radius of the pin, and the distance between adjacent pins. A detailed study to investigate these effects can be found in [83]. Moreover, the existence of the ridge has a significant effect on the BW. Based on the requirement it is possible to choose the band gap by changing the geometry parameters. For the BW enhancement of the periodic structures, different shapes of periodic cells were analyzed to increase the realized bandgap [121].

Since the PRGW waveguides were proposed only a few years ago, they became the focus of attention of the researchers as an alternative approach for MMW applications for several reasons:

- **Reduced losses**: RGW is an air-filled guiding structure that has no dielectric loss since it does not require a dielectric substrate to operate. In addition, it has a negligible level of radiation loss and surface waves; the only possible losses are mainly attributed to conductor losses due to finite conductivity, which may be reduced by electroplating. Since GW does not rely on any dielectric medium, the dielectric loss is avoided considerably.
- **Large BW:** RGW offers a wide band transmission BW with wider isolation between dominant mode cutoff and higher order mode cutoff; which implies a larger usable single-mode BW [122]. These features have been proved by different authors using different techniques like changing the shape of the unit cell [123] and decreasing the gap height above the bed of nails in some cases [124]**.**
- **Manufacturing flexibility and self-packaging ability** : most waveguides are normally manufactured in split blocks using Computer Numerical Control (CNC) machining or 3D printing, that are attached together; thereafter, they use tightening screws to provide tight contact between the parts. At high frequencies, the screws might not be tight enough for the waveguide to operate without leakage loss through the edges. Meanwhile, this tight screw contact is not necessary for the RGW since it depends on having a gap between the upper and lower plates and the bed of nails blocks the propagation at the sidewalls.
- **Affordable cost**: one of the advantages of the GW is that there is no connection between the upper and lower metallic surfaces, which makes them a suitable choice of low fabrication cost. As the manufacturing cost of PCB fabrication is significantly

lower compared to CNC machining, PRGW is an interesting solution for high-frequency microwave devices.

- **Quazi-TEM propagation**: the benefit of Quazi-TEM is that the media is almost non-dispersive, where the phase velocity and the characteristic impedance are constants over a wide band. Moreover, the TEM mode has a cutoff frequency about zero Hertz, which enables this mode to carry any signal at any frequency.
- **Compact size:** in terms of size, the width of the RGW with two rows is smaller than the width of the GGW for the same frequency band. Moreover, the mechanical durability for both RGW and GGW components is quite impressive [125]**.**

These features highlight this technology as a suitable candidate for MMW and Sub-MMW bands guiding structures for realizing better performance radiating systems.

Challenges with conventional RGW

The RGW technology was widely used at higher frequencies because of supporting the Quazi-TEM propagation mode with significant low loss. However, the propagating mode is still relatively dispersive in comparison to the pure TEM propagation mode, which can propagate in the air medium.

In the conventional RGW structures, the Quazi-TEM propagation occurs because the outer part of the field (fringing) experience a different propagation environment, resulting from the entire upper ground plane parallel to the ridge area, which can also be seen as an air filled microstrip line. Thus, even if the HIS surface in the lower part provides a stop band in the area around the ridge, the propagation is not totally confined within the ridge area. The extended upper ground plane is not intended to cut the continuity of the waves outside the ridge borders, which causes a lot of fringing fields outside the ridge boundary. Accordingly, the first row of EBG unit cell after the ridge borders, suffers from strong fringing fields continued by the upper plane and cannot operate adequately to suppress the whole power around the ridge. This will drastically decrease the Peak Power-Handling Capability (PPHC) of the structure, implying that several rows of cells must be considered to provide better propagation suppression or to weaken the coupling between adjacent RGW lines, which enlarges the components and devices made with this technology.Moreover, the horizontal asymmetry of the propagation medium between top and bottom layer of common RGW structure indicates that the preparation mode is characterized as a Quazi-TEM and not a pure TEM.

2.5.2.2 GGW technology

The Groove Gap Waveguide (GGW) is a special version of the RGW technology that was first proposed in [126]. In terms of geometry, the concept of GGW is based on replacing the ridge by a metal groove embedded with pins on both sides as illustrated in Figure 2.30.

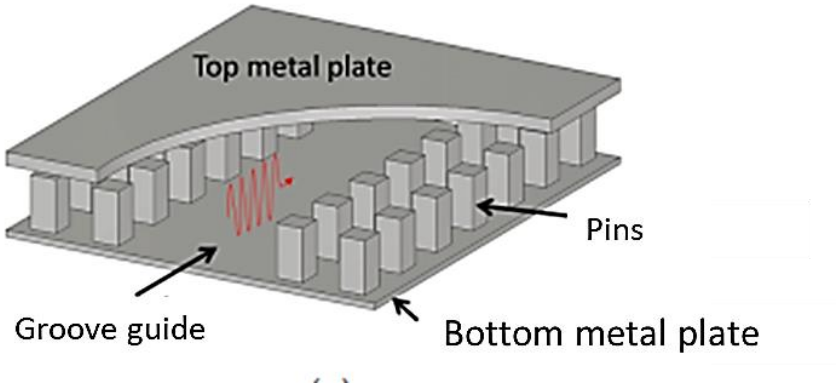

Figure 2-30 GGW structure.

In order to create a controlling path for the EM wave propagation in a desired direction inside a parallel plate waveguide where no EM wave can propagate, the distance between the top and bottom plates must be less than $\lambda/4$ and one of them must be embedded with a PMC lattice. In this particular case, the PMC surface consists of a 2D periodic structure of short-circuited conducting pins. Such designs, offer wider BWs and lower losses, especially at high frequencies, because they are made of metal material.

Furthermore, GGWs have shown their potential advantage versus conventional waveguides especially at the MMW frequency range by offering a highly simpler mechanical assembly where it can be easily manufactured by available machining methods.

The GGW can take two versions, vertical polarization (VP), and horizontal polarization (HP), as depicted in Figure. 2.31 (a) and (b) respectively. The propagation region in both versions behave in a similar way as conventional rectangular waveguide; it can propagate TE or TM modes depending on the cross-sectional dimensions. It is noteworthy that the dominant mode (TE_{10}) is utilized in most practical cases.

The preliminary step towards the design of GGW is to accomplish a band gap with PMC/PEC structure in a frequency band around the desired operating frequency of the antenna. In reality, the PMC plane is artificially formed by an array of conductive pins. The geometrical parameters affecting the stop-band are the air gap “h” between the AMC and PEC planes, the width “a”, the height “d” and the periodicity of the pins “p”.

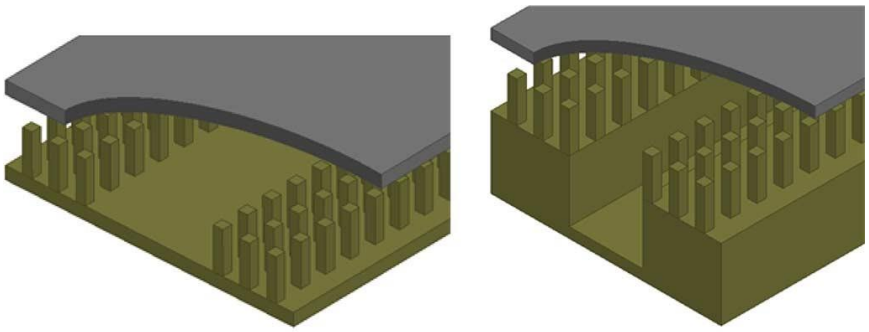

(a) (b)

Figure 2-31 GGW polarizations. (a) GGW-VP. (b) GGW-HP.

The design starts with approximate dimensions of the pin array following the guidelines presented in [124].This is performed by employing optimization tools and the Eigen mode solver in CST Microwave Studio in order to obtain the dispersion diagram of the bandgap structure unit cell formed by the parallel PEC and AMC planes.

Figure 2.32 (b) illustrates the simulated unit cell of a GGW structure, which is surrounded by periodic boundary conditions. The design parameters are taken as a reference, to be (a = 1 mm, d = 6.25 mm, p = 2.7 mm, and is h = 1 mm) in order to create a relatively wide stop-band ranging from 11 to 19 GHz that covers the desired operating frequency of the antenna (f = 14 GHz in this case). The corresponding dispersion diagram of the structure is depicted in Figure 2.32(a), and Figure 2.33 show a cross section and the dispersion diagram of GGW line.

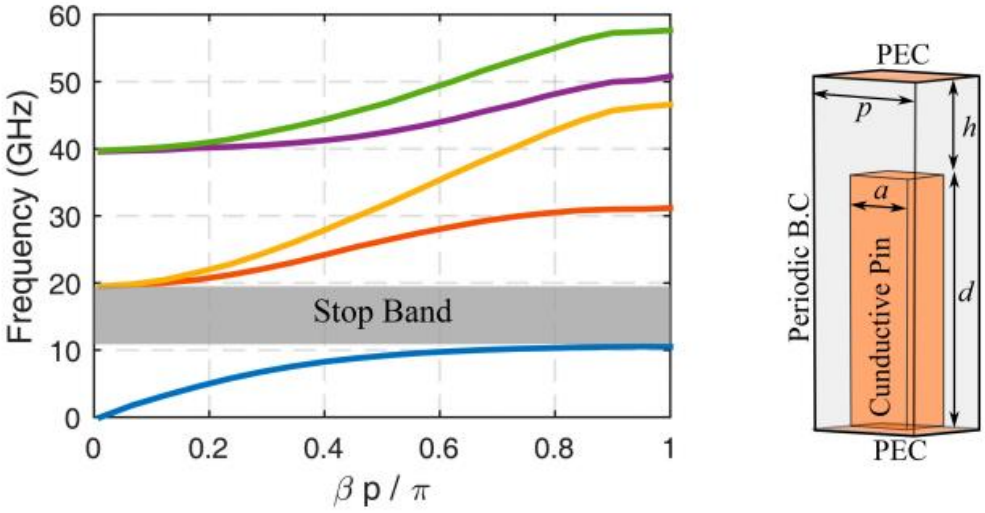

(a) (b)

Figure 2-32 (a) Dispersion diagram for the band gap structure (b) Simulated unit cell [127].

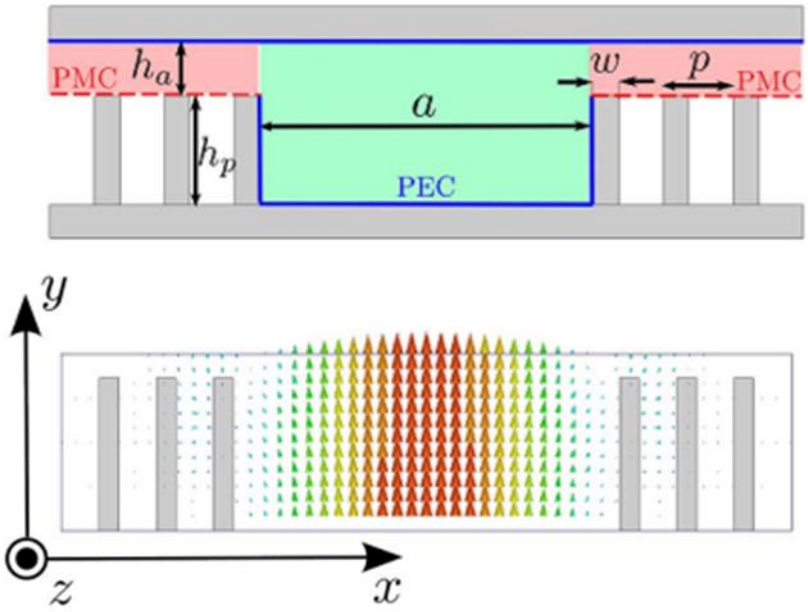

2-33 GGW cross-section and E-field distribution of its fundamental mode [128].

In [128], the stopband of the GGW structure in this case ranges form 28.1GHz to 52.9 GHz as demonstrated in Figure 2.34. Three frequencies were analyzed namely, 28GHz (outside the stopband, mode below cutoff), 29 GHz (inside the stopband, mode below cutoff), and 40GHz (inside the stopband, mode under usual operation above cutoff).

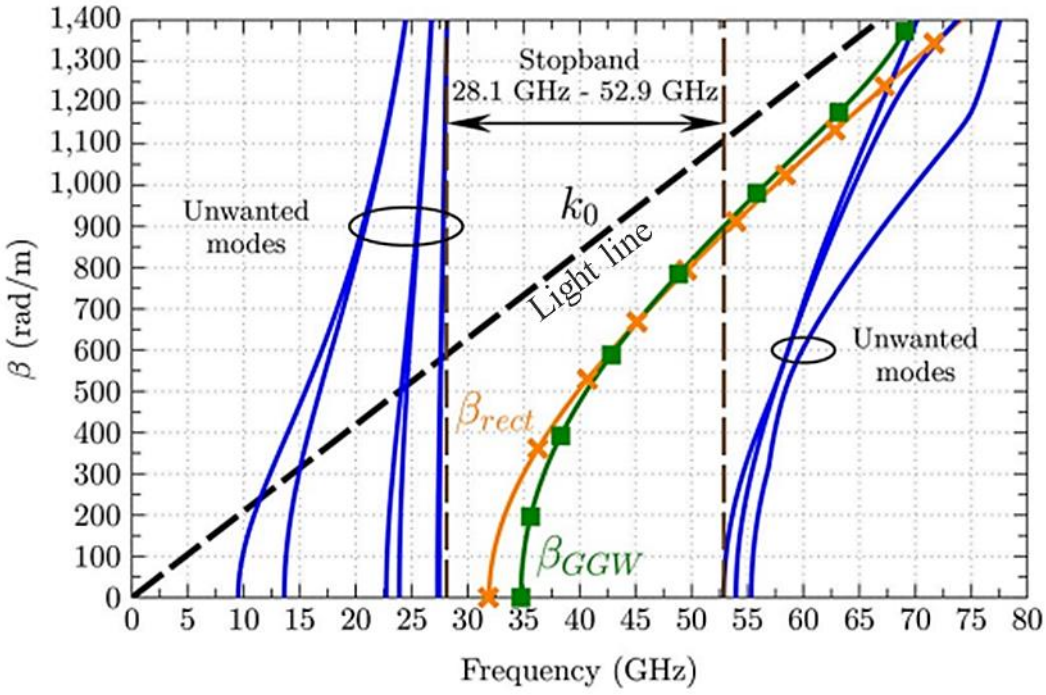

Figure 2-34 GGW line segment dispersion diagram.

The comparison of GGW and rectangular waveguide behavior, illustrated in Figure 2.35, reveals distinct electric field dynamics. Outside the stopband (at 28 GHz), the E-field spreads into the pin structure preventing any propagation of the signal.

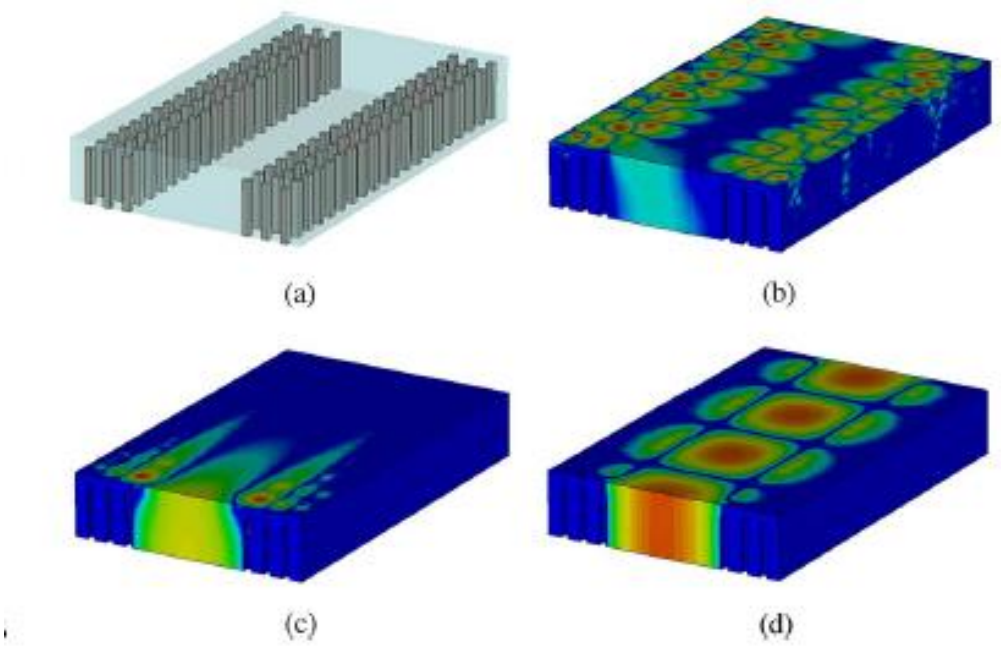

Figure 2-35 GGW analyses for 3 different frequencies (a) GGW structure. (b) 28GHz (c). 29Ghz. (d) 40GHz [128].

However, within the stopband, energy is delivered along the axial direction in a similar manner to the rectangular waveguide mode TE_{10}, regardless of whether the mode is below or above cutoff frequency. Notably, when the mode is below cutoff, the E-field spreads more in the lateral directions, indicating a significant change in energy distribution even though effective propagation along the axial direction is inhibited. A better illustration of the E-field distribution in fundamental mode was shown in Figure 3.36.

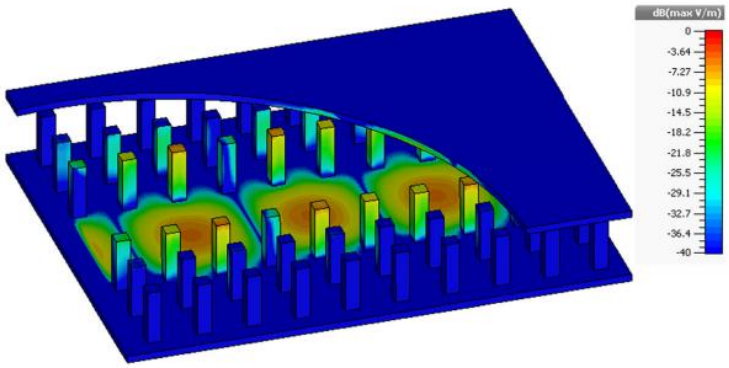

Figure 2-36 Front view of E-field distribution GGW [130].

Ideally, the lateral periodic structures should extend infinitely, whereas in practice, they can be significantly truncated without significant loss of performance. Studies have shown that even with just three rows of pins, the desired effect of forbidding propagation in the lateral regions can still be achieved effectively [129]. Therefore, while infinite extension is optimal in theory, practical implementations can utilize much smaller configurations with minimal compromise in performance

The main difference with the RGW is that the GGW allows propagation of TE/TM modes as a substitute of quasi-TEM mode in the RGW. Thus, the operation of GGW is similar to the rectangular waveguides along with an additional advantage of not requiring electrical contact between the top and lower conductor layer of the guiding structure [131] [132] [133].Besides, the GGW has fewer losses (higher Q factor) compared to the RGW since the ridge is removed from the bottom plate. Thus, more volume of the current density and more space for signal propagation compared to RGW. However, the resonant length of both guiding structures can be affected by the tolerance in the positioning of the pin walls, in contrast to the rectangular waveguide, which has a larger Q factor. Besides, the fact that the propagating ridge is not in the same level of the periodic nails offers a low insertion loss at high frequencies, which is very similar to that of conventional rectangular waveguide. In addition, the fabrication limits for the realization of compact parts have to be considered in the design of the structure. Specifically, in order to consider the cost and tolerance of the fabrication, a trade-off between the cross-section and length of the pins has to be taken into account.

In order to have more flexibility in the design, MRGW [134] were used instead. In this kind of waveguide, the integration into planar circuits is more effective than traditional waveguides, and the dielectric losses are not severe compared to the conduction losses. There is also some new modified version of GW, which will be explained in the following sections.

2.5.2.3 Inverted Microstrip Gap waveguide IMGW

The IMGW is a specialized structure designed for efficient signal propagation, particularly in the design of arbitrary circuits with bends and discontinuities where the unit cell's position must be adjusted to fit the overall structure while maintaining the performance. In order to prevent the ridge from disrupting the periodicity of PMC surface, the ridgeline is placed atop the bed of nails without direct connection to the ground plane, utilizing a thin low-dielectric constant substrate to ensure proper spacing. This method preserves the periodicity of the bed of nails or mushrooms.

Additionally, the air gap within the IMGW can be filled with low-dielectric constant materials to maintain the wideband characteristics of the guiding structure. A microstrip circuit featuring the necessary discontinuities can be printed on a grounded substrate and then flipped to face the periodic texture. In this arrangement, as shown in Figure 2.37, the AMC surface forces the E-field to propagate through the air gap between the microstrip line and the top metal, effectively allowing the IMGW structure to function as a packaged microstrip line, as highlighted in several publications [135] [136].

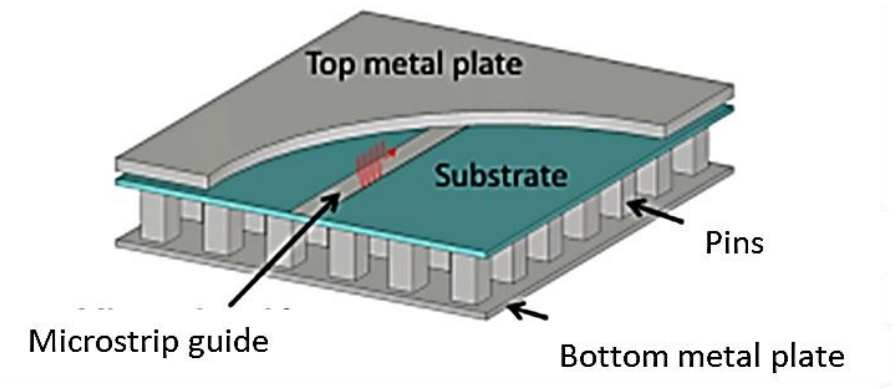

Figure 2-37 IMGW structure.

IMGWs are complex structures to analyze and design, but they have garnered substantial interest due to their unique combination of benefits. They merge the low-loss advantages of metallic waveguides with the compact size and ease of fabrication associated with microstrip technologies. As a result, IMGWs can be a preferred choice for feeding networks in certain applications. The IMGW is a very convenient technology for the design of low loss feed networks due to the dielectric low loss since there is no dielectric substrate in the propagation region between the microstrip and the upper PEC. Moreover, the conductive metal loss is reduced to a minimum by increasing the transverse dimensions of the microstrip lines, which can be done due to both surface waves and radiation, provided if the inverted micro strip line is packaged by gap waveguide technology.

In particular, it was found in [138] that there is a need for a compact wideband transition from IMGW to rectangular waveguides that enters orthogonally to the microstrip circuit, which is a severe limitation when designing IMGW antenna arrays at high frequencies.

The first step to realize in the design of the IMGW is the meta surface that generates the stop-band in the desired frequency band. To do so, the dispersion diagram generated by a unit-cell in the irreducible Brillouin zone is evaluated as depicted in Figure 2.38 (b). In this example, the generated stop band extends from 20.9 GHz to 35.7 GHz, which includes the desired center frequency of 28 GHz.

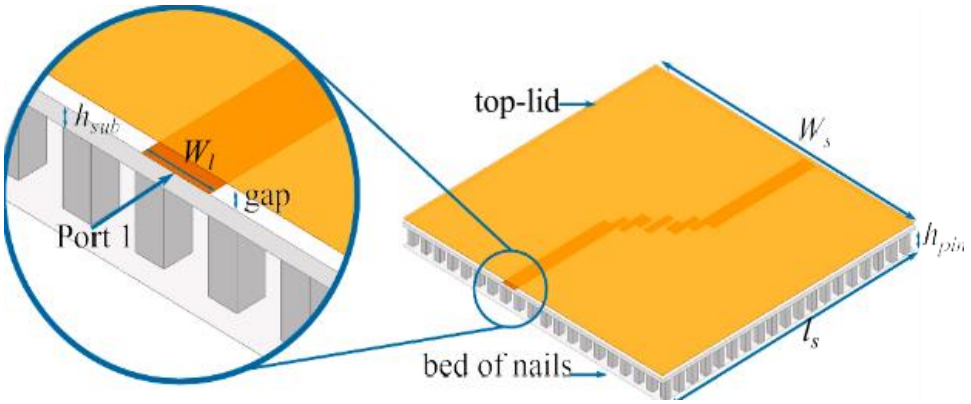

(a)

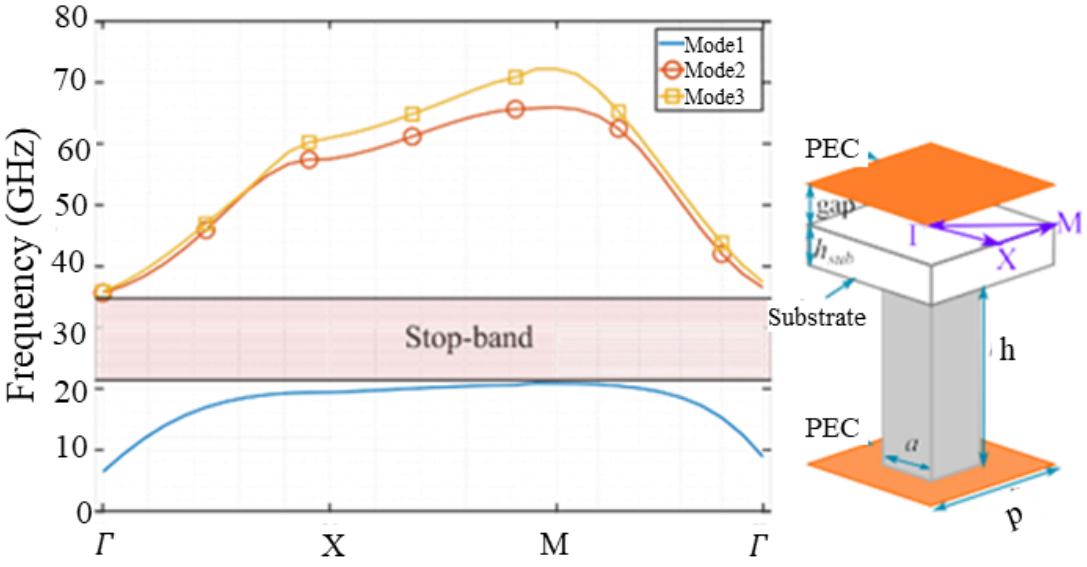

(b)

Figure 2-38 (a) IMGW topology, (b) Unit cell dispersion diagram [137].

The proposed unit cell is designed with periodicity p = 2.05 mm and consists of a conductive pin of lateral dimensions a = 0.8 mm and a height h_{pin} = 1.25 mm. On top of the conductive pin is placed a substrate with a relative permittivity ε_r = 3 and height h_{sub} = 0.5 mm. Over the substrate, separated by an air gap of 0.5 mm, is placed a PEC top plate. To have a parallel plate condition for the unit cell, a PEC plate is also placed at the bottom of the conductive pin. Once the meta surface structure is designed, a 50ohms microstrip line is added above the substrate over the conducting pins.

Table 2.2 summaries the potential losses for the different versions of GW and conventional transmission technologies at the 60GHz band at which we are most interested.

Table 2-2 Losses associated with GW structures.

Prototype	*Frequency range (GHz)*	*Simulated loss (dB/cm)*	*Measured min-max loss (dB/cm)*
GW	*50-75*	*0.0136*	*0.295 – 0.042*
GGW	*50-75*	*0.019*	*0.03 – 0.0442*
RGW	*50-75*	*0.0373*	*0.058 - 0.0705*
PRGW	*56/68*	*0.0805*	*0.162 - 0.23*
IMGW	*56-72*	*0.0934*	*0.21 - 0.288*
*MS line**	*50-75*	*0.23*	*0.62 – 0.77*
*MS line***	*50-75*	*0.271*	*0.7055*
SIW	*50*	*0.1327*	*0.2172*
Air-filled SIW	*50*	*0.0621*	*0.0615*

**LCP 0.127-0.2mm substrate; **Rogers 4003 0.127-0.2mm substrate*

Conclusion

In this chapter, detailed examination of both conventional and emerging wave guiding techniques was investigated, focusing on their advancements, advantages, and drawbacks. Conventional methods, such as hollow waveguides, were evaluated for their high power handling and precision, yet their limitations in size and cost persist despite technological improvements. Newer techniques, including SIW and RGW, offer significant enhancements in miniaturization, BW, and integration, although they introduce new challenges such as significant losses and complex fabrication processes. Overall, the chapter underscores the progress made in wave guiding technologies and highlights the balance between performance improvements and practical limitations, offering valuable insights for selecting suitable techniques for MMW applications.

CHAPTER III: DUAL BEAM DRA-BASED ARRAY FOR 5G APPLICATIONS

3.1 Introduction

Recently, researchers have increasingly turned their focus to the MMW band, as it offers a substantial amount of untapped spectrum that may satisfy the growing demand for high performance wireless data systems. The MMW band provides the capacity for significantly higher data rates and enhanced communication capabilities compared to lower frequency bands. However, adopting MMW frequencies presents several challenges. The high frequency signals in this band are more susceptible to impairments due to their shorter wavelength and increased sensitivity to atmospheric conditions, which can cause signal attenuation and degrade the overall performance. Additionally, as MMW antennas become smaller in size, the current flow density increases, leading to high conduction losses and reduced overall efficiency. Addressing these challenges is crucial for optimizing the performance and potential MMW technology in advanced wireless systems [139].

The DRAs offer a promising solution to this problematic; they are expected to be the best replacement for conventional electric radiating elements, particularly in high-frequency applications like MMW systems. Unlike conventional antennas that suffer from conduction losses due to the presence of metal components, DRAs use dielectric materials, which makes DRAs not only cost-effective but also capable of achieving high gain and high radiation efficiency as well [140]. When properly excited, DRAs present excellent performance characteristics, including improved signal strength and efficient energy radiation, making them a compelling choice for advanced communication systems.

Besides, adopting array technology will provide higher channel capacity and improve the system throughput compared to a single radiating element. Nevertheless, improving the channel capacity will not insure a sufficient operating BW to cover all users [141]. This difficulty was behind the idea of introducing the beam-forming technology, which focuses the signal into specified directions for better coverage and reliability. Several works related to this latter concept were introduced in the literature [142] [143] [144].

This chapter provides firstly, through a concise literature overview, a comprehensive understanding of DRAs and their evolving role in modern antenna systems. This review covers the foundational concepts and key developments in DRAs technology, including

their operational principles, types, and applications, highlighting their unique advantages and performance metrics. After that, a miniaturized bi-band triangular DRA-based array along with a dual-beam forming capability was investigated for the Ka-band applications. In fact, a miniaturization technique is achieved by cutting a rectangular DRA diagonally and applying a metallic strip at the top side wall. Therefore, the proposed configuration provides a dual-band and dual-beam abilities at the same time, with a wide beam pointing angle (>30°). The obtained results show that this novel design delivers high radiation efficiency and high gain at both operating frequencies with a large impedance BW.

3.2 DRA overview

The DRA principle relies on a dielectric resonator as the primary radiating element that can transform guided waves into unguided waves [140]. In the past, these antennas have been mainly realized by making use of ceramic materials characterized by high permittivity and high Q factor (between 20 and 2000) [145]. Currently, DRAs are made from several plastic materials with a high dielectric constant. The main advantages of DRAs are summarized as follows

- **Compact size:**

The size of a DRA is proportional to $\frac{\lambda_0}{\varepsilon_r}$ where $\lambda_0 = \frac{c}{f_0}$ is the free space wavelength at the resonant frequency f_0, and ε_r is the relative permittivity of the dielectric material. Unlike traditional metallic antennas, which are sized proportional to λ_0, DRAs can be much smaller when using materials with high dielectric constants, leading to more compact designs [146].

- **High radiation efficiency:**

DRAs, particularly when constructed from low-loss dielectric materials, exhibit high radiation efficiency. This latter is especially advantageous at very high frequencies (30 GHz to 300 GHz) [147], where conventional metallic antennas often suffer from increased conductor losses [148].

- **Wide BW:**

The impedance BW of a DRA can be significantly large if the dimensions of the dielectric resonator and the material's dielectric constant are appropriately selected, allowing for effective operation over a broad range of frequencies [149].

- **Versatile Excitation Techniques:**

DRAs can be excited through various methods, such as coaxial probes, micro-strip lines, or aperture coupling. This versatility facilitates their integration into different applications and array configurations [150].

- **Customizable Performance:**

The gain, BW, and polarization characteristics of DRAs can be easily tailored using different design techniques, allowing for precise control over their performance, which helps to meet different application requirements [151].

3.3 DRA characteristics

The characteristics of DRA are mainly determined by the following criteria:

3.3.1 Components and structure

The shape, size and type of dielectric material play a significant role in the design of DRA. The core of the DRA is usually made from materials with high dielectric constant ε_r that helps concentrating the EM energy efficiently, such as ceramics, glass, or certain polymers [152]. These resonators are readily available in simple geometries such as cylindrical, rectangular, or spherical shape as illustrated in Figure 3.1, to suit several types of wireless applications, and different dimensions that can be tailored to resonate at particular frequencies.

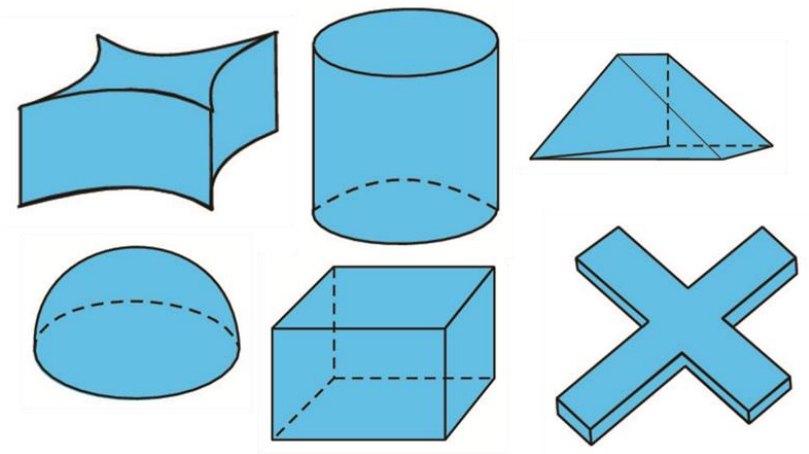

Figure 3-1 Different available shapes of DRA antenna.

Conventionally, in the design on DRA a ground plane is placed underneath the dielectric resonator to reflect the EM waves and enhance the radiation efficiency and directivity.

3.3.2 Resonance frequency

The DRA resonance frequency f_r is that at which the dielectric resonator naturally oscillates and radiates the stored EM energy most efficiently. This frequency is influenced by several factors; it is fundamental to its performance, affecting impedance matching, radiation characteristics, size, and overall efficiency [153]. Precise control and optimization of the resonance frequency are essential for designing effective and reliable antennas for various applications [154].

3.3.3 Relative permittivity

The choice of dielectric constant ε_r is crucial in the design of DRA with desired frequency characteristics; it indicates the energy storing capacity of the material when an electric potential is applied to it, and controls the EM wave's propagation through the material. It has direct influence on the size, BW, Q factor, and resonant frequency f_r of the DRA. The relative permittivity depends directly on the used material [150]. Higher ε_r implies that the material can store more electrical energy, which leads to a slower wave propagation speed, resulting in a lower resonant frequency for a given resonator size.

3.3.4 Quality factor (Q)

The Q factor of DRA measures the power loss and specifies the frequency selectivity of the operating system. It describes how well the antenna can store energy relatively to the energy lost per unit cycle and is defined as follows

$$Q = \frac{2\omega W_e}{P_{rad}} \qquad 3.1$$

Where W_e and P_{rad} are the stored energy and radiated power, respectively.

A high Q factor indicates a narrow BW and low energy loss, meaning the DRA has high efficiency and is well-suited for applications requiring precise frequency selection [155]. Whereas, low Q factor signifies a wider BW and higher energy losses, which might be desirable for applications needing broader frequency coverage.

3.3.5 Impedance BW

The impedance BW describes the range of frequencies over which the DRA can properly radiate or receive energy [156]. Generally, the desired BW is defined in terms of Voltage Standing Wave Ratio ($VSWR$) and Q factor

$$BW = \frac{VSWR-1}{Q\sqrt{VSWR}} \quad 3.2$$

Where $VSWR$ can be defined in terms of reflection coefficient $|\Gamma|$

$$VSWR = \frac{1+|\Gamma|}{1-|\Gamma|} \quad 3.3$$

The reflection coefficient is also referred to as S_{11} or return loss of the antenna [157].

3.3.6 Radiation efficiency

Several techniques exist for estimating the radiation efficiency η of antennas. For small antennas, the Wheeler cap method is particularly useful [158]. This method relies on the antenna's *Q*-factor that is based on the total power P given by

$$P = P_{rad} + P_{dis} \quad 3.4$$

where P_{rad} is the radiated power and P_{dis} is the power dissipated as heat.

It also linked directly to the radiation and loss resistance. By selecting the proper dielectric material with low-loss characteristics, high radiation efficiency can be maintained, even at MMW frequencies, due to the absence of surface waves and minimal conductor losses associated with the DRA.

The Q factor of the antenna can be separated into the radiation *Q* factor "Q_{rad}" and the dissipation *Q* factor "Q_{dis}" such that

$$\frac{1}{Q} = \frac{1}{Q_{rad}} + \frac{1}{Q_{dis}} \quad 3.5$$

The radiation efficiency η of the antenna is the ratio of the radiated power to the total power, expressed in terms of the antennas *Q* factors [140] as

$$\eta = \frac{P_{rad}}{P_{rad}+P_{dis}} = 1 - \frac{1}{Q_{dis}} \quad 3.6$$

In order to determine Q and Q_{dis}, experimental measurements of the return loss are taken with and without a radiation shield, or Wheeler's cap. Without the shield, the measured BW represents Q, while with the shield, which suppresses radiation, the measured BW corresponds to Q_{dis} [159]. Figure 3.2 illustrates a DRA covered by a Wheeler's cap.

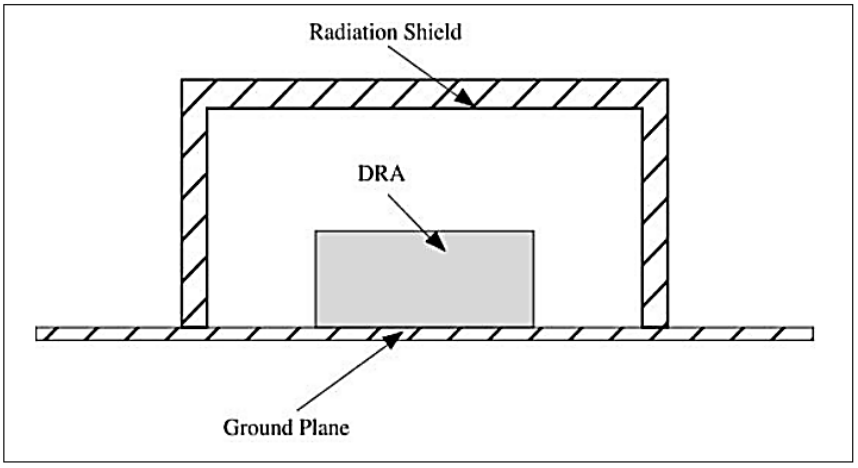

Figure 3-2 Wheeler cap method for determining radiation efficiency.

The radiation efficiency of the antenna is also related to directivity (D) and gain (G) of the antenna by the following relation

$$\eta = \frac{G}{D} \quad 3.7$$

3.3.7 Radiation pattern

The radiation pattern depicted in Figure 3.3 consists of the graphical representation of the radiation far field properties of the DRA, which is described as the angular variation of the radiation level around the antenna [160]. It is studied in the form of radiated power field patterns as a function of the direction in the far field region to provide insight about the directionality and coverage of the DRA's, which is crucial for understanding its performance in various applications. Several factors can affect the shape and direction of the radiation pattern:

- Specific resonant modes (such as TE or TM) exhibit different field distributions, influencing how energy is radiated.

- The type of feeding mechanism affects the symmetry and directivity of the radiation pattern.
- The dielectric properties of the material can disturb the radiation pattern by influencing the effective permittivity and the manner the DRA interacts with EM waves.

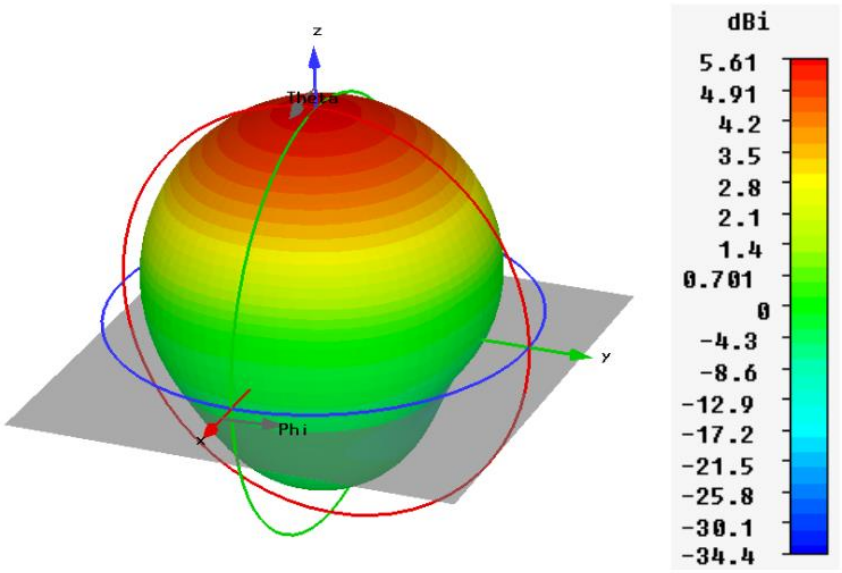

Figure 3-3 3D radiation pattern for a typical DRA.

The physical dimensions and shape of the DRA determine the main lobe's direction and the overall beam width. Larger DRAs or those with different aspect ratios exhibit distinct radiation characteristics [161]. Typically, rectangular DRA exhibit a radiation pattern with a pronounced main lobe in the direction normal to the largest face. Whereas, cylindrical DRAs, usually provide more symmetric radiation pattern around their axis. This means that the radiation is relatively uniform in the plane of the cylinder but it might show varying patterns along the axis. Hemispherical DRA is often used in applications requiring wide coverage such as in satellite communications. The radiation pattern is typically wide and provides good coverage over a hemisphere [162].

3.4 Rectangular DRA

The rectangular DRA is the most common shape in the literature since it is characterized by three independent dimensions a, d and b designating width, length and height, respectively. Thus, offering one degree of freedom more than the cylindrical DRA and great design flexibility, due to the large choice of both dielectric materials and different lengths ratios.

Usually the dielectric waveguide model is used to analyze the rectangular DRA [163].

In this type of DRA, the top surface and two among DRA sidewalls are assumed to be perfect magnetic walls, whereas the two others are imperfect magnetic walls.

Figures 3.4 (a) and (b) show 3D and cross-sectional views of a rectangular DRA fed by a slot aperture, respectively. The DRA is mounted on a ground plane so that, an electric wall is assumed for the bottom surface.

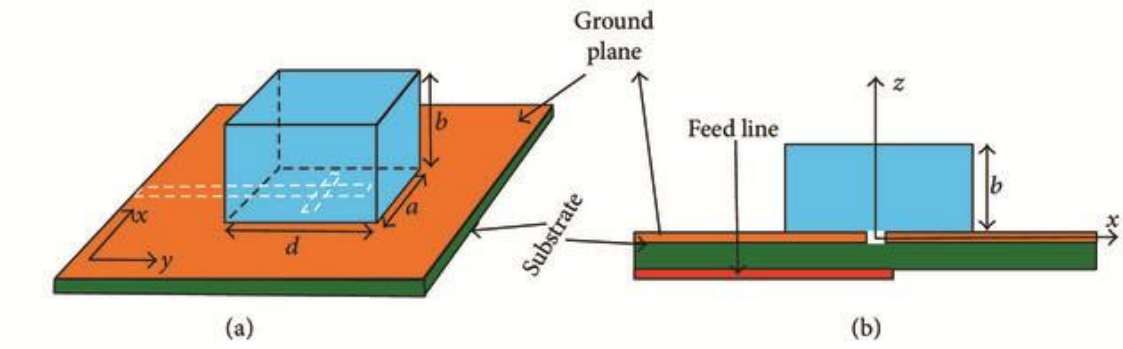

Figure 3-4 Aperture-fed rectangular DRA. (a) 3D view. (b) Cross-sectional view.

The modes of an isolated rectangular DRA can be classified into two main categories: TE and TM modes. However, when the DRA is mounted on a ground plane, it typically excites only TE modes. Since the DRA's three dimensions are independent, TE modes can be existed along the x, y, and z axes with TE_{111} as the fundamental mode. Referring to the Cartesian coordinate system shown in Figure 3.5 , if the dimensions of the DRA satisfy $a > b > d$ then the modes are arranged in order of increasing resonant frequency as TE_{z111}, TE_{y111}, and TE_{x111}.

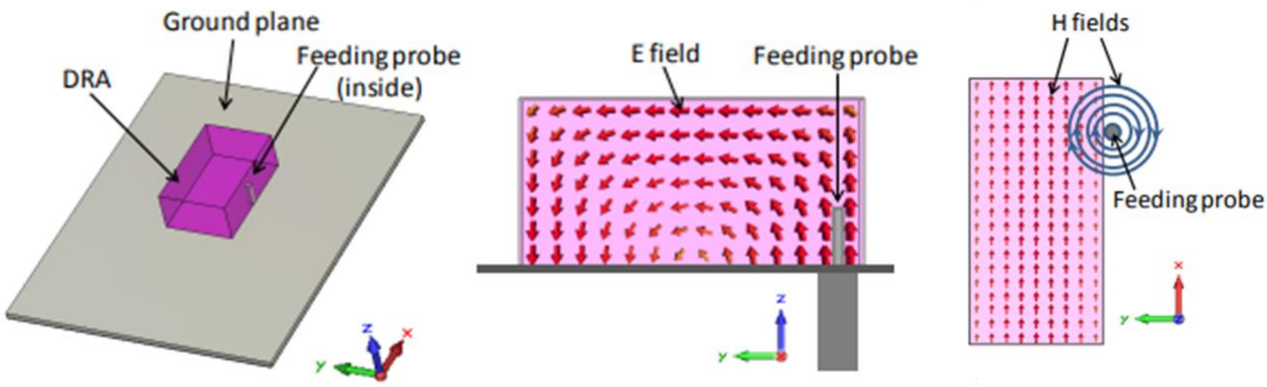

Figure 3-5 E-field and H-field distribution in probe fed DRA.

Each mode can be analyzed similarly, with detailed analysis of the TEz111 mode provided in [164], which includes analytical descriptions of the E-field components within the resonator and the corresponding resonant frequencies

In order to analyze the rectangular DRA, the dielectric waveguide model [163] is employed. When the DRA is positioned on a ground plane, TE modes are excited, and the resonant frequency of the fundamental mode, TE_{111}, is determined by means of the following equations [165], [166]

$$f_{111} = \frac{c}{2\pi}\sqrt{\frac{1}{a^2}+\frac{1}{b^2}+\frac{1}{c^2}} \times \frac{1}{\sqrt{\varepsilon_r}} \quad 3.8$$

Where:

a, b, and c are the physical dimensions of the rectangular DRA.

c is the speed of light in vacuum.

This equation is derived based on the standing wave conditions within the rectangular resonator. The term $\frac{1}{\sqrt{\varepsilon_r}}$ accounts for the fact that the speed of light is slower in the dielectric material compared to a vacuum.

Initially, the resonance frequency is determined by the wave equation that governs the propagation of EM waves inside the DRA. For a wave propagating inside a dielectric medium, the wave number *k* is related to the permittivity of the material and the frequency by:

$$f = \frac{c}{2\pi}.k.\frac{1}{\sqrt{\varepsilon_r}} \quad 3.9$$

For a dielectric rectangular DRA with dimensions a, b, and c in the x, y, and z directions, the wave number components in each direction (k_x, k_y, k_z) can be written as:

$$k_x = \frac{m\pi}{a}, \quad k_y = \frac{n\pi}{b}, \quad k_z = \frac{p\pi}{c} \quad 3.10$$

By substituting the mode indices $m = n = p = 1$ in x, y and z direction respectively from the TE_{111} mode, the wave numbers components become:

$$k_x = \frac{\pi}{a}\ , \ k_y = \frac{\pi}{b}\ , \ k_z = \frac{\pi}{c} \quad 3.11$$

And since he total wave number k can be expressed in terms of to the wave number components along each direction as:

$$k = \sqrt{k_x^2 + k_y^2 + k_z^2}, \tag{3.12}$$

then,

$$k = \sqrt{\left(\frac{\pi}{a}\right)^2 + \left(\frac{\pi}{b}\right)^2 + \left(\frac{\pi}{c}\right)^2} = \pi\sqrt{\frac{1}{a^2} + \frac{1}{b^2} + \frac{1}{c^2}} \tag{3.13}$$

By substituting equation 3.13 in equation 3.9 we arrive to equation 3.8.

The main advantage of the rectangular DRA relies on its three independent geometric dimensions a, b, and c, which provides greater design flexibility compared to the cylindrical and other DRA shapes. Additionally, the rectangular DRA exhibits lower cross-polarization levels than its cylindrical counterpart [166]. Besides, rectangular DRAs support multiple operational modes and typically present less complexity in impedance matching, making them versatile and effective for various applications.

3.4.1 Feed Mechanisms

The antenna requires a feed mechanism to excite the DRA modes properly. This can be accomplished through various methods such as a coaxial probe, a microstrip line, or an aperture-coupled feed.

3.4.1.1 Probe-Fed DRA

The probe-fed DRA is one of the earliest configurations documented in the literature [167] [168]. In this setup, the DRA is positioned directly on the ground plane and is excited through the substrate by a coaxial feed. The coaxial probe may either penetrate the DRA or be placed adjacent to it as illustrated in Figures 3.6.

By optimizing the length and positioning of the feeding probe, the amount of coupling and the input impedance of the DRA can be adjusted [169], thereby allowing control over the resonance frequency. Besides, depending on the location of the probe, various modes can be excited.

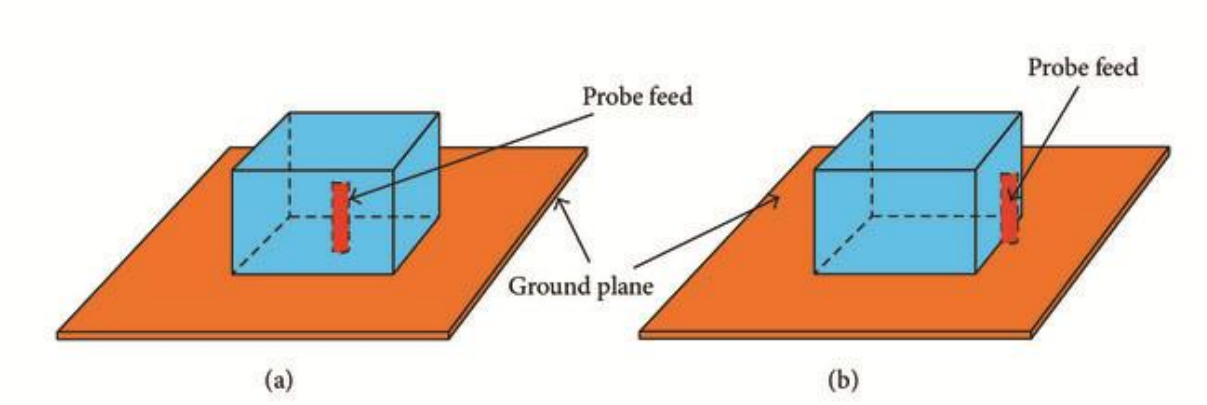

Figure 3-6 Probe-fed rectangular DRA (a) central feed, (b) adjacent feed.

A significant advantage of using a probe that penetrates the DRA is its high coupling efficiency to the resonator, where it can couple directly into a 50Ω system without the need for matching network, which eventually, leads to improved radiation efficiency and better performance. However, this configuration requires drilling a hole in the DRA, and the dimensions of the hole must match the probe's length and radius precisely. If not, the effective dielectric constant of the resonator will be altered, causing a shift in the antenna's resonance frequency [170]. Additionally, the drilling process complicates the manufacturing one and increases the fabrication cost. To reduce manufacturing complexity, an excitation probe can be placed adjacent to the DRA (see Figure 3.6(b)). This method is more cost-effective but results in lower coupling to the DRA, which can negatively impact the radiation characteristics of the antenna. For high-frequency applications, where the antenna is often integrated directly on a PCB or on-chip, probe-fed DRAs are typically impractical.

3.4.1.2 Microstrip transmission line-fed DRA

Another method for feeding the DRA involves proximity coupling from printed microstrip transmission lines. Figures 3.7 (a) and (b) provides a 3D view of a rectangular DRA fed by a conventional microstrip line and a conformal transmission line, respectively.

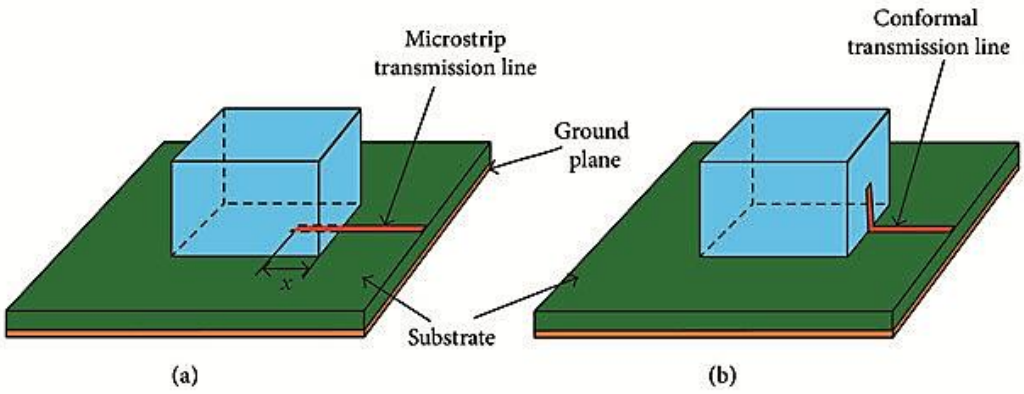

Figure 3-7 3D microstrip transmission line view. (a) Conventional case. (b) Conformal case.

This type of coupling will excite the magnetic fields in the DRA, producing a short horizontal magnetic dipole mode. The level of coupling can be tailored by adjusting the lateral position of the DRA with respect to the microstrip line and on the relative permittivity $\varepsilon_r$of the DRA. In traditional microstrip line-fed DRAs, the dielectric resonator is positioned directly on the transmission line printed on the PCB substrate. One of the earliest documented DRAs with microstrip line feeding is described in [171]. This study has demonstrated that the overlap distance (x) influences the coupling strength and the mode excited by the transmission line, and the optimal coupling occurs when x is slightly less than $\lambda/4$ of the dielectric wavelength at the resonance frequency.

A significant drawback of the microstrip transmission line feed is that the feeding line is not isolated from the dielectric resonator, which affects potentially the DRA's radiation performance. Additionally, placing the dielectric resonator directly on the transmission line can create an undesired air gap between the resonator and the PCB substrate. Moreover, for wide band applications a low permittivity DRA is required, except that low permittivity values are directly associated with small amount of coupling. Thus, an array of DRAs is required in order to achieve an acceptable radiation efficiency. In this case, microstrip lines can be used as a series feed for a linear array of DRAs if a sufficient number of elements are used. One disadvantage of this method is that the polarization of the array is dictated by the orientation of the microstrip line because the direction of the magnetic fields in the DRA is parallel to it.

In a conformal transmission line-fed DRA the resonator is positioned directly on the PCB substrate, and the feeding microstrip line is bent over the resonator, as depicted in Figure 3.7(b). This arrangement integrates the transmission line with the resonator without introducing an air gap. The shape of the transmission line, which conforms to the contour of the dielectric resonator, can be optimized to enhance the DRA's performance. For instance, [172] proposes using a conformal elliptical patch to feed a U-shaped DRA, to achieve an impedance BW of 72%.

3.4.1.3 Coplanar waveguide-fed DRA

The CPW excitation method was first introduced in [173] , where a symmetrical CPW circular-loop network was used to feed a rectangular DRA as depicted in Figure 3.8. The coupling level can be adjusted by altering the position of the DRA over the loop. The coupling behavior of the co-planar loop is similar to that of the coaxial probe, but the loop offers the advantage of being non-obtrusive.

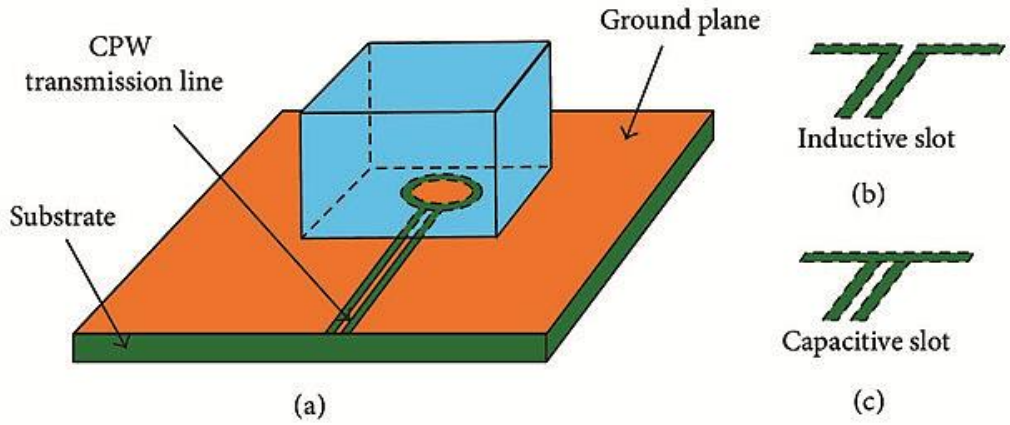

Figure 3-8 (a) Rectangular DRA fed by a CPW circular-loop network. (b) Inductive slot feed. (c) Capacitive slot feed.

One key advantage of CPW excitation is the ability to adjust the coupling slot beneath the dielectric resonator to optimize DRA performance. In [174] the circular-loop feeding network was replaced with an inductive slot and a capacitive slot in conjunction with a hemispherical DRA. It was found that the capacitive slot introduces an additional resonance, resulting in dual-band behavior with resonances associated with both the DRA and the feeding slot. CPW feeding structures are particularly popular in MMW applications and are especially effective

when the DRA is integrated into a System on Chip (SoC). This approach enhances antenna efficiency by using CPW transmission lines, which keeps the dielectric resonator separated from the lossy silicon substrate by the ground plane.

3.4.1.4 Slot-Fed DRA

One of the most widely used feeding techniques for DRA is the aperture coupling via a slot cut in the ground plane that is fed by a micro strip line beneath the ground plane. In this method, the aperture behaves like a magnetic current running parallel to the length of the slot, which excites the magnetic fields in the DRA [175]. The guided wave traveling along the transmission line is coupled through the slot to excite the resonant modes of the DRA. This coupling mechanism has the advantage of having the feed network located below the ground plane, thus avoiding spurious radiation. The microstrip stub can be designed to cancel out the reactive component of the slot, thus allowing for an impedance match to the DRA. Figure 3.9 illustrates the top view of an aperture-coupled hemispherical DRA, as described in [176].

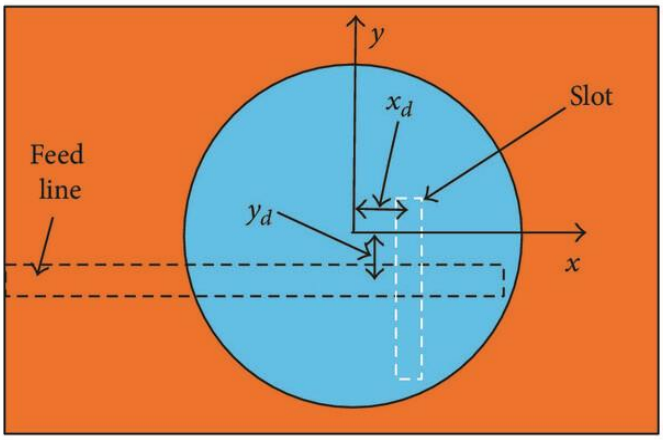

Figure 3-9 Slot-fed hemispherical DRA.

This study explores the impact of slot displacements $x_d$and y_d from the center of the DRA. It was observed that the coupling level could be adjusted by moving the DRA with respect to the slot allowing for a large degree of design flexibility. In this example the optimal resonance and impedance matching occur when the DRA is precisely centered over the slot at "$x_d = y_d = 0$". This technique's main advantage is that it prevents direct EM interaction between the feed line and the DRA. This separation helps reduce spurious radiation from the feeding network, thereby improving the polarization purity of the DRA. However, a significant challenge with this method is that the slot length needs to be approximately $\frac{\lambda}{2}$, which can be difficult to achieve at lower frequencies while maintaining a compact DRA size.

3.4.2 DRA miniaturization methods

To minimize the size of a DRA, two prevalent approaches are employed, namely using materials with high dielectric constants and inserting a metal plate in the symmetry plane of the resonator.

3.4.2.1 High relative dielectric constant

The size of a DRA is generally inversely proportional to the dielectric constant ε_r of the resonator, so in order to reduce the DRA's size we can select a material with a high dielectric constant. However, this choice must be made with caution as a higher dielectric constant can negatively impact the impedance BW. For instance, in the work of [166] a low-profile rectangular DRA ($0.026\lambda_0$) is made from a material with a very high relative permittivity ($\varepsilon_r = 100$); but even with such a high dielectric constant, the impedance BW remains reasonable, ranging from 1.1% to 3.3%.

To address BW limitations associated with high dielectric constants, a multilayer DRA design can be employed. By optimizing the dielectric constant and height of each layer, the DRA's parameters, such as size, impedance BW, and gain, can be finely tuned. Figure 3.10 depicts the cross-sectional view of a two-layer rectangular DRA as proposed in [177] where ε_{r1}, ε_{r2}, h_1 , h_2 are the dielectric constant and hight of first and second layer, respectively .This multilayer configuration provides additional design flexibility for ε_{r2} and h_2 compared to a single-layer design. Using this approach, the authors in [178] successfully designed a low-profile rectangular DRA with a height of $\frac{1}{10\lambda_0}$ that achieved an impedance BW of 40% and an average gain of 9 dBi.

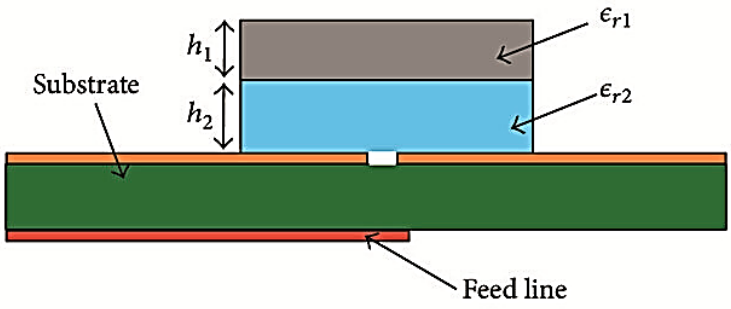

Figure 3-10 Cross-sectional view of a two-layer rectangular DRA for size reduction.

3.4.2.2 Metal plate along symmetry plane

Another effective technique for reducing the size of the DRA involves integrating a metal plate along the key symmetry planes, as suggested by image theory [179]. Figure 3.11(a) illustrates the cross-sectional view of a probe-fed rectangular DRA of length a, and height b, while Figure 3.11(b) shows its miniaturized counterpart.

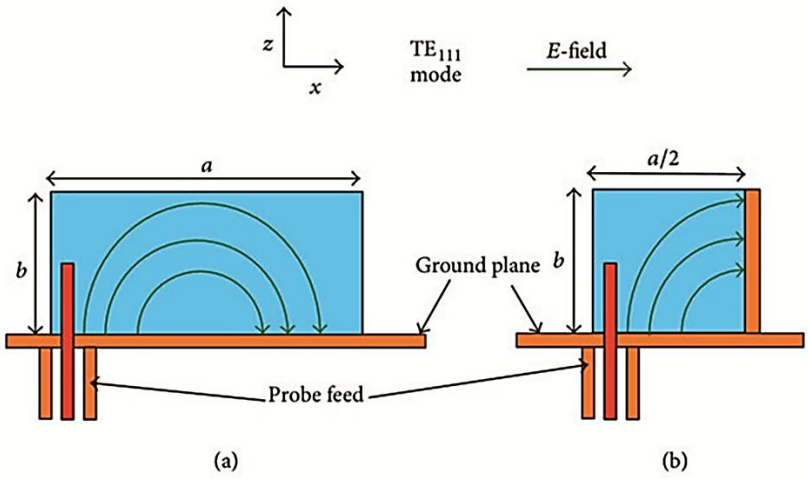

Figure 3-11 Probe-fed rectangular DRA. (a) Cross-sectional view (b) Miniaturized version.

As indicated in Figure 3-11, the size of the DRA can be halved by placing a conducting plate along the central cross-section of the dielectric resonator at $x = a/2$. The effect of the miniaturization on the resonant frequency and the impedance BW of a DRA was investigated in [180] and the results are summarized in Table 3.1.

Table 3-1 Effect of miniaturization of rectangular DRA

Parameters	***Before miniaturization***	***After miniaturization***
$\boldsymbol{a}\ (\boldsymbol{mm})$	*88*	*44*
$\boldsymbol{b}\ (\boldsymbol{mm})$	*40*	*40*
$\boldsymbol{Volume}\ (\boldsymbol{cm^3})$	*70.4*	*35.2*
$\boldsymbol{\varepsilon_r}$	*12*	*12*
$\boldsymbol{f_0}\ (\boldsymbol{GHz})$	*1.22*	*0.918*
Impedance BW (%)	*16*	*5.4*
Conducting plate	*No*	*Yes*

It is clearly seen that the insertion of the metal plate allows halving the volume of the DRA but at the same time, results in a reduction of the available impedance BW by a factor of three. It should be mentioned that when a conducting plate is used, the position as well as the length of the feeding probe should be fine-tuned in order to match the input impedance of the antenna at the desired resonant frequency.

3.5 Design of miniaturized DRA

Due to the importance of the permittivity of the dielectric material in the selection of the proper substrate for the DRA, we focused in part this of the work on investigating the variation in the permittivity of the substrates against the S_{11} response. The implementation results of this examination were subsequently used to obtain the best behavior for the proposed antenna at the targeted double band range.

As indicated in Figure 3.12, five substrates with different levels of permittivity were used in this study to analyze the double band frequency response, including (Rogers RT5880 with ε_r = 2.2), (Rogers RO3003 with ε_r = 3), (Rogers RT6006 with ε_r = 6.45), (Rogers RT6010LM with ε_r = 10.7), (Rogers RO 3010 with ε_r = 11.2).

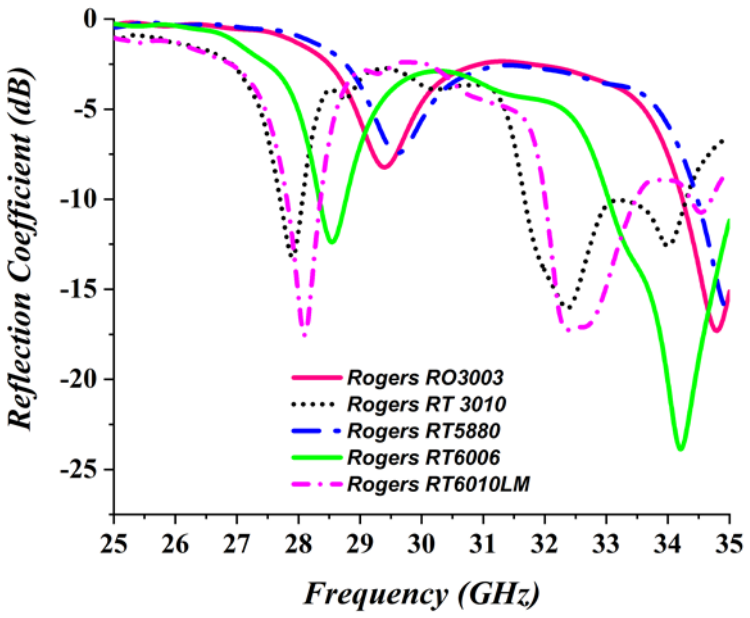

Figure 3-12 Return loss of different substrate dielectric constants.

It appeared that when the proposed DRA was built over the Rogers RT5880 (εr = 2.2) and Rogers RT 3003 (εr = 3), it exhibited only a single resonant frequency around 35 GHz, which does not meet the double band target defined within this work. In contrast, when the

Roger RT 6006 (εr = 6.45) was utilized, the antenna successfully achieved the required double band behavior at 29 and 39 GHz but the reflection coefficient was not consistent between these two frequencies. However, with higher relative permittivities, Rogers RT6010LM (ε_r = 10.7) and Rogers RO3010 (ε_r = 11.2), both exhibited nearly identical dual-band behavior, resonating at approximately 28 GHz and 33 GHz.

Accordingly, the array's DRAs were constructed using Rogers RT6010LM laminate with relative permittivity of ε_r =10.6 and a loss tangent of δ=0.0023. This material was chosen due to its superior dual-band performance, since it demonstrates the most distinct double band behavior. Finally, The DRAs are mounted on a Rogers RO3003 substrate with dielectric constant of ε_r=3, a loss tangent of δ=0.001 and a thickness of 0.75mm. All dimensions of the proposed antenna, as depicted in Figure 3.13, are listed in Table 3.2.

Table 3-2 Optimum dimensions of the proposed array antenna.

Parameters	***Values (mm)***
W	**15**
L	**20**
W_l	**0.2**
L_l	**5.54**
a	**2.5**
b	**6**
c	**5**
a_1	**2**
a_2	**1.33**
a_3	**1.5**
a_4	**2.1**
a_5	**0.94**

The structure is excited by a thin microstrip feed line mounted on the bottom side and the spacing between the two adjacent radiating elements has been carefully optimized to avoid a severe interference between the two main side lobe beams.

In order to achieve reduced size shapes and avoid designing a bulky structure, a miniaturization technique described in [181] was employed; in this case, the Rectangular DRA (RDRA) is divided diagonally to obtain a Triangular DRA (TDRA) that is further covered by a thin sheet of copper from the upper face as shown in the design layout of Figure 3-13 (a). The detailed configuration views of the proposed array antenna is illustrated in Figures 3.13 (b) and (c).

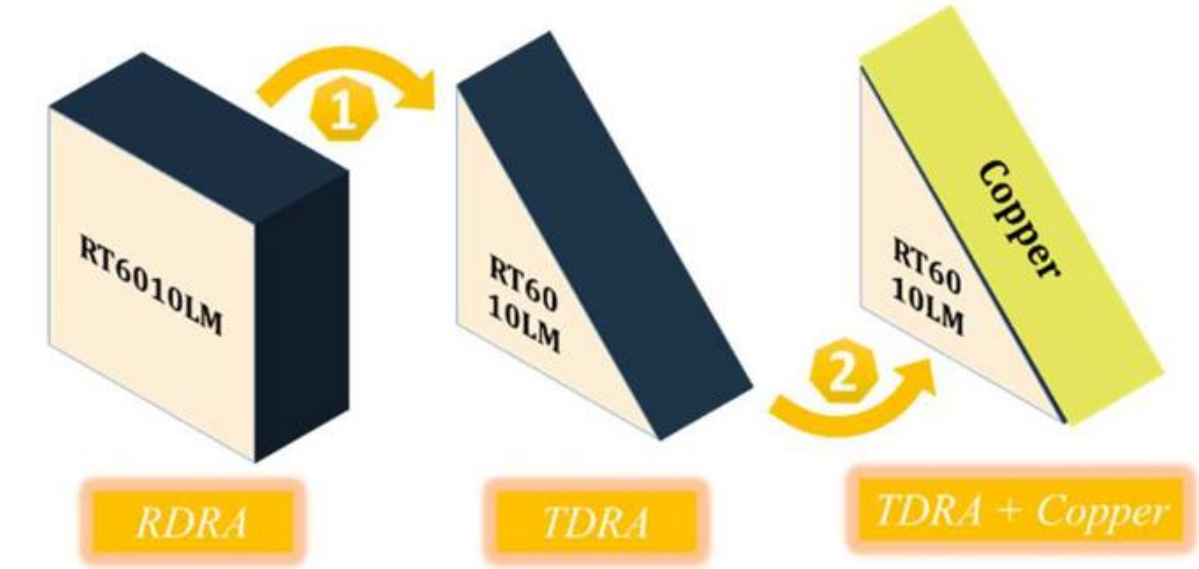

(a)

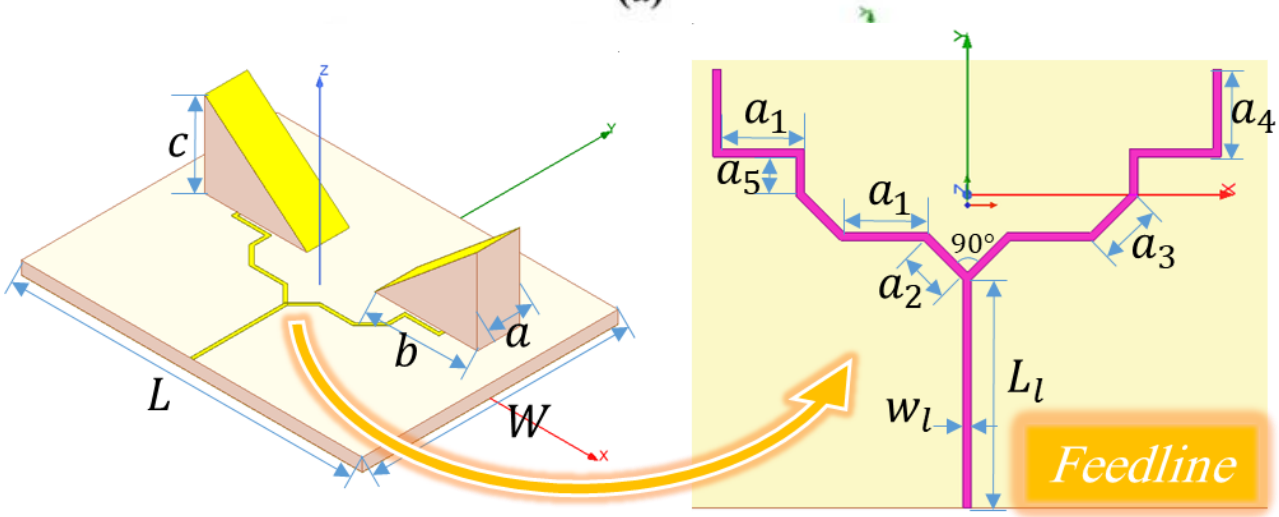

(b)

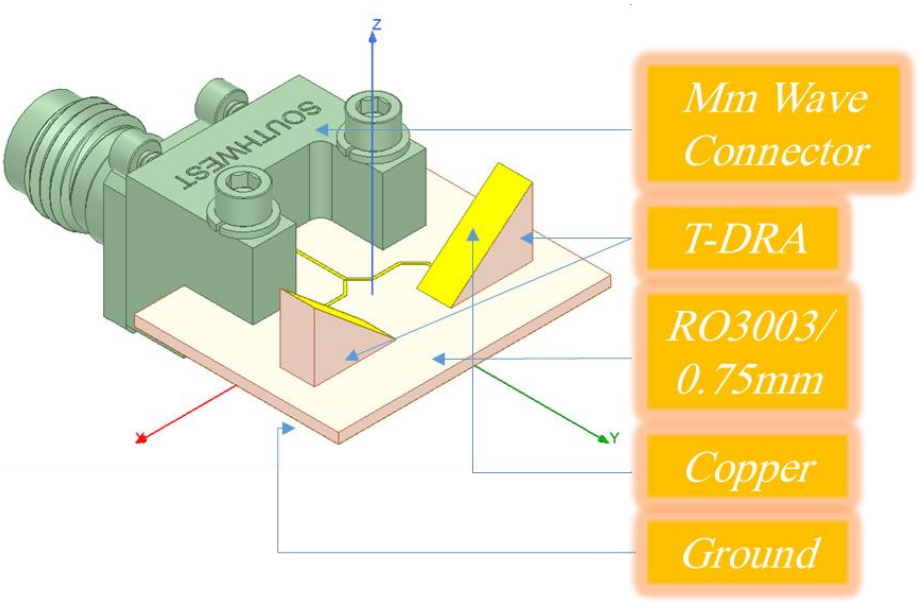

(c)

Figure 3-13(a) Miniaturization process (b-c) Sketch of the proposed antenna.

By cutting the RDRA diagonally and plating it with copper cladding (assuming the copper acts as a PEC), we introduce a discontinuity that will alter the distribution of EM fields within the dielectric resonator. This modification causes the EM fields to concentrate differently within the dielectric material, because certain modes that previously exhibited symmetric field distributions are disrupted or redistributed and the symmetry breaking caused by the diagonal cut and the PEC boundary conditions can excite some new modes and couple energy to the radiating aperture (formed by the copper cover). In summary, this modification leads to a radiation pattern with a tilt angle as opposed to the typical broadside pattern associated with symmetric RDRAs, providing directional radiation suitable for specific applications requiring beam steering or focused radiation patterns. In this case, the tilt angle of the beam depends on the dimensions and orientation of the diagonal cut and the copper cover.

3.5 Results discussion

As illustrated in Figure 3.14, the metallized TDRA has demonstrated a distinct double band performance with a return loss of less than -10 dB and VSWR~1 at around 28 GHz and 33 GHz. At 28 GHz, the antenna maintains a large impedance BW greater than 1 GHz, ranging from 27.96 GHz to 28.7 GHz and ensuring effective operation within this band. Similarly, at 33 GHz, it exhibits an impedance BW extending from 32.4 GHz to 33.5 GHz, which also

covers more than 1 GHz. These results indicate excellent impedance matching and minimal signal reflection with dual-band behavior, confirming the TDRA's capability to deliver reliable performance across these critical MMW frequencies, with good VSWR close to 1 at both bands.

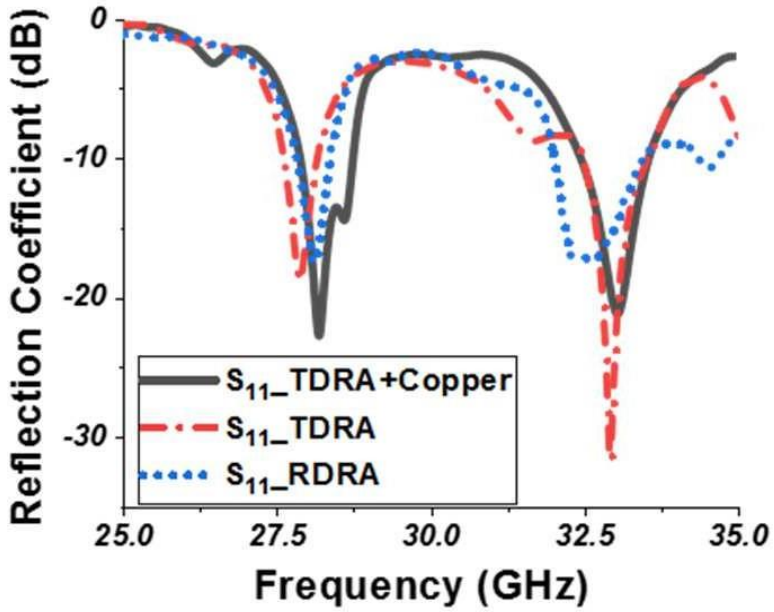

(a)

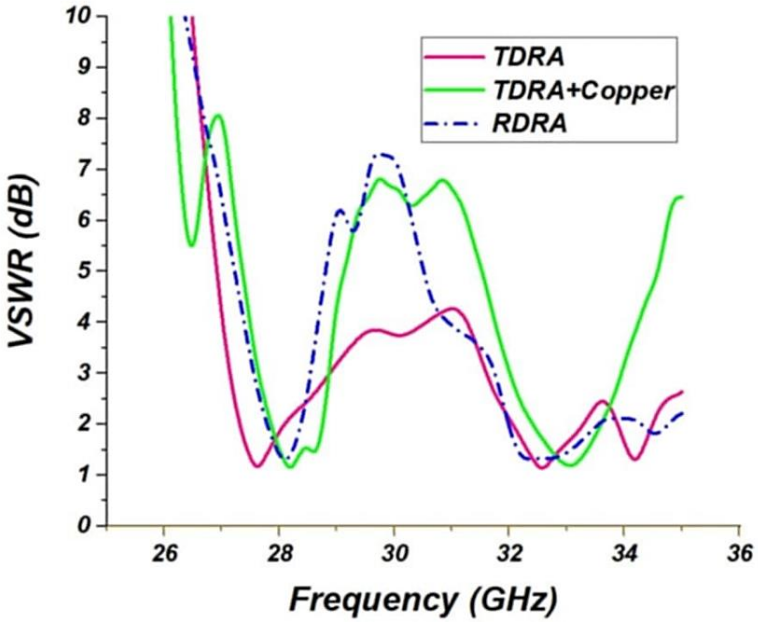

(b)

Figure 3-14. Proposed miniaturized dual-band TDRA characteristics. (a) Magnitude of reflection coefficient (S11). (b)VSWR.

As shown in Figure 3.15, the miniaturized TDRA presents impressive performance at both frequencies, achieving a peak gain of 8 dBi at 28 GHz and 6 dBi at 33 GHz. This antenna design maintains a remarkably stable radiation efficiency of approximately 90% across these frequencies, highlighting its effectiveness in delivering high gain while preserving excellent radiation performance.

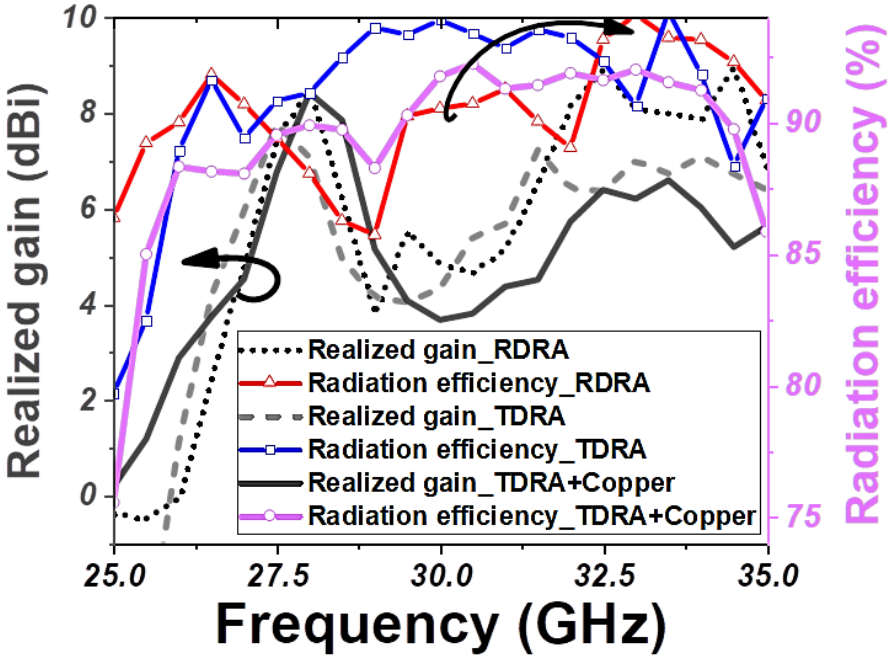

Figure 3-15 Realized gain and radiation of RDRA, TDRA, and TDRA+copper.

A comparison study of the results before and after miniaturization related to RDRA, TDRA, and TDRA+Copper cases reveals that, despite minor discrepancies in the graphical data, the performance metrics remain nearly identical across all configurations. This observation indicates that, the miniaturized TDRA maintains comparable performance characteristics to the original RDRA, even with its significantly reduced size. By employing a diagonal division method to shrink the RDRA's dimensions, the miniaturized TDRA has effectively reduced its physical dimensions without sacrificing efficiency or gain, making it well-suited for compact MMW frequency communication systems.

On the other side, Figure 3.16 shows the effect of the cutting angle of the TDRA radiation pattern at α =9°, α =27°, and α =40° and illustrates how the radiation beam pattern evolves with changes in the angle α.

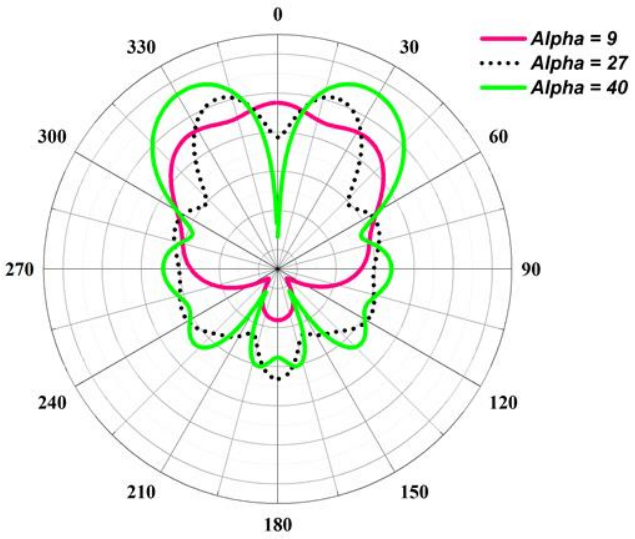

(a)

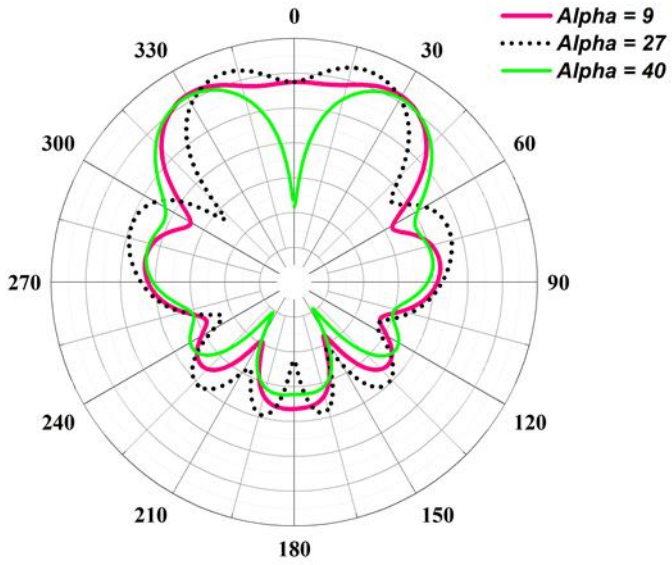

(b)

Figure 3-16 Radiation pattern of different cutting angles (a) at 28GHz, (b) at 33GHz.

- At α =9°, the radiation beam is directed predominantly in one direction. The pattern shows a concentrated beam, indicating minimal spreading or diffraction effects.

- At α =27°, the pattern begins to split, signifying the onset of beam divergence. This transition point reveals the start of significant spreading in the beam's directionality.

- At α =40°. The radiation beam has evolved into a double beam pattern. This indicates further splitting and broadening of the beam, resulting in two distinct radiation lobes. The

increased angle has led to more pronounced diffraction effects, splitting the beam into multiple directions.

Finally, the desired dual band behavior with distinctly separate beams is effectively realized as illustrated in Fig. 3-17 (a) and (b); the TDRA achieves a significant beam separation of over -20 dB. The antenna exhibits dual beam patterns at 28 GHz where the beams are positioned at ±28° with an angular width of 31.9°, while at 33 GHz the beams are at ±31° with an angular width of 30.1°. This pronounced beam separation and well-defined angular coverage across both frequencies demonstrate the TDRA's enhanced performance and precision in delivering high quality distinct radiation patterns.

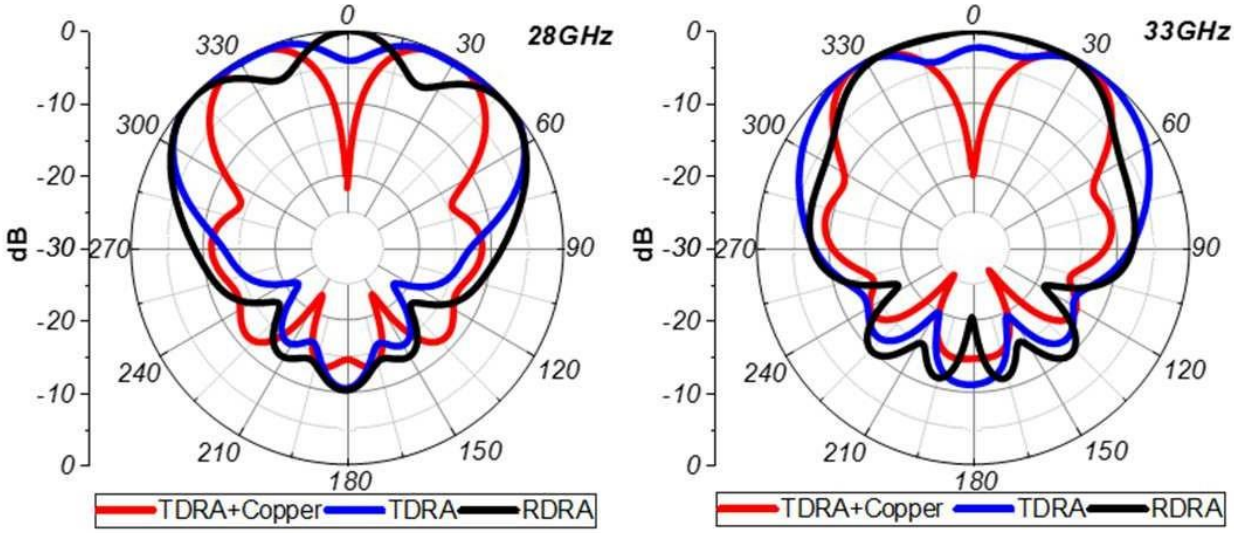

Figure 3-17 Radiation patterns in the E-plane at 28 GHz (left) and at 33 GHz (right).

3.7 Conclusion

This chapter has introduced an innovative miniaturized dual-band TDRA array with an upper copper metallization layer that enables dual-beam functionality. The designed structure achieves effective beam pointing coverage with symmetric radiation patterns centered at ±28° for 28 GHz and ±31° for 33 GHz. This dual-beam configuration not only ensures high radiation efficiency but also supports a relatively wide impedance BW, enhancing overall performance. The miniaturized TDRA array thus demonstrates its capability to deliver precise and high-efficiency radiation patterns across both specified MMW frequencies while maintaining robust impedance characteristics.

CHAPTER IV: Novel High Efficiency V-Band Pure TEM D-PRGW Antenna for 5G MMW Applications

4.1 Introduction

The fifth generation of wireless systems is set to provide improved functionalities, including faster data rates and lower latency. However, increasing device connectivity has led to congestion in the sub-6 GHz frequency band, approaching capacity limits and resulting in slower services with more dropped connections. To address this drawback, researchers are exploring the MMW band, ranging from 30 to 300 GHz, which offers significant potential. However, the MMW band encounters severe challenges due to its relatively short wavelength (1–10 mm), which can cause blockages from obstacles and atmospheric absorption during transmission.

Additionally, at higher frequencies, the antenna dimensions become narrower, leading to increased current density and conduction loss [182]. Consequently, the conventional microstrip transmission line may not be efficient enough for antenna feed [183]. Besides, a high level of accuracy and precision is necessary in the manufacturing process to build such a small structure while maintaining good electrical contact between adjacent elements with minimum interference.

To address these challenges, various approaches have been suggested in existing literature with enhanced efficiency, increased gain, and broader BW. One of the most promising techniques is RGW technology, which offers reduced insertion loss and self-packaging capabilities [184]. This section deals first with the proposal of an enhanced version of a planar rectangular slot antenna fed by the quasi-TEM printed ridge gap waveguide (PRGW), attended with a numerical study of a miniaturization procedure showing the limitations of the conventional PRGW-based antennas. Next, an innovative solution is presented introducing a new miniaturized pure TEM wide-band slot antenna utilizing D-PRGW technology. The performance supremacy of the proposed antenna is then assessed through a comprehensive comparative study including the most efficient conventional techniques.

4.2 PRGW technique and its limitations

As explained in chapter 2, the conventional PRGW configuration involves eliminating the normal parallel plate modes by incorporating a HIS around a strip line made of a PEC. As a result, the wave propagation occurs exclusively within the air gap between the ridgeline and the upper metallic plate, extending uniformly throughout the structure in the form of Quasi-TEM mode. Hence, this structure significantly reduces dielectric losses since the propagation takes place within an air gap.

This feeding technology has found its way into numerous research endeavors. In [185] a wide band slot antenna fed by a simple PRGW and further enhanced by using a Frequency Selective Surface acting as a Fabry Perot Cavity, to reach 15dbi gain. In the work in [186], a dual polarized Magneto Electric (ME) dipole antenna realized upon an AMC sidewall cavity and excited by two orthogonal PRGW lines, implemented on two substrate layers that operates in the Ka band, has reached a relative impedance bandwidth of 23.4% and a 10.5dbi gain. In 2018, Zhang et al. [187] have proposed a modified version of PRGW that stands on replacing the air gap by a dielectric substrate for compactness ; the obtained results was then improved by using different tuning configurations around the radiating slot. The achieved gain was around 6dbi for single slot and 11dbi for the 4×1 array.

The PRGW supports a Quazi-TEM mode propagation along the ridge. This propagation mode is considered relatively dispersive in comparison to the pure TEM mode supported by a smooth parallel PEC waveguide [188]**.** This effect is mainly attributed to the horizontal asymmetry AMC-PEC between both the top and bottom layers, causing some extended fringing fields to spread outside the borders of the ridge area into the upper plate. Consequently, the performance will decrease and several rows of textured HIS surfaces will be needed to surround the ridge from both sides in order to compensate for the power loss and eliminate all the leaked surface waves effectively.

However, at this point, it is worth pointing out that in the works mentioned above, the conventional PRWG feeding of a single slot antenna just by itself was found to be not efficient, leading to the exploration of alternative design strategies. Therefore, the final designs were either:

- Arranged in the form of an array antenna [187] as shown in Figure 4.1(a).

- Used to excite another type of radiating element such as an ME dipole [186] as shown in Figure 4.1(b) , DRA [189] as shown in Figure 4.1(c), or even patches [190] as shown in Figure 4.1(d).
- Backed with a superstrate layer [191] or Fabry Perot Cavity (FPC) [192] as shown in Figure 4.1(e).

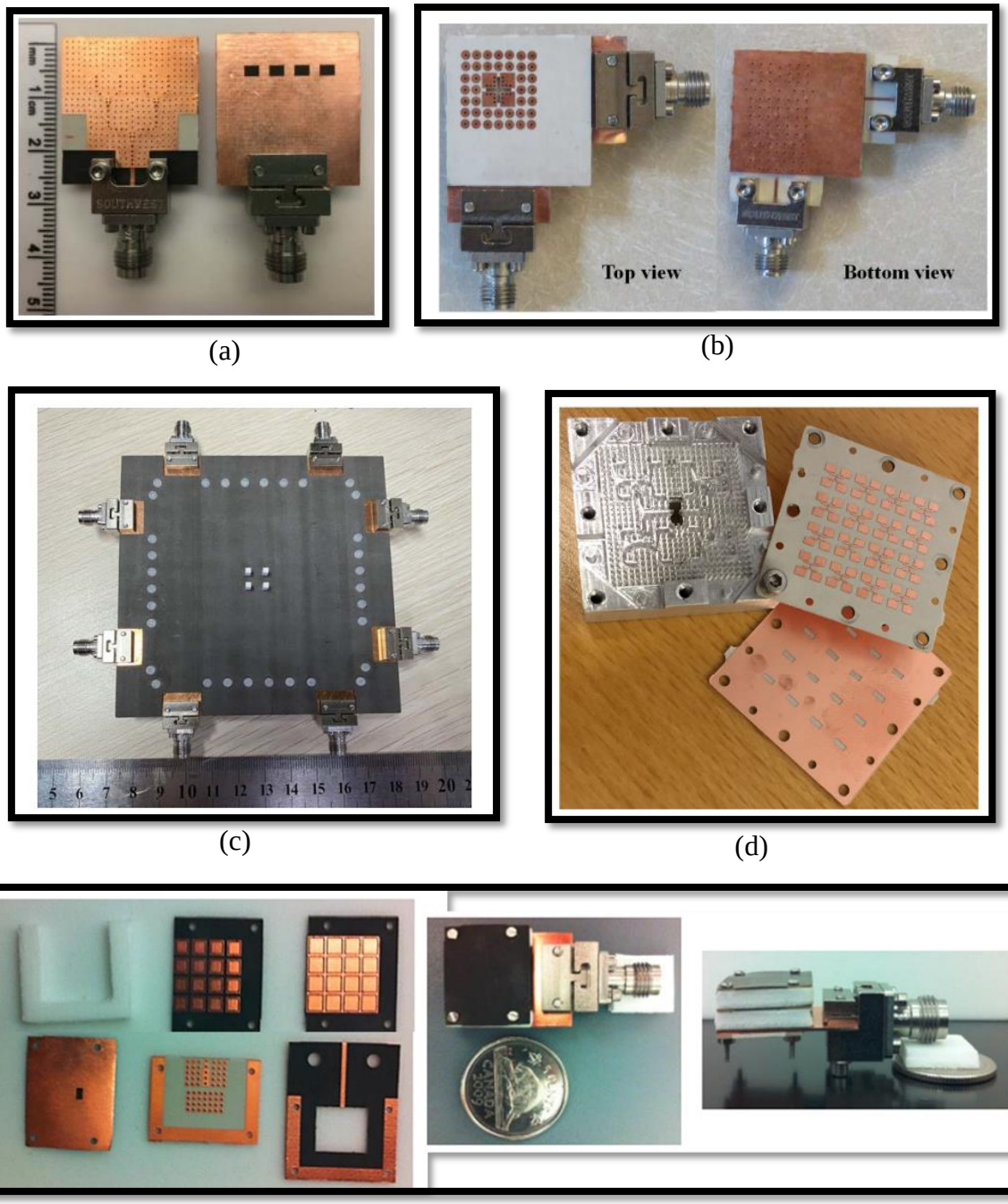

(a) (b) (c) (d) (e)

Figure 4-1 Examples of incorporation of RGW with several enhancement techniques, (a) Array structure, (b) ME dipole, (c) DRA, (d) Patches, (e) FPC.

By way of illustration, in [185] the gain of the slot antenna was about 4dBi. However, after adding the FSS layer, it jumped to 15.6dBi. The same remark can be done in [187] where the gain has reached approximately 7dBi when the cavity exciting the optimized offset (in both directions X and Y) slot was tuned, and then, a 4×1 array was arranged to increase the gain to 12dBi. Therefore, despite achieving satisfactory results, all of these approaches present the inconvenience of a bulky structure that would not be suitable for integration in small-size devices and appliances.

In summary, even though PRGW is better than a microstrip line as a feeding structure at higher frequencies, the challenge remains to address the significant losses around the ridge area. This drawback should be fixed in order to deliver the signal more properly to the radiation slot and get better performance without the need for any additional modifications or components that would make the overall structure bulkier. Furthermore, the dimensions of the design must be reduced as much as possible without affecting the performance in order to make it suitable for 5G wireless devices.

This issue must be resolved to ensure efficient signal delivery to the radiation slot and improve the overall performance without introducing additional bulkiness through modifications or extra components. Moreover, reducing the dimensions of the design without compromising performance is crucial to making it suitable for integration into 5G wireless devices. This is why this section focuses on improving the PRGW performance from the slot antenna alone and without the exploration of any additional structures that would result in massive design.

4-3 D-PRGW technology

On the other hand, the development and implementation of the novel D-PRGW technology, initially proposed and examined in [193], as a wave-guiding structure operating in the Ka-band, represents another promising advancement. This technology, as shown in Figure 4.2, incorporates a double AMC textured surface in both the upper and lower layers, resulting in an asymmetrical structure featuring a dual ridge line on each side.

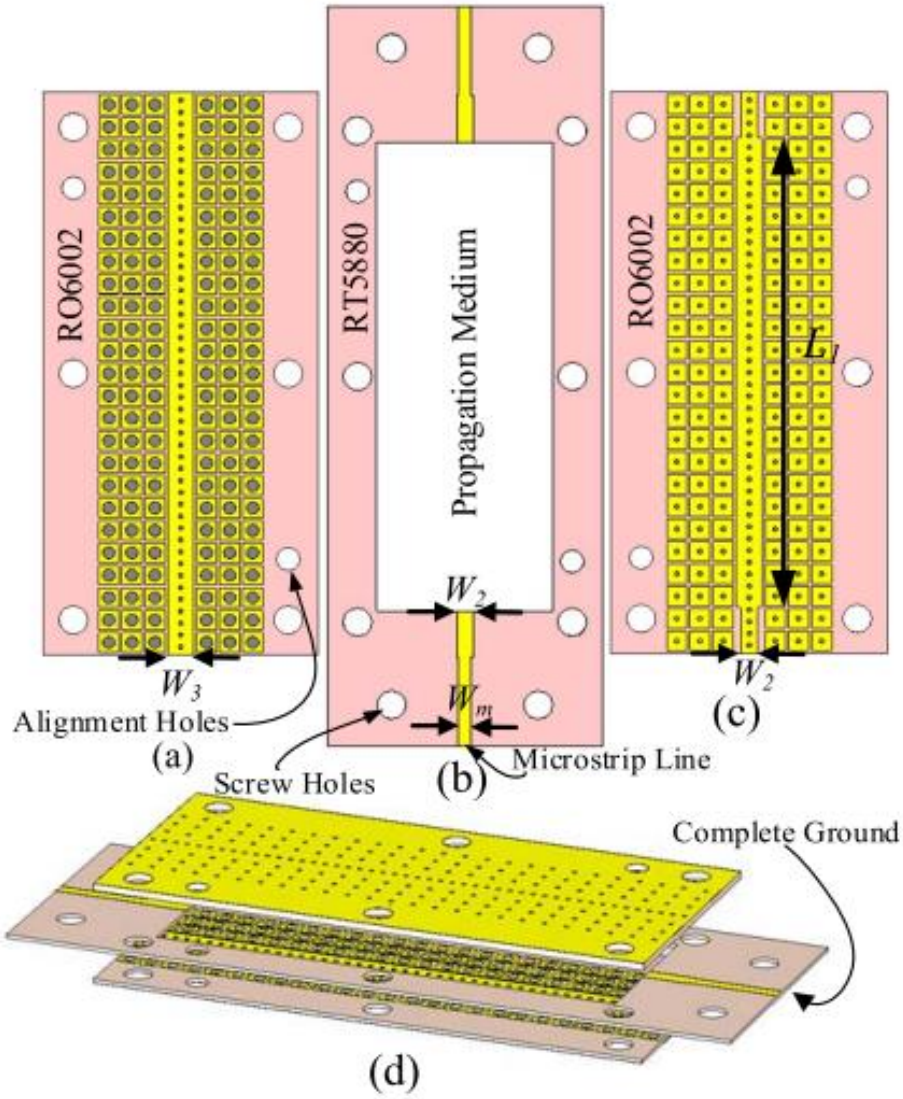

Figure 4-2 Geometry of the D-PRGW. (a) Lower thin AMC layer with straight ridge. (b) Middle microstrip feeding layer. (c) Upper thick AMC layer with straight ridge. (d) 3-D view of the stacked layers.

Consequently, the signal will be entirely confined within the symmetrical double ridge zone, with minimal fringing fields outside the ridge boundaries even with the presence of two 90° bends, the corresponding results are depicted in Figures 4.3.

This configuration closely mimics an ideal parallel plate PEC/PEC waveguide, as the propagating mode is predominantly a pure TEM instead of a Quasi-TEM mode. As a result, undesired leakage outside the ridge's borders is automatically limited, potentially reducing the number of rows required to eliminate surface waves. Subsequently, this technology was introduced in [194] to feed a simple TEM H-plane horn antenna, marking it as the only instance in the literature where the D-PRGW technology serves as a feeding structure.

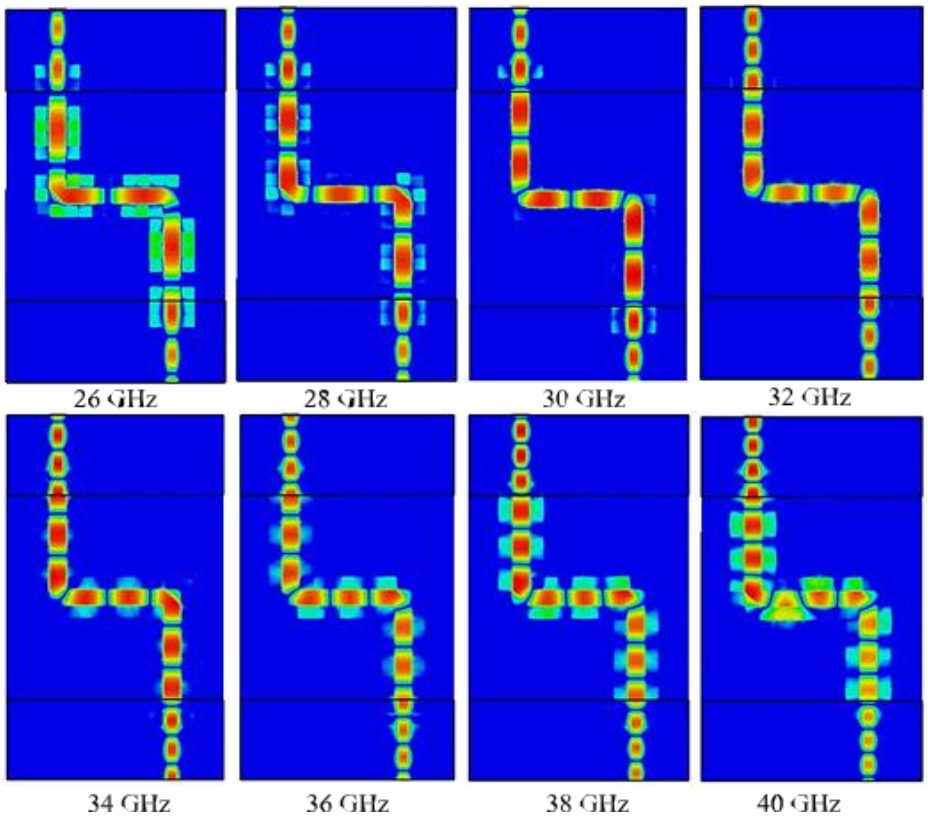

(a)

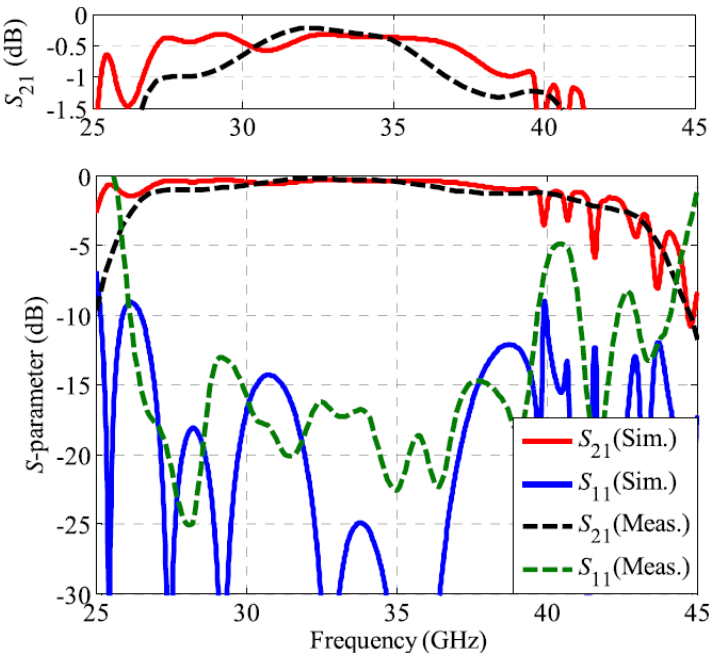

(b)

Figure 4-3 (a) E-field distribution inside the D-PRGW with two 90° bends at different frequencies. (b) Simulated and measured reflection and transmission coefficients of the D-PRGW with two 90° bends and four wavelengths length.

4.4 Enhanced PRGW antenna

The objective in this section is to underscore the limitations of PRGW technology, particularly at high frequencies, by designing an enhanced slot antenna fed by the PRGW, operational in the V band. For this purpose, a numerical analysis is conducted to introduce and explore a miniaturization process applied to an optimized planar rectangular slot antenna design fed by the conventional Quazi-TEM PRGW. This miniaturization involves iteratively removing one row of textured surfaces to evaluate its impact on antenna performance and physical size.

The presence of surface waves can degrade signal propagation, especially at the interface between different materials with varying refractive indices (such as between metal and free space). These waves are bound vertically to the surface as vertical TEM (V-TEM) waves when scattered by irregularities, boundaries, or textured surfaces. They can be mitigated by using a HIS that simulates equivalent boundary conditions [70] effectively acting as a perfect magnetic conductor (PMC) within a specific frequency range, commonly known as an artificial magnetic conductor (AMC).

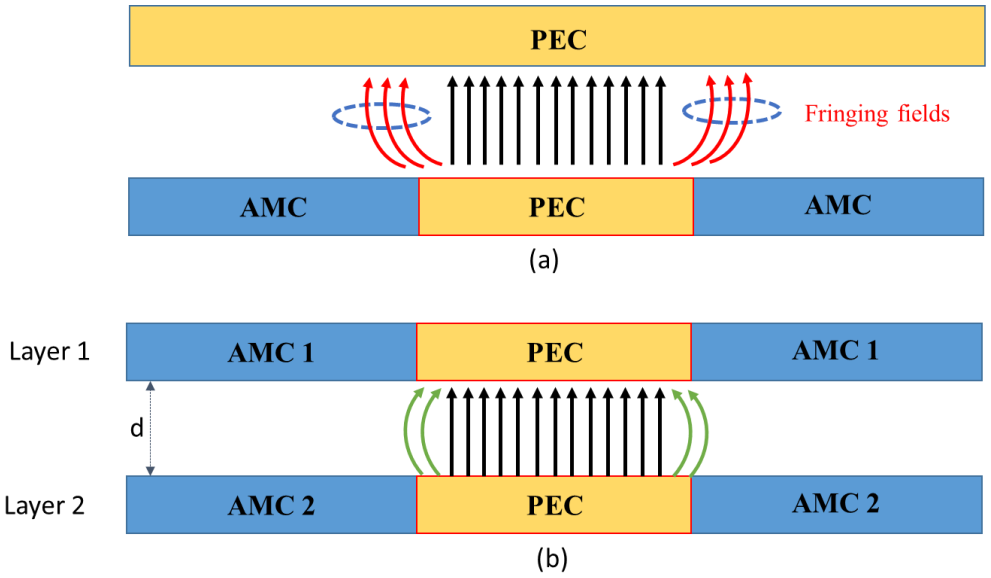

Figure 4-4 (a) Configuration of dispersive conventional PRGW (b) Configuration of the novel D-PRGW.

One of the most widely used types of AMC is the EBG mushroom-type lattice, which comprises a shaped metal pad grounded by metalized via holes and separated from a parallel PEC metal plate by an air gap. This design has been employed in various studies, such as those in [195], [196], and [197], to suppress surface waves around the ridge of the planar

resonant grating waveguide PRGW within a desired frequency range. However, the propagation of waves will not be confined solely along the ridge line due to the fringing fields leaking into the upper layer, which significantly reduces the structure's efficiency, as illustrated in Figure 4.4.

4.4.1 Design steps

The design methodology of this proposed work is illustrated in Figure 4.5.

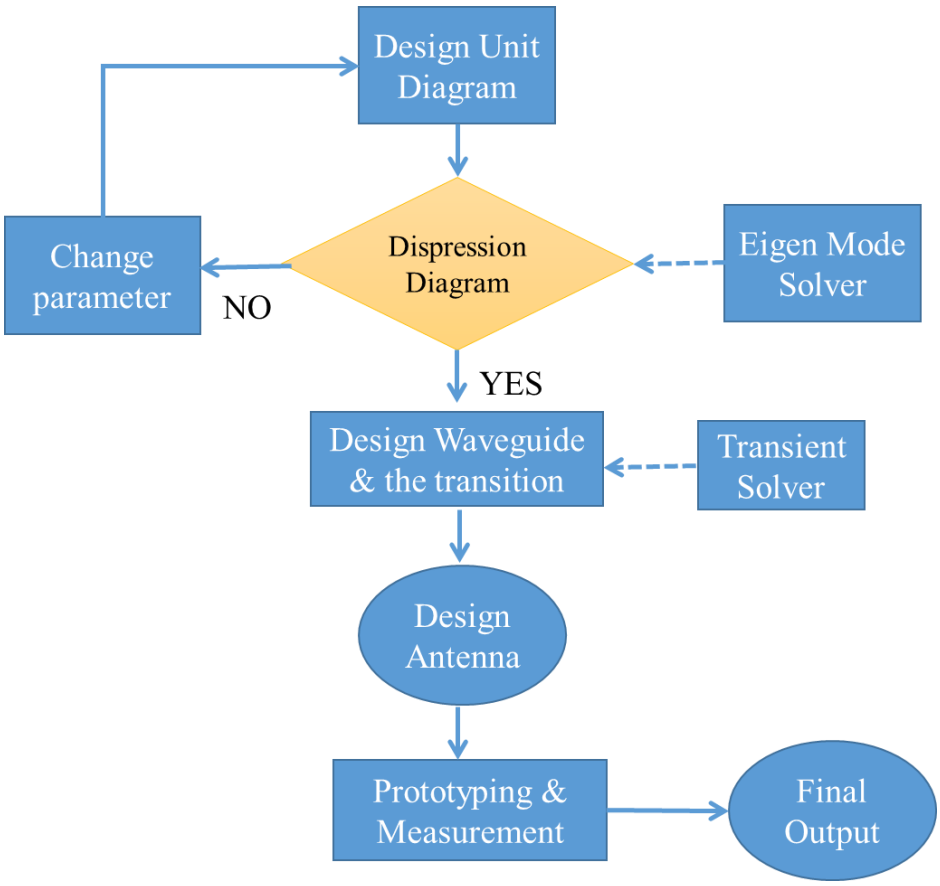

Figure 4-5 Design methodology.

4.4.2 Design characteristics

A ridge line of width w_r=1.25mm is printed on a Rogers's substrate RO3003 with a dielectric constant ε_r=3 and a loss tangent δ=0.001 and surrounded by several rows of EBG mushroom surface from each side and grounded by plated vias to eliminate any leakage into the substrate. The EM field will propagate in the air gap between the ridge line and the top metallic parallel plate to excite a rectangular slot embedded in the copper cladding of substrate Rogers RT/duroid 5880 with a dielectric constant ε_r=2.2 and a loss tangent δ=0.001.

In the design of the EBG lattice, the following conditions must be satisfied [198];

$$\frac{d}{c} < 0.4 \quad (4.1)$$

$$\frac{d}{p} \geq 0.5 \quad (4.2)$$

Where d is the vias diameter, p is the periodicity, and c is the length of the unit cell.

4.4.3 Dispersion diagram

The dispersion diagram of the conventional EBG unit cell and the line segment depicted, respectively, in Figure 4.6 and Figure 4.7, show a wide cutoff region that extends among the whole V band, where no mode is allowed to propagate.

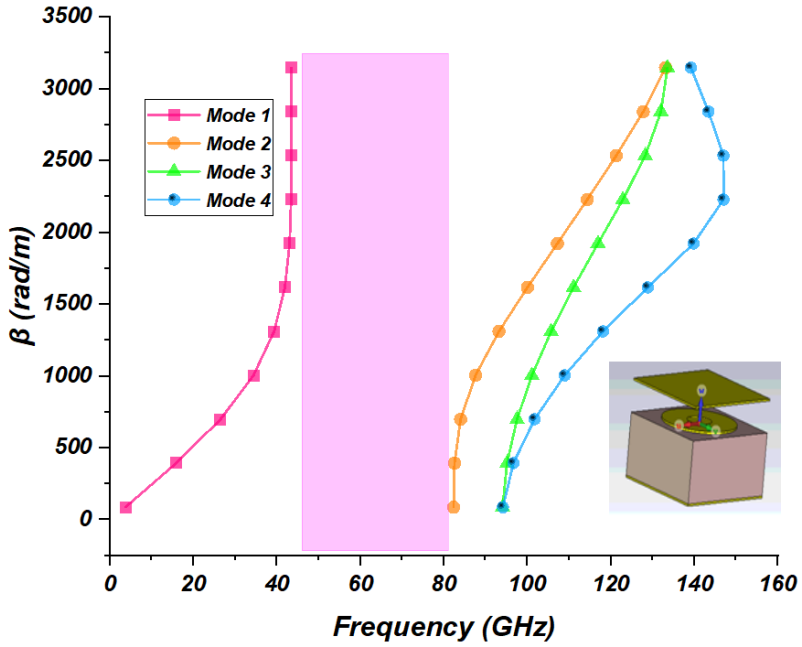

Figure 4-6 Dispersion diagram of conventional single layer EBG unit cell.

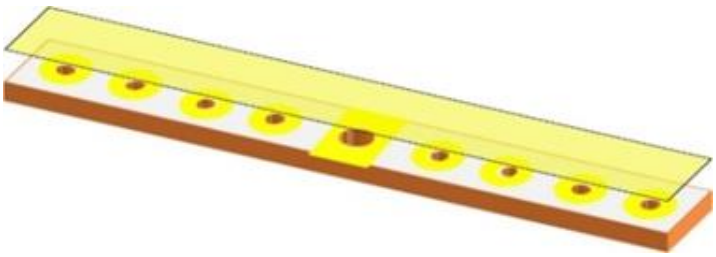

(a)

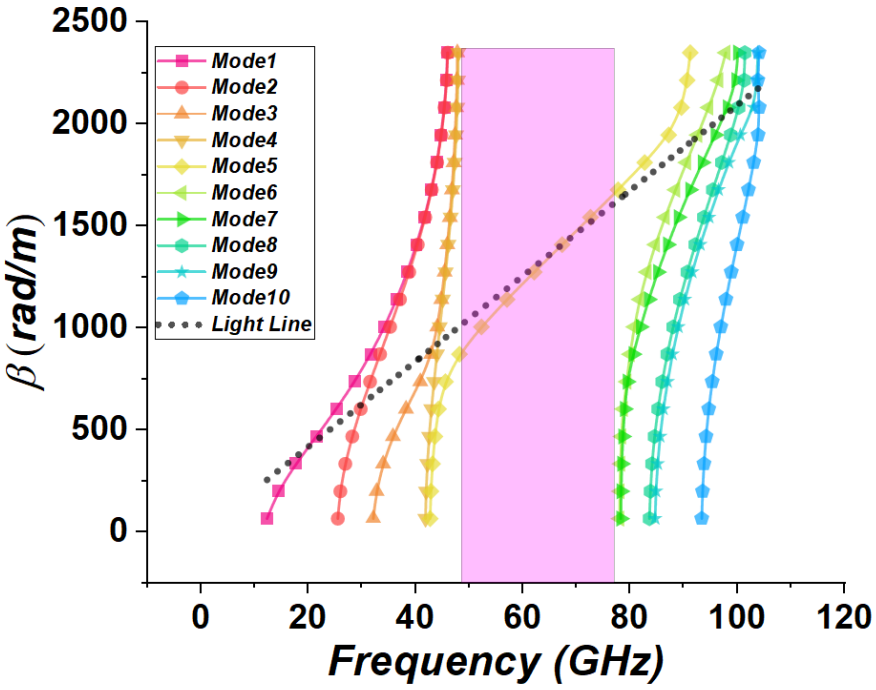

(b)

Figure 4-7 Three Single-layer line segment study; (a) line segment section, (b) its dispersion diagram.

4.4.4 Miniaturization procedure

In the first step of the design, five rows of EBG mushroom surfaces were added at both sides of the ridge line and five rows behind the radiating slot to ensure eliminating all possible surface waves effectively. A regular 50Ω micro strip line is printed on the bottom side of the support substrate holding the upper metallic plate to feed the structure as shown in Figure 4.8. Since we aim to explore the limitations of PRGW technology, the dimensions and placement of the slot were optimized to deliver the best performance in terms of BW, gain, and efficiency, to be further miniaturized.

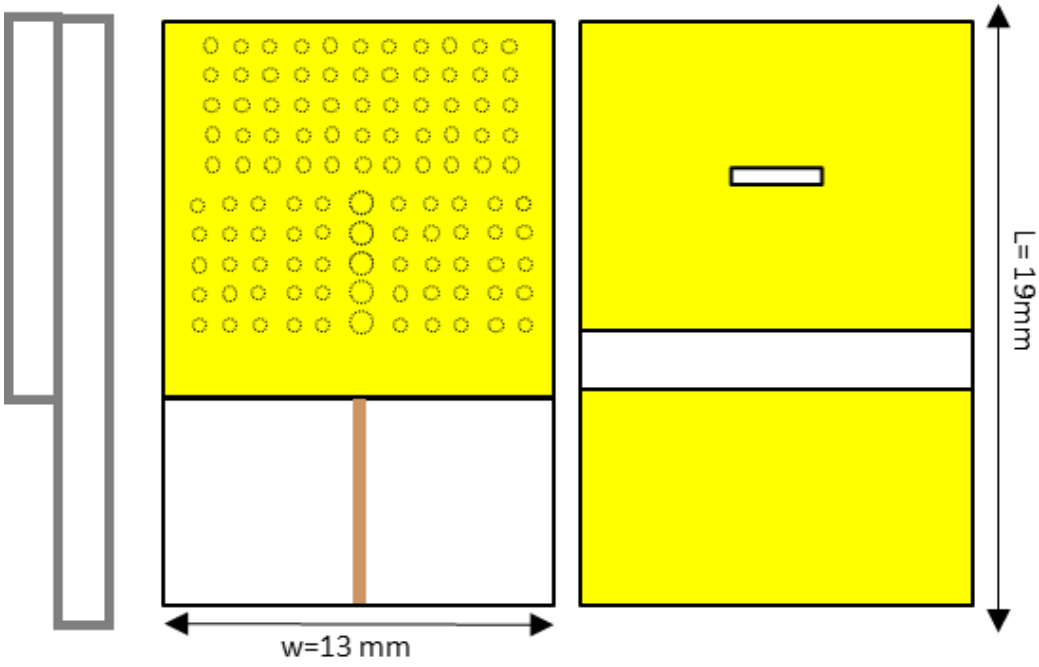

(a) (b) (c)

Figure 4-8 Enhanced conventional PRGW slot antenna. (a) Side view. (b) Bottom view. (c) Top view.

Furthermore, since this work is dedicated to mobile terminals wireless communication, the overall size of the antenna must be compact. Therefore, a miniaturization approach was applied to reduce the structure dimensions. This procedure consists of eliminating one row of EBG at a time from each side of the ridge line while maintaining the same size and location of the radiating slot as shown in Figure 4.9.

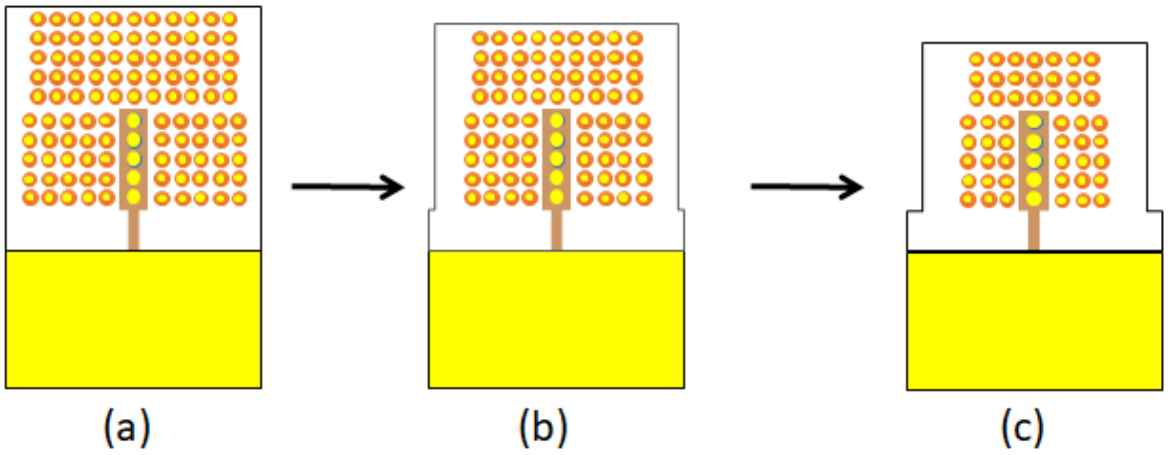

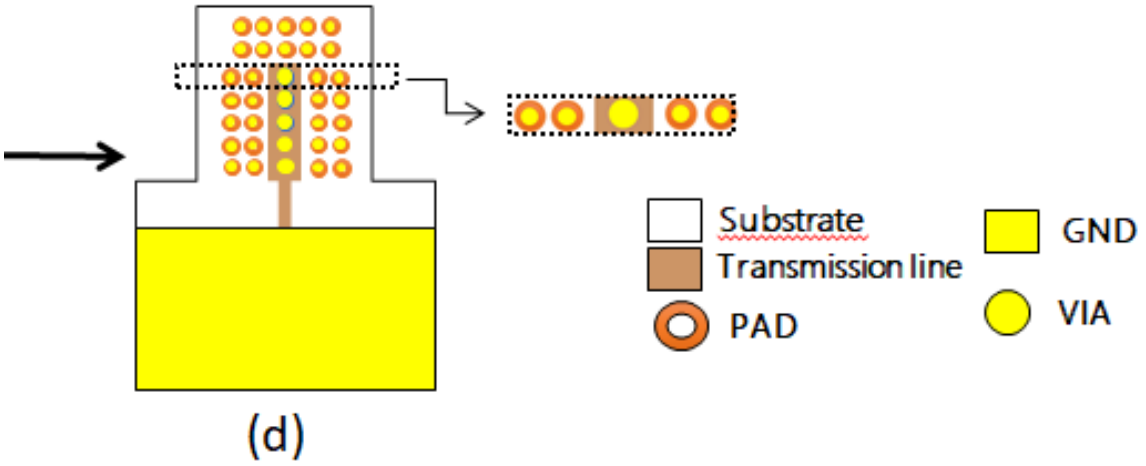

Figure 4-9 . Miniaturization procedure of conventional PRGW slot antenna. (a) Antenna1 with 5 rows of EBG. (b) Antenna 2 with 4 rows of EBG. (c) Antenna 3 with 3 rows of EBG. (d) Antenna 4 with 2 rows of EBG.

From the obtained results shown in Figure 4.10, it is clearly seen that the performance has drastically decreased each time one AMC row is suppressed around the ridge. The BW is reduced from 6.5Ghz large (57.5GHz-64GHz) when the structure has full five rows to only 3.2GHz (59GHz-62.2GHz) for the final case with just two rows and the gain has decreased from a peak of 9.5dBi centered at 61GHz to a 6dbi peak at 62GHz.

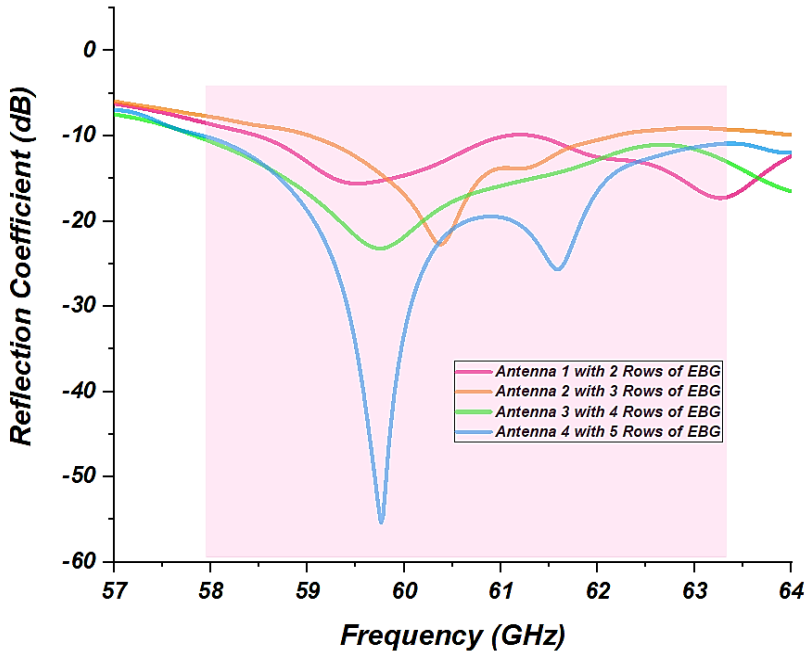

(a)

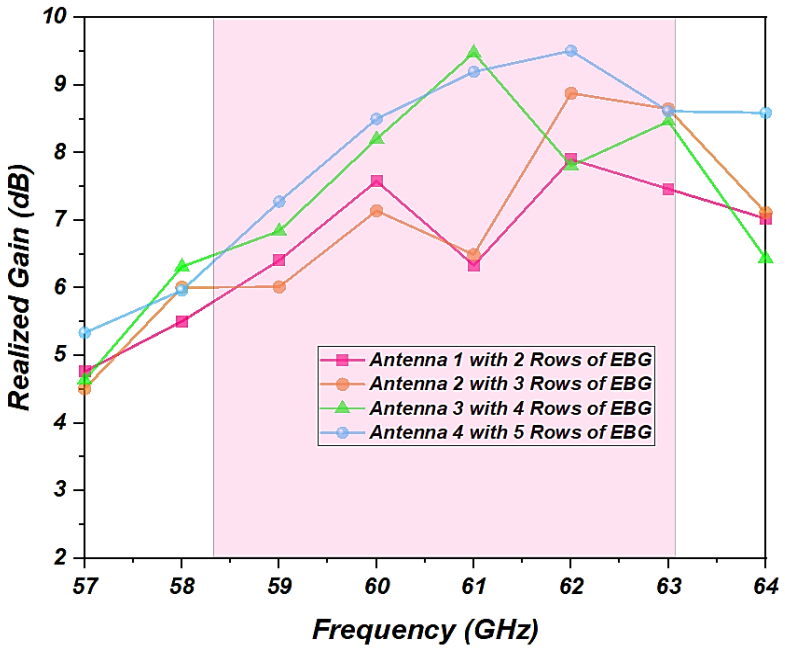

(b)

Figure 4-10 Antennas' performances for different EBG rows. (a) Reflection coefficient. (b) Realized gain.

4.4.5 Essential Analyses

These results lead us to conclude that the traditional PRGW faces a serious limitation in maintaining good confinement inside the ridge line and properly delivering the signal to the slot, due to the fact that it requires at least four or more operating rows of textured surface on either side of the ridge to suppress the fringing fields leaking outside. Consequently, we get large planar dimensions that can no longer be miniaturized. In addition, it must be backed with another type of antenna or a superstrate layer to reach coherent results, which makes the overall design even bulkier and not suitable for integration in small-size devices.

4-5 Proposed V-Band Pure TEM D-PRGW Antenna

In this chapter, the design of novel V-Band pure TEM slot antenna, effectively miniaturized and fed by the abovementioned innovative D-PRGW technique, is proposed and validated. Besides, a comprehensive analysis of the antenna's performance evaluation is given together with a detailed discussion of the fabricated prototype. Finally, the outcomes of this work were summarized and discussed.

This antenna stands out for its minimal elements, compact dimensions, reduced insertion loss, and concentrated power around the double-ridge area, distinguishing it from the conventional single-layer PRGW.

The proposed antenna design methodology is the same as that illustrated in Figure 4.5.

4.5.1 Novel Double EBG unit cell and line segment analysis

To begin, less dispersive double EBG unit cells using the Eigenmode Solver is designed and simulated to ensure coverage of the required operating frequency band. This latter, shown in Figures 4.11, involves incorporating two parallel textured surfaces in both layers of the structure. This configuration creates a parallel AMC/AMC cutoff region, effectively eliminating all undesired fringing fields. The boundary conditions set by the parallel AMC/AMC and PEC/PEC guiding medium facilitate a pure TEM propagating mode, as opposed to the quasi-TEM mode seen in conventional PRGW designs. The AMC/AMC lattices surrounding the double-ridge line can be identical or different, with the spacing between the two layers meeting the following specific criteria to suppress propagation outside the ridge region.

$$The\ gap\ (d)\ \ll \begin{cases} \lambda/_4, & Assymmetrical(AMC1 \neq AMC2) \\ \lambda/_2, & Symmetrical(AMC1 = AMC2) \end{cases}$$

In the scenario where identical AMC with spacing d is utilized, the double AMC unit cell can be seen as a mirrored version of a single AMC unit cell from the conventional RGW, but with a gap of d/2 where the ground plane is excluded. This implies that the D-PRGW with identical AMC will exhibit the same band gap as the conventional RGW but with twice the gap height. Additionally, if the gap height is less than λ/2, the symmetrical AMC/AMC will propagate Horizontal (H-TEM) waves, while the PEC/PEC parallel-plate region will propagate Vertical (V-TEM) polarization waves.

On the other hand, if the gap height equals or exceeds λ/2, both polarizations will be supported by the two parallel regions. This indicates that selecting an appropriate height will naturally eliminate V-TEM surface waves within the symmetrical AMC/AMC area. However, if H-TEM modes happen to be excited at line discontinuities or corners, they may propagate within the horizontally identical AMC/AMC gap instead of between PEC/PEC. This occurs because the upper and lower edges of the guiding region share identical boundary conditions

[199], which could lead to leakage outside the guiding medium. Consequently, in this design, an asymmetrical AMC/AMC configuration with varying surface impedances is employed to establish a complete stop band for all potential horizontal or vertical modes.

The double-layered AMC/AMC unit cell is fabricated on Rogers's RO3003 substrate. The lower layer incorporates a textured cylindrical metallic pin of height h_2=0.254mm and width d_2=0.9mm , that is connected to the ground plane. In contrast, the upper layer is designed as a mushroom-type structure having a circular metallic patch of width w_1=0.8mm, height 17µm, corresponding to the copper cladding's thickness of Rogers's RO3003 substrate) grounded by a plated metallic pin of diameter d_1=0.2mm, height h_1=0.5mm.

The width of the stop band is controlled by the height of the gap that separates the upper and lower layers, as discussed in references [200] and [201]This gap height, denoted as h_g, plays a critical role in determining the stop band's extent and is constrained by practical considerations such as the thickness of the supporting substrate (in this case, Rogers RT/duroid 5880). Due to fabrication limitations, the gap height is set at h_g=0.5mm to align with the available substrate thickness.

4.5.1.1 Dispersion diagram

The dispersion properties of the proposed double AMC unit cell are analyzed using the Eigen mode solver in CST Studio and the resulting dispersion diagram depicted in Figure 4.11. This unit cell has achieved a wide cut-off frequency range from 42 GHz to 74 GHz, covering all the V bands between mode 1 and mode 2, with the electric field distribution exhibiting vertical polarization.

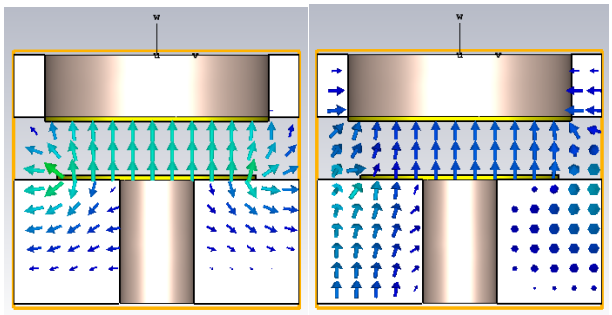

(a)

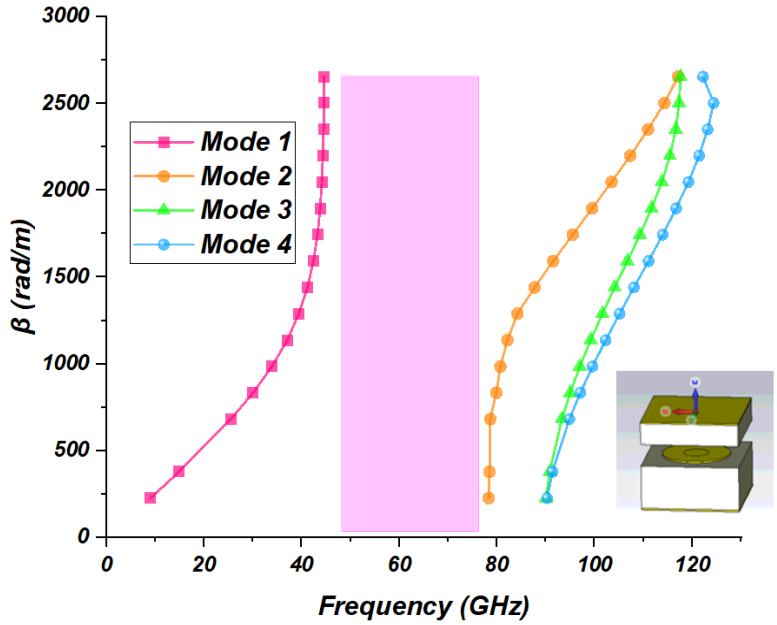

(b)

Figure 4-11 EBG unit cell characterization. (a) E-field distribution of mode 1 and mode 2, (b) Dispersion diagram of the Double-layer EBG unit cell.

Following the optimization of the double AMC unit cells, they were arranged in a periodic 2D lattice formation comprising two rows on each side of the double ridge. This arrangement effectively suppresses both V-TEM and H-TEM surface waves simultaneously, ensuring strict confinement of propagation along the double ridge line area. Due to the periodicity along the y-axis, a single transverse segment of the D-PRGW line surrounded by two rows of AMC/AMC cells on either side, under longitudinal periodic boundary conditions, is considered for extracting the dispersion diagram.

The dispersion diagram presented in Figure 4-12 illustrates a nearly pure TEM propagating mode, aligned parallel to the light line, propagating within the cut-off region formed by the double AMC/AMC lattice. The ridge width is determined based on strip line theory, followed by the drilling of a row of pins with diameters d_{r1}=0.51mm and d_{r2}=0.9mm beneath the upper and lower ridge lines, respectively. This arrangement aims to eliminate surface waves that may escape into the dielectric substrates beneath the ridge.

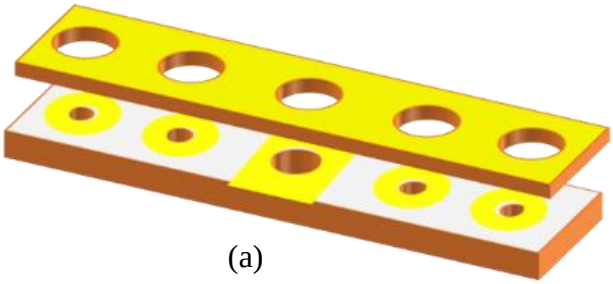

(a)

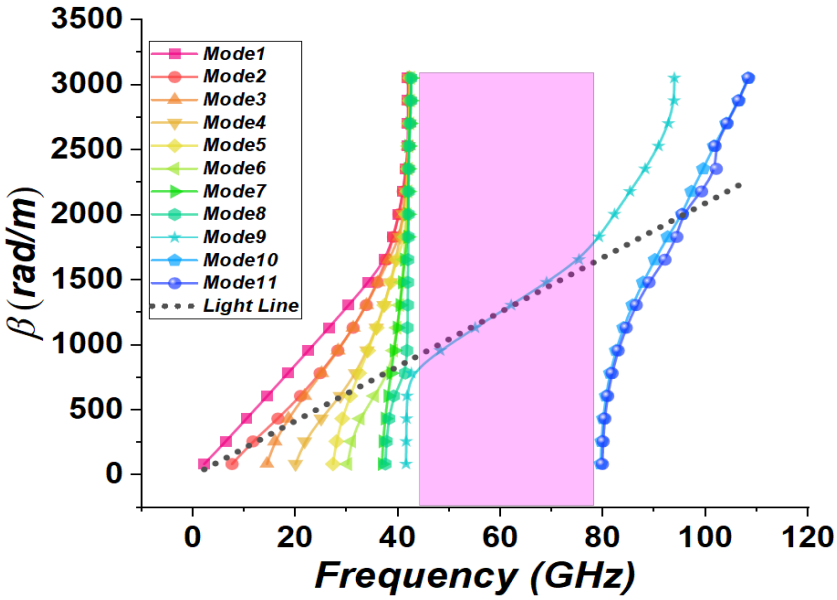

(b)

Figure 4-12 Line segment study. (a) Segment section. (b) Dispersion diagram.

In the linearly polarized parallel plate waveguide model, which supports a pure TEM mode, the structure consists of textured AMC walls holding two parallel PEC/PEC plates separated by a low permittivity material. This configuration mirrors the boundary conditions of the D-PRGW's cutoff region. Notably, the lower cutoff frequency in the parallel plate waveguide remains unaffected by planar dimensions (x, y) as long as the parallel condition is met, resulting in performance close to a parallel plate waveguide. Accordingly, the characteristic impedance of the D-PRGW is expected to closely match the fundamental expression related to the characteristic impedance of the transmission line in an ideal parallel-plate waveguide because of the similarity in the boundary conditions around the dielectric guiding medium in both cases; it can be represented as:

$$Z = \frac{\eta d}{w} \qquad 4.3$$

Where $\eta = \frac{\sqrt{\mu}}{\sqrt{\varepsilon}}$ is the intrinsic impedance of the medium between the parallel plates, d is the separation distance between them, and W is the physical width of transmission line.

This theoretical expression is valid in ideal parallel-plate waveguide case where the lateral walls are assumed to be AMC; giving no consideration to the fringing fields from the edges of the line. Consequently, there is no field variation in the transverse direction. However, in reality the fringing fields do exist around the strip of the D-PRGW. Therefore, the effective width of the strip W_{eff} increases. So, to express the D-PRGW characteristic impedance accurately and include the effect of fringing fields around the line edges , the physical width W of expression (3) should be replaced by the effective width (W_{eff}) expressed as follows.

$$W_{eff} = W + f(d) \quad 4.4$$

W_{eff} varies with respect to the gap height (d) of D-PRGW's configuration f(d) and its optimum empirical formula is obtained from [193] as follow:

$$Weff = W + 0.502d + 0.04 \quad 4.5$$

Finally, the characteristic impedance of the TEM-PRGW can be expressed as:

$$Z = \frac{\eta d}{W+0.502d+0.04} \quad 4.6$$

4.5.2 Proposed novel D-PRGW Antenna Design

Next, a line segment simulation is conducted to confirm the propagation of a single mode within the D-PRGW feeding line. The D-PRGW, as previously investigated, is employed to stimulate a rectangular slot, positioned at the termination of the upper layer's ridgeline, as depicted in Figures 4.13 and 4.14.

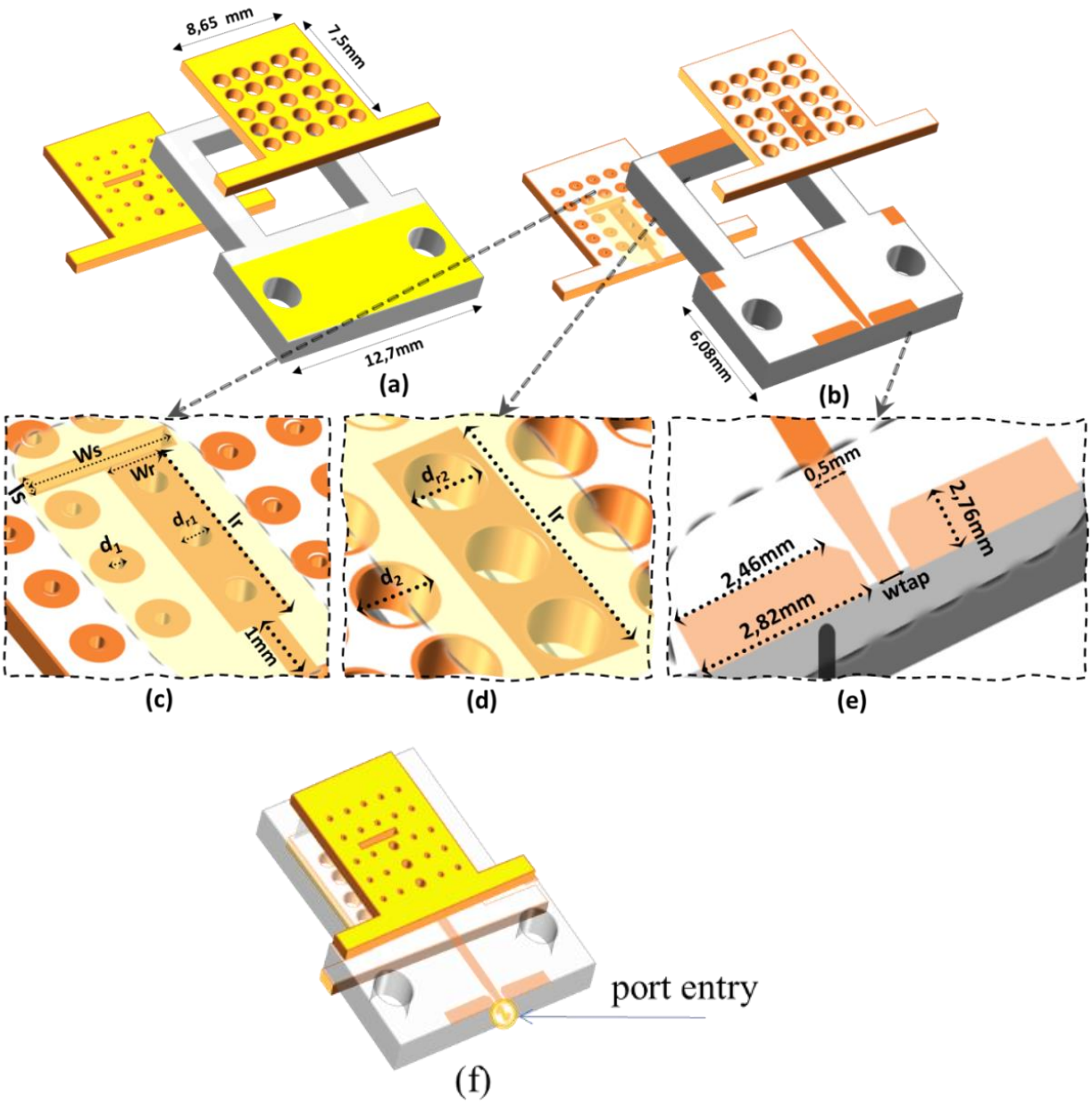

Figure 4-13 DPRGW slot antenna structure. (a) Top view. (b) Bottom view. (c) Upper ridge line with (d) Lower Ridgeline (e) Port entry (f) Final structure of D- PRGW slot antenna.

The radiating slot's position and dimensions are carefully chosen to maximize the antenna's operational BW. Here in this design, an offset feeding to the slot cavity has been used instead of the central feeding technique because according to the study established in [202]**,** the offset coupling allows the excitation of nearly all possible resonance modes inside the cavity As illustrated in Figure 4.15, the proposed design has successfully achieved an extensive operating range from 50GHz to 70GHz. A slight deviation between the measured and simulated results is noted, which mainly attributed to fabrication accuracy related to the diameter d_1 of the vias.

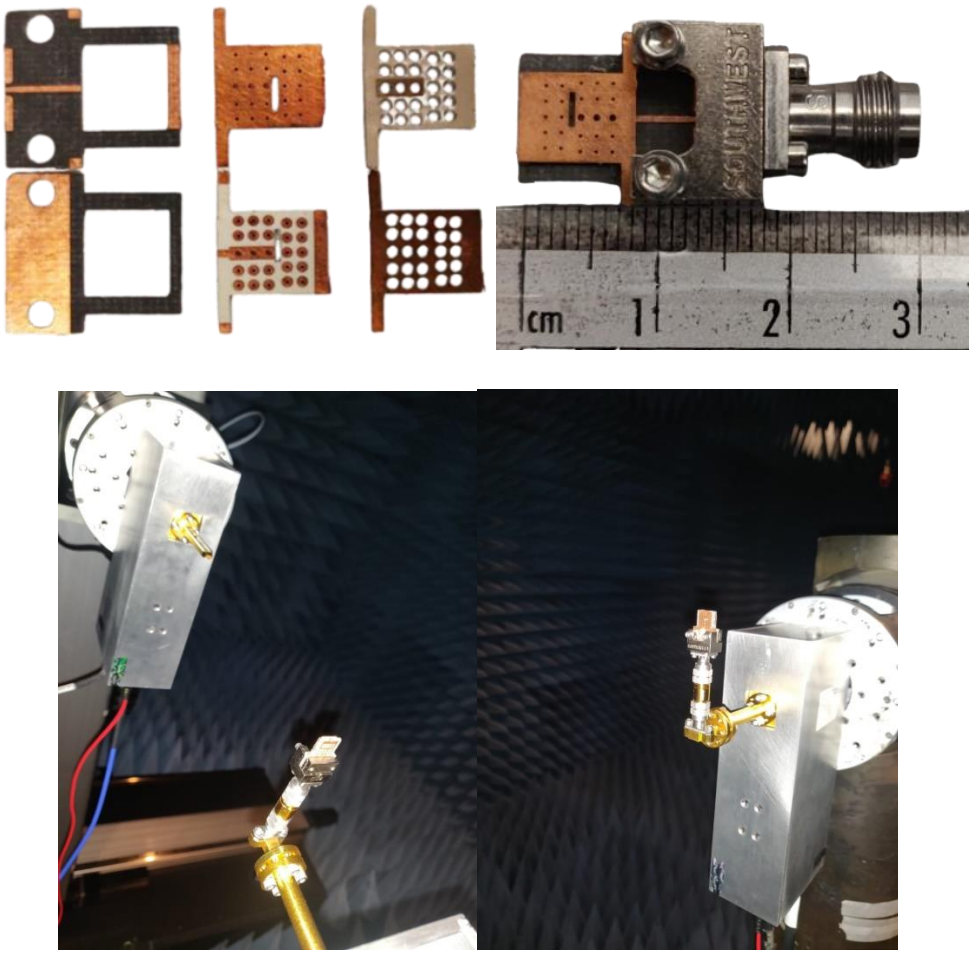

Figure 4-14 Photographs of the fabricated D-PRGW slot antenna and Antenna radiation pattern measurement setup.

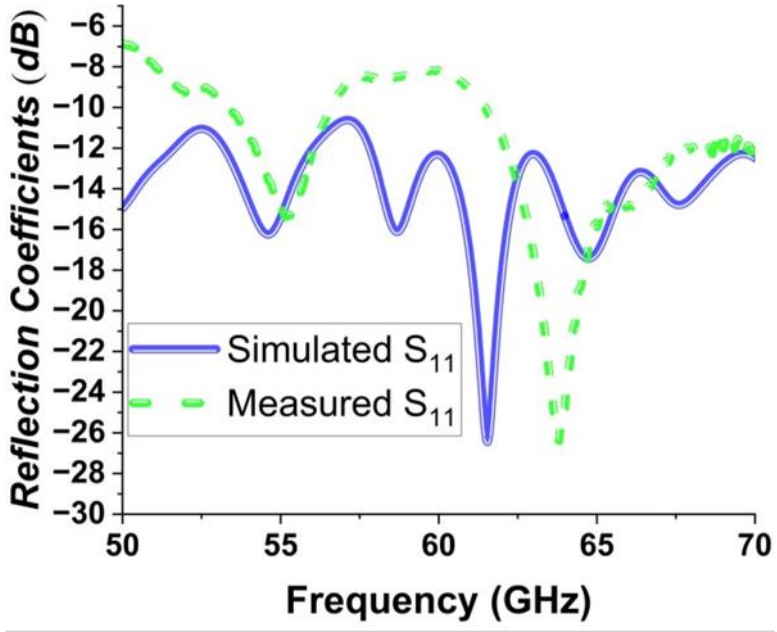

Figure 4-15 Reflection coefficient of the D-PRGW slot antenna.

The antenna exhibits significant gain throughout its BW, reaching a peak of 16dBi around 65GHz, with a high radiation efficiency exceeding 93%, as depicted in Figure 4. 16.

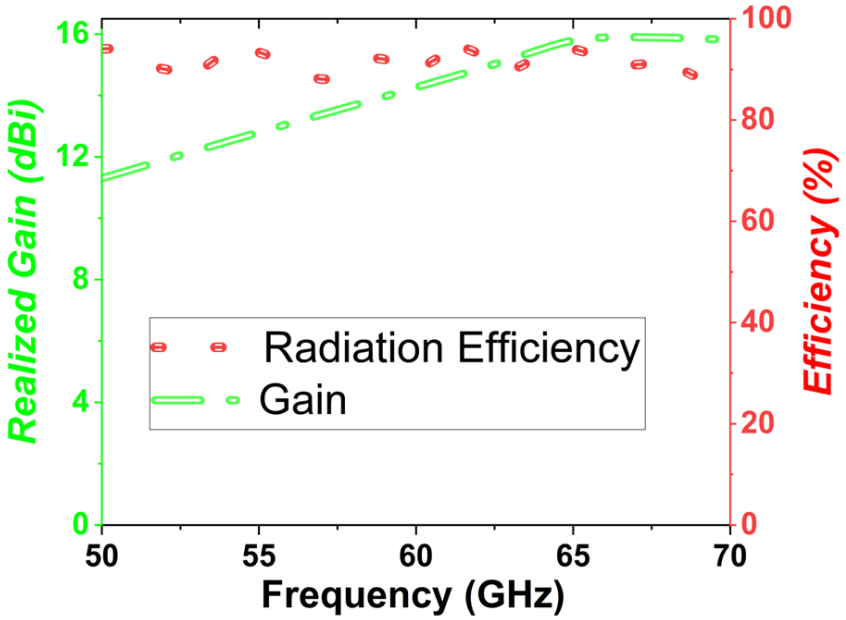

Figure 4-16 Gain and Radiation Efficiency of the D- PRGW slot antenna.

The radiation patterns have been plotted in Figure 4.17 in both (y-z plane) and Φ=900 (x-z plane) for the frequencies 55GHz, 65 GHz, and 70GHz. The cross-polar levels of the radiation patterns are more than 30dB low, which is generally the case for high gain antennas. The co-polarization beam shows a 45° tilt mainly accentuated by the antenna's asymmetry, where the slot's offset feed is altering the current flow inside the cavity aperture resulting in a tilted radiation pattern [203].

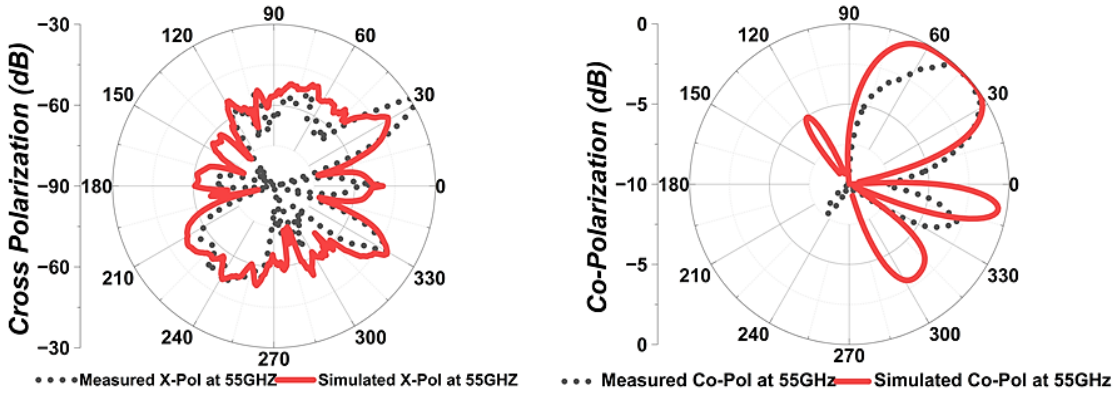

(a)

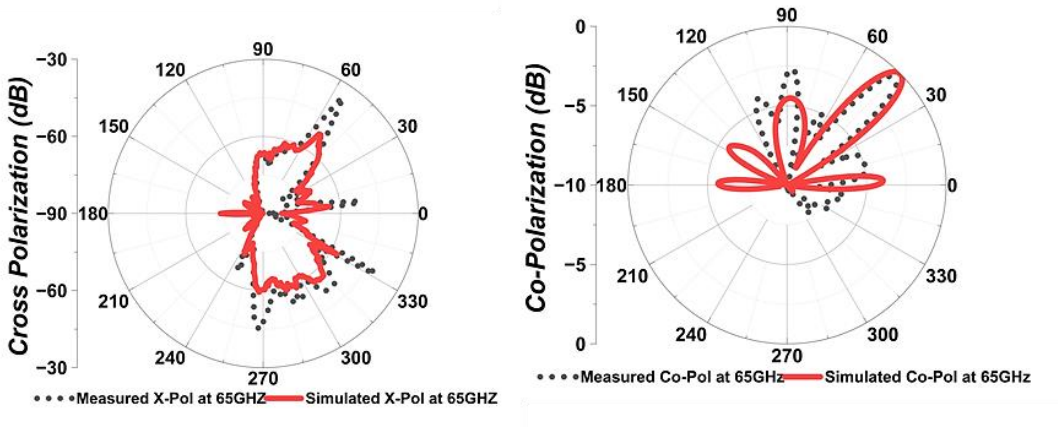

(b)

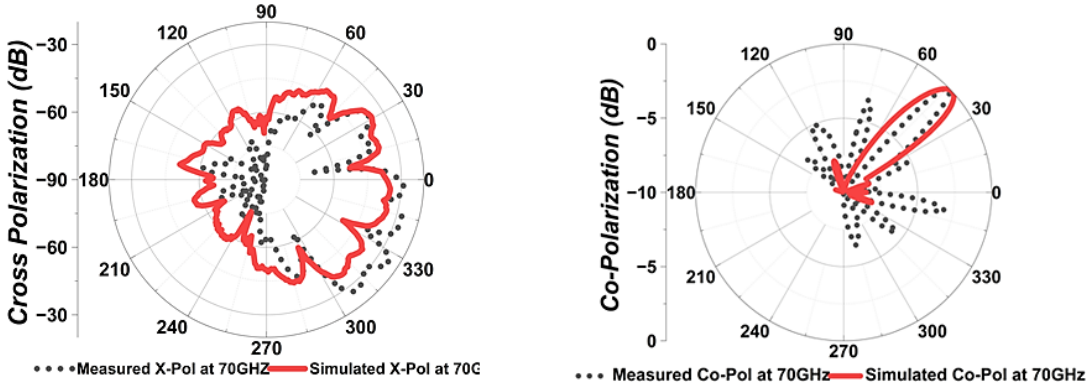

(c)

Figure 4-17 Radiation patterns of D-PRGW slot antenna at (a) 55 GHz; (b) 65 GHz; and (c) 70GHz.

This deviation is also attributed to presence of EBG lattice in the structure, which alters the refractive index with respect to the substrate; in this case, the EM wave undergoes a different phase shift from each layer resulting in a tilt in the main beam [204].

Tilted beam antenna can focus the beam towards specific direction, which will improve the efficiency and reduce interference making them good candidate for 5G wireless communication terminals. Moreover, it facilitates precise medical imaging of specific areas or organs, as well as accurate sensing of particular astronomical targets or geographical regions of interest. It can also be adjusted on cell towers mounted on high-rise buildings, for optimal coverage of the road and remote environments, making it necessary to the antenna to have a main beam oriented below the horizon. Besides, it can be used in satellite communication systems to track and communicate with satellites ensuring reliable data transmission.

The proposed miniaturized antenna is also characterized by small size, making it excellent candidate for compact devices such as smartphones, IoT, laptops, tablets, and other computing devices. Likewise, small antennas are necessary for integrating into automotive vehicles, airborne, maritime, or ground-based radar systems and satellite payloads where space and weight constraints are critical.

Additionally, its high gain and wide BW further enhance its suitability for the aforementioned applications. Its Ultra-wide BW enables high-speed data transfer and low latency required for 5G and satellite communications. It also supports high-resolution imaging for medical diagnosis, remote sensing, astronomy and spectroscopy.

To the best of our knowledge, this is the first time the D- PRGW was adopted to feed a slot-radiating antenna in the V band and the overall size of the structure is considered to be the smallest in the literature so far.

4.5.3 Design evaluation

Finally, a design evaluation of the proposed novel D-RPGW antenna has been established through a comparative study with other reported papers in the literature using the conventional GW technology. The comparison is summarized in Table 4.1, shows that the propose design has a compact size and high performance compared to the existing antennas.

The PRGW-based slot antennas can lower conduction loss at high frequencies to a certain level but at the expense of bulkiness, low gain, and narrow impedance BW since they are considered resonant structures. To overcome these limitations complementary modifications were proposed. By way of illustration in [185], the gain of the slot antenna was about 4dBi. However, after adding the (FSS) layer, it jumped into 15.6dBi but the overall height of the structure exceeded 5mm. The same remark can be made in [187], where the gain reached approximately 7dBi when the cavity was exited alone, but after arranging it as a 4*1 array the gain reached 12dBi, this array arrangement resulted in a bulky antennas with large dimensions such as [205], [206], [207].

All of the articles described in Table 4.1 above focus their works on improving the performance of the antenna based on additional modifications, such as integrating radiation elements above the slot, adopting an array arrangement, or adding an FSS superstrate resulting in a bulky structure that limits their utilization in practical applications. whereas the

proposed antenna design we focus on optimizing the slot's structure itself without additional modifications.

Table 4-1 Comparison of the proposed antenna and previous published designs

Reference	Frequency band	Technology	Peak gain (dBi) Before/after modification	BW (%) Before/after modification	Radiating elements	Dimensions (mm)	Antenna type
[192]	V	PRGW+FPC	≅4/15.6	16.8/20.4	1	22×18×5.5	slot
[195]	Ka	PRGW	≅/21.2	13.3/16.5	4x4	35×34×28	ME dipole
[187]	V	SIGW	≅7/12	11/33.3	4	25×27×0.76	Slot (array)
[208]	Ka	PRGW loaded with grooves	≅7/15.5	≅5/22	4	40 × 42 × 5.3	Slot (array)
[209]	Ka	PRGW	≅7/10.5	≅13/23.4	1	12× 12 × 2.7	ME dipole
[205]	Ka	PRGW+DP (SRR)	≅6/15	≅21/23	4	> 40×40×6	ME dipole
[210]	V	PRGW	≅4/9.1	>33/19.7	2	14× 15.7 × 0.76	slot
[211]	ka	Corporate RGW	9.8/21.2	21/10.4	4x4	56×48×1.3	MTS slot
[206]	ka	PRGW	NA/ 19.2	20.4/24	4x4	35.3×35.3×1.6	Strip-slot MTS
[207]	ka	SIW	21.9/20.4	9.64/18.9	4x4	63×48×5.47	ME dipole
[212]	W	GGW&RGW	NA/19.48	NA/12.8	4x4	20×20×7.7	Slot
Proposed works	**V**	**PRGW**	**9.5**	**11.5**	**1**	**13 × 19 × 0.76**	**Slot**
		D-PRGW	**16**	**33.3**	**1**	**8.6 × 7.5 × 1.27**	

Therefore, a remarkable improvement in the performance is achieved, where the proposed antenna has fairly reached a 33.3% relative BW with a high gain of about 16 dBi all over the operating frequency.

Conclusion

In the first part of this work, a numerical study of a miniaturization procedure was applied to an optimized version of the PRGW slot antenna that has reached a peak gain of 9.5 dBi and 11.5% BW among the V band.

This technique has proven the limitations of conventional antennas that adopted PRGW technology as a feeding mechanism in terms of gain and BW. It has also shown that in this type of structure good performance requires large dimensions along with several rows of EBG unit cells to operate coherently. These bulky structures will increase the complexity of the design as well as the cost of fabrication and won't be suitable for integration in low-scale devices.

Accordingly, in the second part, a new miniaturized design was proposed. This novel approach is based on the wide-band pure TEM D-PRGW technology in order to overcome the impairments of the previous PRGW systems with strictly minimum elements and compact overall size.

This novel approach is shown to deliver a wide BW of 33.3% ranging from 50 to 70 GHz with a high peak gain of 16 dBi and high efficiency (above 90%) all over the operating band.

GENERAL CONCLUSION

This thesis, titled "Contribution to the Design of New Antenna Structures More Efficient for 5G Communications Systems," has presented a comprehensive study of antenna technologies aimed at enhancing performance in the rapidly evolving 5G landscape.

There are many classical defies that are well-known in the deployment of 5G networks, such as infrastructure requirements, security vulnerabilities, high deployment costs and interoperability issues with existing networks. However, recently the limited availability of high-frequency spectrum became the major challenge that needs to be affronted. This is due mainly to the exponentially increasing seek for high-speed connectivity, support for massive machine-type communication and minimal latency.

The MMW band has been chosen as a fundamental choice for future 5G networks since it provides the capacity for reduced latency, significantly higher data rates and enhanced communication capabilities compared to lower frequency bands.

However, the high frequency signals in this band are more susceptible to impairments due to their shorter wavelength and increased sensitivity to atmospheric conditions, which can cause signal attenuation, sensitivity to environmental factors and degrade the overall performance. Moreover, as MMW antennas become smaller in size, the current flow density increases, leading to high conduction losses and reduced overall efficiency. All these characteristics necessitate innovative antenna designs capable of addressing the specific requirements of 5G communication systems.

The first part of this work gives an insight on new technologies of existing guiding techniques that address these frequency-dependent challenges and offer improved performance across a wider range of applications. In this context, recent technologies like SIW, RGW and PRGW were presented as the most promising guiding structures for higher frequency circuits and passive devices. Firstly, a detailed comprehension of how SIW and RGW technologies could potentially overcome the limitations faced by traditional transmission mechanisms is given, although they introduce new challenges such as significant losses and complex fabrication processes. Secondly, more interest was oriented specifically toward PRGW waveguides that became the focus of attention of the researchers as an alternative approach for MMW applications for several reasons including their reduced losses, large BW, quazi-TEM propagation and compact size. Each of the aforementioned technologies was evaluated in terms of its operational principles, advantages, and limitations. This overview highlighted the

transition from traditional designs to more compact and efficient structures, underscoring the necessity for tailored solutions in the MMW spectrum.

The first contribution to solve the aimed problematic is the use of DRAs technology taking advantage of its remarkable benefits namely, its outstanding performance characteristics and the use of dielectric materials, which makes such antennas cost-effective and able to achieve high gain and high radiation efficiency. After underlining the main features and advantages of DRAs and their evolving role in modern antenna systems, a miniaturized innovative metalized 2×1 bi-band Triangular DRA-based array along with a dual-beam forming capability was investigated for the Ka-band applications.

Herein, array technology was adopted to improve the channel capacity, which, however, would not provide sufficient operating BW to cover all users. To overcome this limitation the beam-forming technology is used to focus the signal into specified directions for better coverage and reliability. The miniaturization technique is achieved by cutting a rectangular DRA diagonally and applying a metallic strip at the top sidewall, providing a dual-band and dual-beam abilities at the same time, with a wide beam pointing angle (>30°).

The proposed TDRA effectively operates within two separate Ka-band frequencies, demonstrating symmetric radiation patterns at angles of ±28° for 28 GHz and ±31° for 33 GHz respectively. This design has achieved impressive performance metrics, including a peak gain of 8 dBi at 28 GHz and 6 dBi at 33 GHz, coupled with a stable radiation efficiency of approximately 90%. These results highlight the antenna's effectiveness in delivering high gain while maintaining excellent radiation performance, making it suitable for high-density urban environments typical of 5G deployments. The obtained results show that this novel design delivers high radiation efficiency and high gain at both operating frequencies with a large impedance BW.

Next, a state of the art on PRGW-based antenna techniques has shown that these latter need further research efforts to ensure efficient signal delivery to the radiation slot and improve the overall performance without introducing additional bulkiness. Therefore, an attempt has been made to improve PRGW-based antenna’s performance improving the PRGW performance without the assessment of any additional structures that would result in massive design. For this purpose, first of all the dimensions and placement of the slot were optimized to deliver the best performance in terms of BW, gain, and efficiency. Then, a miniaturization approach was applied by eliminating one row of EBG at a time from each side

of the ridge line while maintaining the same size and location of the radiating slot. The simulation results show the existence of a miniaturization limit that should not be exceeded to keep acceptable compromise between antenna size and performance efficiency, which imposes a serious constraint to further improvement of PRGW proposed antenna.

The second contribution is inspired from the novel D-PRGW technology that is as a wave-guiding structure operating in the Ka band, able to overcome the PRGW drawbacks. D-PRGW incorporates a double AMC textured surface in both the upper and lower layers, resulting in an asymmetrical structure featuring a dual ridge line on each side were the signal would be entirely confined with minimal fringing fields outside the ridge boundaries. Hence, a novel compact V-Band pure TEM D-PRGW slot antenna is proposed, simulated and realized. This latter utilizes double layer EBG lattice around the ridge area, effectively minimizing surface waves and confining the signal within the ridge. This proposed antenna achieved a wide impedance matching bandwidth of 33.3%, covering the frequency range from 50 to 70 GHz, thus accommodating significant portions of the unlicensed new radio (NR) bands (n262 and n263) of the V band. Furthermore, this design reached a peak gain of 16 dBi while maintaining an overall efficiency exceeding 90% across the operating band. The combination of high performance and compact size positions this antenna as an ideal candidate for 5G wireless communications centered around 60 GHz.

Finally, a comparative study, including the main performance criteria, showed clearly the superiority of the proposed antennas.

FUTURE WORK

While this research has contributed significantly to the field of antenna design for 5G applications, there are several avenues for future work that warrant exploration. First, the integration of advanced materials, such as metamaterials or graphene-based composites, could further enhance the performance characteristics of the TDRA and similar designs. These materials may provide improved bandwidth, gain, and thermal stability, potentially leading to even more compact and efficient antennas.

Second, expanding the frequency range of the proposed antennas to include lower bands could enhance their versatility for different applications, including sub-6 GHz communications. This would involve modifying the design parameters to achieve a balance between performance and operational range, addressing the need for multi-band antennas that can operate seamlessly across various frequency ranges.

Additionally, incorporating adaptive beamforming techniques and smart antenna technologies could enhance the directional capabilities and responsiveness of the antenna designs. This would enable dynamic adjustments in radiation patterns, improving signal quality and coverage in real-time based on user demand and environmental conditions.

Moreover, experimental validation of the proposed designs in real-world scenarios is essential to assess their performance under various operational conditions. This could include extensive field testing to evaluate factors such as interference, multipath propagation, and the effects of urban environments on antenna performance.

Finally, collaboration with industry partners for prototype development and testing could provide valuable insights into practical deployment challenges and requirements. Engaging in such partnerships may lead to the refinement of antenna designs to better meet the commercial needs of 5G network providers.

In conclusion, this thesis has laid the groundwork for the development of advanced antenna structures tailored for 5G communications, addressing both theoretical and practical aspects of design. The findings and innovations presented herein have the potential to significantly contribute to the ongoing evolution of wireless communication systems, ensuring robust and efficient connectivity in an increasingly interconnected world.

References

[1] STÜBER, Gordon L. *Digital Modulation and Power Spectrum. Principles of Mobile Communication*, 2012, p. 189-269.

[2] SARKAR, Tapan K., WICKS, Michael C., SALAZAR-PALMA, Magdalena, et al. *Smart antennas*. John Wiley & Sons, 2005.

[3] SARKAR, Tapan K., MAILLOUX, Robert, OLINER, Arthur A., *et al. History of wireless*. John Wiley & Sons, 2006.

[4] RAPPAPORT, Theodore S., SUN, Shu, MAYZUS, Rimma, et al. *Millimeter wave mobile communications for 5G cellular: It will work!*. IEEE access, 2013, vol. 1, p. 335-349.

[5] DAHLMAN, Erik, PARKVALL, Stefan, et SKOLD, Johan. 4G: *LTE/LTE-advanced for mobile broadband*. Academic press, 2013.

[6] ATTARAN, Mohsen. *The impact of 5G on the evolution of intelligent automation and industry digitization. Journal of ambient intelligence and humanized comp*uting, 2023, vol. 14, no 5, p. 5977-5993.

[7] IVANOVA, E. P., ILIEV, T. B., STOYANOV, I. S., et al. *Evolution of mobile networks and seamless transition to 5G*. In : IOP Conference Series: Materials Science and Engineering. IOP Publishing, 2021. p. 012008.

[8] CHANDRA, Kishor, PRASAD, R. Venkatesha, QUANG, Bien, et al. *CogCell: cognitive interplay between 60 GHz picocells and 2.4/5 GHz hotspots in the 5G era*. IEEE Communications Magazine, 2015, vol. 53, no 7, p. 118-125.

[9] GHOSH, Amitava, THOMAS, Timothy A., CUDAK, Mark C., et al. *Millimeter-wave enhanced local area systems: A high-data-rate approach for future wireless networks*. IEEE Journal on Selected Areas in Communications, 2014, vol. 32, no 6, p. 1152-1163.

[10] PIRINEN, Pekka. *A brief overview of 5G research activities*. In : 1st International Conference on 5G for Ubiquitous Connectivity. IEEE, 2014. p. 17-22.

[11] M. Fallgren, B. Timus, et al., *Scenarios, Requirements and KPIs for 5G Mobile and Wireless System*, METIS deliverable D, vol. 1, p. 1, 2013.

[12] DU PREEZ, Jaco et SINHA, Saurabh. *Millimeter-wave antennas: configurations and applications*. springer, 2016.

[13] HUANG, Kao-Cheng et EDWARDS, David J. *Millimetre wave antennas for gigabit wireless communications: a practical guide to design and analysis in a system context*. John Wiley & Sons, 2008.

[14] Moody, J., Lepkowski, S., & Forbes, T. (2023). *A mmW Receiver Exploiting Complementary Current Reuse and Power Efficient Bias Point*. IEEE Transactions on Microwave Theory and Techniques.

[15] BHARTIA, Prakash et BAHL, Inder Jit. *Millimeter wave engineering and applications*. 1984.

[16] RUSEK, Fredrik, PERSSON, Daniel, LAU, Buon Kiong, et al. *Scaling up MIMO: Opportunities and challenges with very large arrays*. IEEE signal processing magazine, 2012, vol. 30, no 1, p. 40-60.

[17] NIU, Yong, LI, Yong, JIN, Depeng, et al. *A survey of millimeter wave communications (mmWave) for 5G: opportunities and challenges*. Wireless networks, 2015, vol. 21, p. 2657-2676.

[18] WELLS, Jonathan. *Multi-gigabit microwave and millimeter-wave wireless communications*. Artech House, 2010.

[19] ALTSHULER, EDWARD E. et MARR, RICHARD A. *A comparison of experimental and theoretical values of atmospheric absorption at the longer millimeter wavelengths*. IEEE transactions on antennas and propagation, 1988, vol. 36, no 10, p. 1471-1480.

[20] WELLS, Jonathan. *Faster than fiber: The future of multi-G/s wireless.* IEEE microwave magazine, 2009, vol. 10, no 3, p. 104-112.

[21] MARCUS, Michael et PATTAN, Bruno. *Millimeter wave propagation: spectrum management implications.* IEEE Microwave Magazine, 2005, vol. 6, no 2, p. 54-62.

[22] LI, Xiaogang, YU, Li, ZHANG, Yuxiang, et al. *Diffraction characteristics aided blockage and beam prediction for mmWave communications.* In : 2022 IEEE 95th Vehicular Technology Conference:(VTC2022-Spring). IEEE, 2022. p. 1-5.

[23] MANNING, Trevor. *Microwave radio transmission design guide*. Artech house, 2009.

[24] PIERSANTI, Stefano, ANNONI, Luca Alfredo, et CASSIOLI, Dajana. *Millimeter waves channel measurements and path loss models*. In : 2012 IEEE International Conference on Communications (ICC). IEEE, 2012. p. 4552-4556.

[25] MATIN, Mohammad A. *Review on millimeter wave antennas-potential candidate for 5G enabled applications*. Advanced Electromagnetics, 2016, vol. 5, no 3, p. 98-105.

[26] WANG, Cheng-Xiang, HAIDER, Fourat, GAO, Xiqi, et al. *Cellular architecture and key technologies for 5G wireless communication networks*. IEEE communications magazine, 2014, vol. 52, no 2, p. 122-130.

[27] APPLEBY, Roger, ROBERTSON, Duncan A., et WIKNER, David. *Millimeter wave imaging: a historical review*. In : Passive and Active Millimeter-Wave Imaging XX. SPIE, 2017. p. 1018902.

[28] 5G Observatory Biannual Report Report of June 2024(Situation as of 31 March2024)Study on European 5G Observatory phase III (CNECT/2021/OP/0008).

[29] BRUDER, J., CARLO, J., GURNEY, J., et al. *IEEE standard for letter designations for radar-frequency bands*. IEEE Aerospace & Electronic Systems Society, 2003, p. 1-3.

[30] NAKAMURA, Takehiro, BENJEBBOUR, Anass, KISHIYAMA, Yoshihisa, et al. *5G radio access: Requirements, concept and experimental trials*. IEICE Transactions on Communications, 2015, vol. 98, no 8, p. 1397-1406.

[31] SRIDHAR, Varadharajan et SRIDHAR, V. *Spectrum regulation: case of V-band*. Emerging ICT Policies and Regulations: Roadmap to Digital Economies, 2019, p. 59-78.

[32] SEYEDI, Alireza. *On the physical layer performance of Ecma-387: A standard for 60GHz WPANs*. In : *2009 IEEE International Conference on Ultra-Wideband*. IEEE, 2009. p. 28-32.

[33] BAYKAS, Tuncer, SUM, Chin-Sean, LAN, Zhou, et al. *IEEE 802.15. 3c: The first IEEE wireless standard for data rates over 1 Gb/s*. IEEE Communications Magazine, 2011, vol. 49, no 7, p. 114-121.

[34] ANASTASI, Giuseppe, BORGIA, Eleonora, CONTI, Marco, et al. *IEEE 802.11 ad hoc networks: performance measurements*. In : 23rd International Conference on Distributed Computing Systems Workshops, 2003. Proceedings. IEEE, 2003. p. 758-763.

[35] YILMAZ, Turker et AKAN, Ozgur B. *On the use of low terahertz band for 5G indoor mobile networks*. Computers & Electrical Engineering, 2015, vol. 48, p. 164-173.

[36] SAKAGUCHI, Kei, HAUSTEIN, Thomas, BARBAROSSA, Sergio, et al. *Where, when, and how mmWave is used in 5G and beyond*. IEICE Transactions on Electronics, 2017, vol. 100, no 10, p. 790-808.

[37] MATTISSON, Sven. *Overview of 5G requirements and future wireless networks*. In : ESSCIRC 2017-43rd IEEE European Solid State Circuits Conference. IEEE, 2017. p. 1-6.

[38] WANG, Dian et CHAN, Chi Hou. *Multiband antenna for WiFi and WiGig communications*. IEEE antennas and wireless propagation letters, 2015, vol. 15, p. 309-312.

[39] ETTORRE, Mauro, SAULEAU, Ronan, LE COQ, Laurent, et al. *Single-folded leaky-wave antennas for automotive radars at 77 GHz*. IEEE Antennas and Wireless Propagation Letters, 2010, vol. 9, p. 859-862.

[40] AGARWAL, Smriti, PATHAK, Nagendra P., et SINGH, Dharmendra. *Performance comparison of microstrip patch antenna for 94 GHz imaging applications.* In : 2012 IEEE 7th International Conference on Industrial and Information Systems (ICIIS). IEEE, 2012. p. 1-4.

[41] JILANI, Syeda Fizzah, ABBASI, Qammer H., et ALOMAINY, Akram. *Inkjet-printed millimetre-wave PET-based flexible antenna for 5G wireless applications.* In : 2018 IEEE MTT-S International Microwave Workshop Series on 5G Hardware and System Technologies (IMWS-5G). IEEE, 2018. p. 1-3.

[42] MATOS, Sérgio A., LIMA, Eduardo B., COSTA, Jorge R., et al. *Design of a 40 dBi planar bifocal lens for mechanical beam steering at Ka-band*. In : 2016 10th European Conference on Antennas and Propagation (EuCAP). IEEE, 2016. p. 1-4.

[43] RAMANUJAM, Parthasarathy, PONNUSAMY, Manimaran, et RAMANUJAM, Krishnamurthy. *A compact wide-bandwidth Antipodal Vivaldi Antenna array with suppressed mutual coupling for 5G mm-wave applications.* AEU-International Journal of Electronics and Communications, 2021, vol. 133, p. 153668.

[44] ELFERGANI, Issa, RODRIGUEZ, Jonathan, IQBAL, Amjad, et al. *Compact millimeter-wave MIMO antenna for 5G applications.* In : 2020 14th European Conference on Antennas and Propagation (EuCAP). IEEE, 2020. p. 1-5.

[45] TAFAZOLLI, Rahim, WANG, Chin-Liang, et CHATZIMISIOS, Periklis. *Wiley 5G Ref: the essential 5G reference online*. Wiley, 2019.

[46] HASAN, Md Nazmul, BASHIR, Shahid, et CHU, Son. *Dual band omnidirectional millimeter wave antenna for 5G communications.* Journal of Electromagnetic Waves and Applications, 2019, vol. 33, no 12, p. 1581-1590.

[47] HONG, Tao, ZHENG, Shuli, LIU, Rongke, et al. *Design of mmWave directional antenna for enhanced 5G broadcasting coverage*. Sensors, 2021, vol. 21, no 3, p. 746.

[48] PRASAD, S., MEENAKSHI, M., ADHITHIYA, N., et al. *mmWave multibeam phased array antenna for 5G applications.* Journal of Electromagnetic Waves and Applications, 2021, vol. 35, no 13, p. 1802-1814.

[49] LI, Ao et LUK, Kwai-Man. *Millimeter-wave dual linearly polarized endfire antenna fed by 180° hybrid coupler.* IEEE Antennas and Wireless Propagation Letters, 2019, vol. 18, no 7, p. 1390-1394.

[50] LI, Mingjian et LUK, Kwai-Man. *A wideband circularly polarized antenna for microwave and millimeter-wave applications.* IEEE Transactions on Antennas and Propagation, 2014, vol. 62, no 4, p. 1872-1879.

[51] TAN, Wenhao, XIAO, Yu, LI, Cong, et al. *A wide-band high-efficiency hybrid-feed antenna array for mm-wave wireless systems.* Electronics, 2021, vol. 10, no 19, p. 2383.

[52] WENGER, Josef. *Short range radar-being on the market*. In : 2007 European Radar Conference. IEEE, 2007. p. 255-258.

[53] HANSEN, Christopher J. WiGiG: *Multi-gigabit wireless communications in the 60 GHz band*. IEEE Wireless Communications, 2011, vol. 18, no 6, p. 6-7.

[54] UWAECHIA, Anthony Ngozichukwuka et MAHYUDDIN, Nor Muzlifah. *A comprehensive survey on millimeter wave communications for fifth-generation wireless networks: Feasibility and challenges. IEEE Access*, 2020, vol. 8, p. 62367-62414.

[55] D. Pozar, *Microwave Engineering*, 4th Edition, John Wiley & Sons, 2011.

[56] MESA, F., OLINER, A. A., JACKSON, D. R., et al. *The influence of a top cover on the leakage from microstrip line*. IEEE Transactions on Microwave Theory and Techniques, 2000, vol. 48, no 12, p. 2240-2248.

[57] KHODJA, Khalida, BELAZZOUG, Massinisssa, ATIA, Salim, *et al. Dual-beam DRA based array for 5G applications*. In : *2021 IEEE 19th International Symposium on Antenna Technology and Applied Electromagnetics (ANTEM)*. IEEE, 2021. p. 1-2.

[58] KHODJA, K., ATIA, S., MESSAOUDENE, I., et al. *Novel High Efficiency V-Band Pure TEM D-PRGW Antenna for 5G mmWave Applications*. International Journal of Communication Systems, 2024, p. e6008.

[59] LEVINE, Ely, MALAMUD, Gabi, SHTRIKMAN, Shmuel, et al. *A study of microstrip array antennas with the feed network.* IEEE Transactions on Antennas and Propagation, 1989, vol. 37, no 4, p. 426-434.

[60] M. Tsuji, H. Shigesawa, and A.A. Oliner, *Simultaneous Propagation of bound and leaky dominant modes on printed-circuit lines*, IEEE Trans. Microw. Theory and Tech., vol. 43, no. 12, pp. 3007-3019, Dec. 1995.

[61] MCKINZIE, William E. et ALEXOPOULOS, Nicolaos G. *Leakage losses for the dominant mode of conductor-backed coplanar waveguide*. IEEE microwave and guided wave letters, 1992, vol. 2, no 2, p. 65-66.

[62] OMAR, Amjad A. et CHOW, Y. Leonard. *A solution of coplanar waveguide with air-bridges using complex images*. IEEE transactions on microwave theory and techniques, 1992, vol. 40, no 11, p. 2070-2077

[63] SAIN, Arghya et MELDE, Kathleen L. *Impact of ground via placement in grounded coplanar waveguide interconnects*. IEEE Transactions on Components, Packaging and Manufacturing Technology, 2015, vol. 6, no 1, p. 136-144.

[64] SIMONS, Rainee N. *Coplanar waveguide circuits, components, and systems*. John Wiley & Sons, 2004.

[65] ROBINSON, Martin Paul, TURNER, J. D., THOMAS, David WP, et al. *Shielding effectiveness of a rectangular enclosure with a rectangular aperture*. Electronics Letters, 1996, vol. 32, no 17, p. 1559-1560.

[66] MAHMOUD, Samir F. *Electromagnetic waveguides: theory and applications*. IET, 1991.

[67] YONEYAMA, Tsukasa et NISHIDA, Shigeo. *Nonradiative dielectric waveguide for millimeter-wave integrated circuits*. IEEE transactions on Microwave Theory and Techniques, 1981, vol. 29, no 11, p. 1188-1192.

[68] Yoneyama, T., Fujita, S., & Nishida, S. (1983). *Insulated nonradiative dielectric waveguide for millimeter-wave integrated circuits.* IEEE transactions on microwave theory and techniques, 31(12), 1002-1008.

[69] LINDELL, Ismo V. *Image theory for the general isotropic ideal boundary*. Microwave and Optical Technology Letters, 2000, vol. 27, no 1, p. 68-72.

[70] LINDELL, Ismo V. *Ideal boundary and generalised soft and hard conditions*. IEE Proceedings-Microwaves, Antennas and Propagation, 2000, vol. 147, no 6, p. 495-499.

[71] LINDELL, Ismo V. *Condition for the general ideal boundary*. Microwave and Optical Technology Letters, 2000, vol. 26, no 1, p. 61-64.

[72] CUTLER, Cassius Chapin. *Electromagnetic waves guided by corrugated conducting surfaces*. 1944.

[73] KILDAL, P.-S. *Definition of artificially soft and hard surfaces for electromagnetic waves.* Electronics Letters, 1988, vol. 24, p. 168-170.

[74] KISHK, A. A. et KILDAL, P.-S. *Modelling of soft and hard surfaces using ideal perfect electric conducting/perfect magnetic conducting strip grids.* IET Microwaves, Antennas & Propagation, 2009, vol. 3, no 2, p. 296-302.

[75] KILDAL, Per-Simon et KISHK, Ahmed. *EM modeling of surfaces with STOP or GO characteristics–artificial magnetic conductors and soft and hard surfaces.* The Applied Computational Electromagnetics Society Journal (ACES), 2003, p. 32-40.

[76] ENGHETA, Nader et ZIOLKOWSKI, Richard W. (ed.). *Metamaterials: physics and engineering explorations*. John Wiley & Sons, 2006.

[77] KILDAL, Per-Simon, et al. *Artificially soft and hard surfaces in electromagnetics*. IEEE Transactions on Antennas and Propagation, 1990, vol. 38, no 10, p. 1537-1544.

[78] VALERO-NOGUEIRA, Alejandro, ALFONSO, Esperanza, HERRANZ, Jose I., et al. *Experimental demonstration of local quasi-TEM gap modes in single-hard-wall waveguides.* IEEE Microwave and Wireless Components Letters, 2009, vol. 19, no 9, p. 536-538.

[79] KILDAL, P.-S. et LIER, E. *Hard horns improve cluster feeds of satellite antennas*. Electronics Letters, 1988, vol. 24, p. 491.

[80] KEHN, M. Ng Mou et KILDAL, P.-S. *Miniaturized rectangular hard waveguides for use in multifrequency phased arrays*. IEEE Transactions on Antennas and Propagation, 2005, vol. 53, no 1, p. 100-109.

[81] LIER, Erik et KILDAL, P.-S. *Soft and hard horn antennas*. IEEE Transactions on Antennas and Propagation, 1988, vol. 36, no 8, p. 1152-1157.

[82] RAHMAT-SAMII, Yahya et MOSALLAEI, H. *Electromagnetic band-gap structures: classification, characterization, and applications*. 2001.

[83] RAJO-IGLESIAS, Eva et KILDAL, P.-S. *Numerical studies of bandwidth of parallel-plate cut-off realised by a bed of nails, corrugations and mushroom-type electromagnetic bandgap for use in gap waveguides.* IET microwaves, antennas & propagation, 2011, vol. 5, no 3, p. 282-289.

[84] RAJO-IGLESIAS, Eva, ZAMAN, Ashraf Uz, et KILDAL, Per-Simon. *Parallel plate cavity mode suppression in microstrip circuit packages using a lid of nails.* IEEE Microwave and Wireless Components Letters, 2009, vol. 20, no 1, p. 31-33.

[85] RAJO-IGLESIAS, Eva, PUCCI, Elena, KISHK, Ahmed A., et al. *Suppression of parallel plate modes in low frequency microstrip circuit packages using lid of printed zigzag wires*. IEEE microwave and wireless components letters, 2013, vol. 23, no 7, p. 359-361.

[86] PENDRY, John B., HOLDEN, A. J., STEWART, W. J., et al. *Extremely low frequency plasmons in metallic mesostructures*. Physical review letters, 1996, vol. 76, no 25, p. 4773.

[87] BELOV, Pavel A., MARQUES, R., MASLOVSKI, Stanislav I., et al. *Strong spatial dispersion in wire media in the very large wavelength limit.* Physical Review B, 2003, vol. 67, no 11, p. 113103.

[88] SILVEIRINHA, Mário G., FERNANDES, Carlos A., et COSTA, Jorge R. *Electromagnetic characterization of textured surfaces formed by metallic pins*. IEEE Transactions on Antennas and Propagation, 2008, vol. 56, no 2, p. 405-415.

[89] POLEMI, Alessia, MACI, Stefano, et KILDAL, Per-Simon. *Dispersion characteristics of a metamaterial-based parallel-plate ridge gap waveguide realized by bed of nails.* IEEE Transactions on Antennas and Propagation, 2010, vol. 59, no 3, p. 904-913.

[90] BELOV, Pavel A., MARQUES, R., MASLOVSKI, Stanislav I., et al. *Strong spatial dispersion in wire media in the very large wavelength limit*. Physical Review B, 2003, vol. 67, no 11, p. 113103..

[91] KILDAL, Per-Simon, ALFONSO, E., VALERO-NOGUEIRA, A., et al. *Local metamaterial-based waveguides in gaps between parallel metal plates*. IEEE Antennas and wireless propagation letters, 2008, vol. 8, p. 84-87.

[92] HILL, Michael J., ZIOLKOWSKI, Richard W., et PAPAPOLYMEROU, John. *A high-Q reconfigurable planar EBG cavity resonator*. IEEE Microwave and Wireless Components Letters, 2001, vol. 11, no 6, p. 255-257.

[93] CASSIVI, Yves, PERREGRINI, Luca, WU, Ke, et al. *Low-cost and high-Q millimeter-wave resonator using substrate integrated waveguide technique.* In : 2002 32nd European Microwave Conference. IEEE, 2002. p. 1-4.

[94] CHEN, Anqi, MOUSA, Al-Juboori Bahaa Jasim, ZHUANG, Yuan, et al. *Compact Ka-band substrate-integrated waveguide filter with spurlines for satellite communication systems.* In : 2016 IEEE 9th UK-Europe-China Workshop on Millimetre Waves and Terahertz Technologies (UCMMT). IEEE, 2016. p. 10-11.

[95] JUNG, Eun-Young, LEE, Jae W., LEE, Taek K., et al. *SIW-based array antennas with sequential feeding for X-band satellite communication.* IEEE Transactions on Antennas and Propagation, 2012, vol. 60, no 8, p. 3632-3639.

[96] OZTURK, Alper K. et PAKNYS, Robert. *Analysis of propagation between rows of conducting cylinders that model solid surfaces using the same surface area rule*. IEEE transactions on antennas and propagation, 2012, vol. 60, no 5, p. 2602-2606.

[97] DESLANDES, Dominic et WU, Ke. *Design consideration and performance analysis of substrate integrated waveguide components.* In : 2002 32nd European microwave conference. IEEE, 2002. p. 1-4.

[98] IQBAL, Amjad, TIANG, Jun Jiat, WONG, Sew Kin, et al. *Miniaturization trends in substrate integrated waveguide (SIW) filters: A review*. IEEE access, 2020, vol. 8, p. 223287-223305.

[99] RANJKESH, N. et SHAHABADI, M. *Reduction of dielectric losses in substrate integrated waveguide*. Electronics Letters, 2006, vol. 42, no 21, p. 1230-1232.

[100] BELENGUER, Angel, ESTEBAN, Hector, et BORIA, Vicente E. *Novel empty substrate integrated waveguide for high-performance microwave integrated circuits*. IEEE transactions on microwave theory and techniques, 2014, vol. 62, no 4, p. 832-839.

[101] PARMENT, Frédéric, GHIOTTO, Anthony, VUONG, Tan-Phu, et al. *Double dielectric slab-loaded air-filled SIW phase shifters for high-performance millimeter-wave integration*. IEEE Transactions on Microwave Theory and Techniques, 2016, vol. 64, no 9, p. 2833-2842.

[102] GHIOTTO, Anthony, PARMENT, Frédéric, VUONG, Tan-Phu, et al. *Multilayer-substrate integration technique of air-filled waveguide circuits*. In : 2016 IEEE MTT-S International Conference on Numerical Electromagnetic and Multiphysics Modeling and Optimization (NEMO). IEEE, 2016. p. 1-3.

[103] PARMENT, Frédéric, GHIOTTO, Anthony, VUONG, Tan-Phu, et al. *Air-filled substrate integrated waveguide for low-loss and high power-handling millimeter-wave substrate integrated circuits.* IEEE transactions on microwave theory and techniques, 2015, vol. 63, no 4, p. 1228-1238.

[104] KILDAL, Per-Simon. *Three metamaterial-based gap waveguides between parallel metal plates for mm/submm waves.* In : 2009 3rd European Conference on Antennas and Propagation. IEEE, 2009. p. 28-32.

[105] MANTASH, Mohamad, TAROT, Anne-Claude, COLLARDEY, Sylvain, et al. *Novel dual-band hexagonal EBG structure*. In : META'12. 2012.

[106] KIM, Myunghoi et KAM, Dong Gun. *A wideband and compact EBG structure with a circular defected ground structure.* IEEE Transactions on Components, Packaging and Manufacturing Technology, 2013, vol. 4, no 3, p. 496-503.

[107] P. Kildal, *Waveguides and transmission lines in gaps between parallel conducting surfaces.* US Patent 2011/0181373 A1, 28 July 2011.

[108] LEE, Young Ju, YEO, Junho, MITTRA, Raj, et al. *Application of electromagnetic bandgap (EBG) superstrates with controllable defects for a class of patch antennas as spatial angular filters*. IEEE Transactions on Antennas and Propagation, 2005, vol. 53, no 1, p. 224-235.

[109] MAO, Shau-Gang et CHEN, Ming-Yi. *Propagation characteristics of finite-width conductor-backed coplanar waveguides with periodic electromagnetic bandgap cells*. IEEE transactions on Microwave Theory and Techniques, 2002, vol. 50, no 11, p. 2624-2628.

[110] YANG, Fan et RAHMAT-SAMII, Yahya. *Reflection phase characterizations of the EBG ground plane for low profile wire antenna applications.* IEEE Transactions on antennas and propagation, 2003, vol. 51, no 10, p. 2691-2703

[111] PUCCI, Elena, RAJO-IGLESIAS, Eva, et KILDAL, Per-Simon. *New microstrip gap waveguide on mushroom-type EBG for packaging of microwave components.* IEEE Microwave and Wireless Components Letters, 2012, vol. 22, no 3, p. 129-131.

[112] RAZA, Hasan, YANG, Jian, KILDAL, Per-Simon, et al. *Microstrip-ridge gap waveguide–study of losses, bends, and transition to WR-15*. IEEE transactions on microwave theory and techniques, 2014, vol. 62, no 9, p. 1943-1952.

[113] SORKHERIZI, Milad Sharifi et KISHK, Ahmed A. *Transition from microstrip to printed ridge gap waveguide for millimeter-wave application.* In : 2015 IEEE International Symposium on Antennas and Propagation & USNC/URSI National Radio Science Meeting. IEEE, 2015. p. 1588-1589.

[114] SORKHERIZI, Milad Sharifi et KISHK, Ahmed A. *Fully printed gap waveguide with facilitated design properties.* IEEE Microwave and Wireless Components Letters, 2016, vol. 26, no 9, p. 657-659.

[115] JIANG, Xun, JIA, Fangxiu, CAO, Yang, *et al. Ka-band 8× 8 low-sidelobe slot antenna array using a 1-to-64 high-efficiency network designed by new printed RGW*

technology. IEEE Antennas and Wireless Propagation Letters, 2019, vol. 18, no 6, p. 1248-1252.

[116] WANG, Li-Feng, XUE, Shou-Bin, MAO, Zhong-Yang, et al. *Compact dual-band inverted-microstrip ridge gap waveguide diplexer.* International Journal of RF and Microwave Computer-Aided Engineering, 2021, vol. 31, no 10, p. e22829.

[117] ALI, Mohamed Mamdouh M., SHAMS, Shoukry I., et SEBAK, Abdel-Razik. *Printed ridge gap waveguide 3-dB coupler: Analysis and design procedure*. IEEE Access, 2017, vol. 6, p. 8501-8509.

[118] POLEMI, Alessia et MACI, S. *Closed form expressions for the modal dispersion equations and for the characteristic impedance of a metamaterial-based gap waveguide*. IET microwaves, antennas & propagation, 2010, vol. 4, no 8, p. 1073-1080.

[119] ZAMAN, Ashraf Uz, KILDAL, Per-Simon, FERNDAHL, Mattias, et al. *Validation of ridge gap waveguide performance using in-house TRL calibration kit*. In : Proceedings of the Fourth European Conference on Antennas and Propagation. IEEE, 2010. p. 1-4.

[120] VALERO-NOGUEIRA, Alejandro, BAQUERO, Mariano, HERRANZ, Jose I., et al. *Gap waveguides using a suspended strip on a bed of nails*. IEEE Antennas and Wireless Propagation Letters, 2011, vol. 10, p. 1006-1009.

[121] SHAMS, Shoukry I. et KISHK, Ahmed A. *Printed texture with triangle flat pins for bandwidth enhancement of the ridge gap waveguide*. IEEE Transactions on Microwave Theory and Techniques, 2017, vol. 65, no 6, p. 2093-2100.

[122] HELSZAJN, Joseph. *Ridge waveguides and passive microwave components*. Iet, 2000.

[123] SHAMS, Shoukry I. et KISHK, Ahmed A. *Printed texture with triangle flat pins for bandwidth enhancement of the ridge gap waveguide*. IEEE Transactions on Microwave Theory and Techniques, 2017, vol. 65, no 6, p. 2093-2100.

[124] RAJO-IGLESIAS, Eva et KILDAL, P.-S. *Numerical studies of bandwidth of parallel-plate cut-off realised by a bed of nails, corrugations and mushroom-type electromagnetic bandgap for use in gap waveguides.* IET microwaves, antennas & propagation, 2011, vol. 5, no 3, p. 282-289.

[125] HIROKAWA, Jiro et ANDO, Makoto. *Single-layer feed waveguide consisting of posts for plane TEM wave excitation in parallel plates*. IEEE Transactions on Antennas and Propagation, 1998, vol. 46, no 5, p. 625-630.

[126] RAJO-IGLESIAS, Eva et KILDAL, Per-Simon. *Groove gap waveguide: A rectangular waveguide between contactless metal plates enabled by parallel-plate cut-off*. In

: Proceedings of the Fourth European Conference on Antennas and Propagation. IEEE, 2010. p. 1-4.

[127] SHATERIAN, Zahra, HORESTANI, Ali K., et RASHED-MOHASSEL, Jalil. *Design of slot array antenna in groove gap waveguide technology*. *IET Microwaves, Antennas & Propagation*, 2019, vol. 13, no 8, p. 1235-1239.

[128] Berenguer, A., Fusco, V., Zelenchuk, D. E., Sanchez-Escuderos, D., Baquero-Escudero, M., & Boria-Esbert, V. E. (2016). *Propagation Characteristics of Groove Gap Waveguide Below and Above Cutoff*. IEEE Transactions on Microwave Theory and Techniques

[129] Pucci, E., Zaman, A. U., Rajo-Iglesias, E., Kildal, P. S., & Kishk, A. (2013). *Study of Q-factors of ridge and groove gap waveguide resonators.* IET Microwaves, Antennas & Propagation, 7(11), 900-908

[130] NASRI, Marzie et ZARIFI, Davoud. *A broadband gap waveguide-based magic-T junction for millimeter-wave applications*. Journal of Infrared, Millimeter, and Terahertz Waves, 2021, vol. 42, no 7, p. 793-801

[131] BALANIS, Constantine A. *Antenna theory: analysis and design*. John wiley & sons, 2016.

[132] BOSILJEVAC, Marko, POLEMI, A., MACI, Stefano, et al. *Analytic approach to the analysis of ridge and groove gap waveguides-comparison of two methods*. In : Proceedings of the 5th European Conference on Antennas and Propagation (EUCAP). IEEE, 2011. p. 1886-1889.

[133] RAJO-IGLESIAS, Eva et KILDAL, Per-Simon. *Groove gap waveguide: A rectangular waveguide between contactless metal plates enabled by parallel-plate cut-off*. In : Proceedings of the Fourth European Conference on Antennas and Propagation. IEEE, 2010. p. 1-4.

[134] BRAZALEZ, Astrid Algaba, RAJO-IGLESIAS, Eva, VAZQUEZ-ROY, Jose Luis, et al. *Design and validation of microstrip gap waveguides and their transitions to rectangular waveguide, for millimeter-wave applications*. IEEE Transactions on Microwave Theory and Techniques, 2015, vol. 63, no 12, p. 4035-4050.

[135] KISHK, Ahmed, ZAMAN, Ashraf Uz, et KILDAL, Per-Simon. *Numerical prepackaging with PMC lid-Efficient and simple design procedure for microstrip circuits including the packaging*. The Applied Computational Electromagnetics Society Journal (ACES), 2012, p. 389-398.

[136] ZHANG, Jing, ZHANG, Xiupu, SHEN, Dongya, et al. *Packaged microstrip line: A new quasi-TEM line for microwave and millimeter-wave applications.* IEEE Transactions on Microwave Theory and Techniques, 2016, vol. 65, no 3, p. 707-719.

[137] CASTRO, Nelson, PIZARRO, Francisco, HERRÁN-ONTANÓN, Luis Fernando, et al. *Evaluation of inverted microstrip gap waveguide bandpass filters for Ka-band.* AEU-International Journal of Electronics and Communications, 2021, vol. 134, p. 153677.

[138] PUCCI, Elena, RAJO-IGLESIAS, Eva, VAZQUEZ-ROY, Jose-Luis, et al. *Planar dual-mode horn array with corporate-feed network in inverted microstrip gap waveguide*. IEEE Transactions on Antennas and Propagation, 2014, vol. 62, no 7, p. 3534-3542

[139] HEMADEH, Ibrahim A., SATYANARAYANA, Katla, EL-HAJJAR, Mohammed, et al. *Millimeter-wave communications: Physical channel models, design considerations, antenna constructions, and link-budget*. IEEE Communications Surveys & Tutorials, 2017, vol. 20, no 2, p. 870-913.

[140] PETOSA, Aldo. *Dielectric resonator antenna handbook*. Artech, 2007.

[141] ZHANG, Xiu-Yin, XUE, Di, YE, Liang-Hua, et al. *Compact dual-band dual-polarized interleaved two-beam array with stable radiation pattern based on filtering elements.* IEEE transactions on antennas and propagation, 2017, vol. 65, no 9, p. 4566-4575.

[142] KUMAR, Pramod, DWARI, Santanu, MANDAL, Mrinal Kanti, et al. *Electronically controlled beam steerable dual-band star-shaped DRA for UAS and Wi-Fi data link applications.* IEEE Transactions on Antennas and Propagation, 2020, vol. 68, no 10, p. 7214-7218.

[143] SHARAWI, Mohammad S., PODILCHAK, Symon K., KHAN, Muhammad U., et al. *Dual-frequency DRA-based MIMO antenna system for wireless access points*. IET Microwaves, Antennas & Propagation, 2017, vol. 11, no 8, p. 1174-1182.

[144] KLIONOVSKI, Kirill, SHAMIM, Atif, et SHARAWI, Mohammad Said. *5G antenna array with wide-angle beam steering and dual linear polarizations*. In : 2017 IEEE International Symposium on Antennas and Propagation & USNC/URSI National Radio Science Meeting. IEEE, 2017. p. 1469-1470.

[145] RODAHL, Michael, HÖÖK, Fredrik, KROZER, Anatol, et al. *Quartz crystal microbalance setup for frequency and Q-factor measurements in gaseous and liquid environments*. Review of Scientific Instruments, 1995, vol. 66, no 7, p. 3924-3930.

[146] PETOSA, A. M. M. A., ITTIPIBOON, Apisak, ANTAR, Y. M. M., et al. *Recent advances in dielectric-resonator antenna technology*. IEEE Antennas and Propagation magazine, 1998, vol. 40, no 3, p. 35-48.

[147] ZHANG, Yingqi, OGURTSOV, Stanislav, VASILEV, Vasilii, et al. *Advanced Dielectric Resonator Antenna Technology for 5G and 6G Applications. Sensors*, 2024, vol. 24, no 5, p. 1413.

[148] LEUNG, Kowk Wa, LONG, Stuart A., et LUK, K. M. *Overview of the dielectric resonator antenna*. Dielectric Resonator Antennas, 2003, vol. 1.

[149] SAHOO, Madhusmita, PATANI, Aswin, et MAKWANA, Balvant. *A review on Di-electrical resonant antenna based on the performance of gain and bandwidth.* Multimedia Tools and Applications, 2023, vol. 82, no 16, p. 24645-24679.

[150] SHEHBAZ, Muhammad, DU, Chao, ZHOU, Di, et al. *Recent progress in dielectric resonator antenna: Materials, designs, fabrications, and their performance*. Applied Physics Reviews, 2023, vol. 10, no 2.

[151] HARKARE, Ankita H., KOTHARI, Ashwin G., et BHURANE, Ankit A. *Evolution of gain enhancement techniques in dielectric resonator antenna: applications and challenges.* International Journal of Microwave and Wireless Technologies, 2023, vol. 15, no 5, p. 891-905.

[152] MCKIMPSON, Marvin G., POHLENZ, Eric L., et THOMPSON, Steven R. *Evaluating the mechanical properties of commercial DRA.* JOM, 1993, vol. 45, p. 26-29.

[153] MONGIA, Rajesh K. et BHARTIA, Prakash. *Dielectric resonator antennas—A review and general design relations for resonant frequency and bandwidth.* International Journal of Microwave and Millimeter-Wave Computer-Aided Engineering, 1994, vol. 4, no 3, p. 230-247.

[154] ARAS, M. S. M., RAHIM, M. K. A., ASROKIN, A., et al. *Dielectric resonator antenna (DRA) for wireless application.* In: 2008 IEEE International RF and Microwave Conference. IEEE, 2008. p. 454-458.

[155] MUKHERJEE, Biswajeet, PATEL, Pragati, et MUKHERJEE, Jayanta. *A review of the recent advances in dielectric resonator antennas.* Journal of Electromagnetic Waves and Applications, 2020, vol. 34, no 9, p. 1095-1158.

[156] LEE, Ho Sang et LEE, Mun Soo. *A study on the enhancement of gain and axial ratio bandwidth of the multilayer CP-DRA.* In : Proceedings of Papers 5th European Conference on Circuits and Systems for Communications (ECCSC'10). IEEE, 2010. p. 248-252.

[157] IQBAL, Javed, ILLAHI, Usman, SULAIMAN, Mohamad Ismail, et al. *Bandwidth enhancement and generation of CP by using parasitic patch on rectangular DRA for wireless applications.* IEEE Access, 2019, vol. 7, p. 94365-94372.

[158] WHEELER, Harold A. *The radian sphere around a small antenna*. Proceedings of the IRE, 1959, vol. 47, no 8, p. 1325-1331.

[159] MONGIA, R. K., ITTIPIBOON, A., et CUHACI, M. *Measurement of radiation efficiency of dielectric resonator antennas.* IEEE Microwave and Guided Wave Letters, 1994, vol. 4, no 3, p. 80-82.

[160] KAJFEZ, Darko et KISHK, Ahmed A. *Dielectric resonator antenna-possible candidate for adaptive antenna arrays.* In : Proceedings VITEL 2002, International Symposium on Telecommunications, Next Generation Networks and Beyond. 2002. p. 13-14.

[161] PETOSA, Aldo et ITTIPIBOON, Apisak. *Dielectric resonator antennas: A historical review and the current state of the art.* IEEE antennas and Propagation Magazine, 2010, vol. 52, no 5, p. 91-116.

[162] SOREN, Dipali, GHATAK, Rowdra, MISHRA, Rabindra Kishore, et al. *Dielectric resonator antennas: designs and advances.* Progress In Electromagnetics Research B, 2014, vol. 60, p. 195-213.

[163] LEGIER, J. F., KENNIS, P., TOUTAIN, S., et al. *Resonant frequencies of rectangular dlekctric resonators.* IEEE Transactions on Microwave Theory and Techniques, 1980, vol. 28, no 9, p. 1031-1034.

[164] MONGIA, R. Kumar et ITTIPIBOON, Apisak. *Theoretical and experimental investigations on rectangular dielectric resonator antennas.* IEEE Transactions on antennas and propagation, 1997, vol. 45, no 9, p. 1348-1356.

[165] MOON, Jung-Ick et PARK, Seong-Ook. *Dielectric resonator antenna for dual-band PCS/IMT-2000*. Electronics Letters, 2000, vol. 36, no 12, p. 1.

[166] MONGIA, R. K., ITTIBIPOON, A., et CUHACI, M. *Low profile dielectric resonator antennas using a very high permittivity material*. Electronics letters, 1994, vol. 30, no 17, p. 1362-1363.

[167] MCALLISTER, M. W., LONG, S. Andrew, et CONWAY, G. L. *Rectangular dielectric resonator antenna*. Electronics letters, 1983, vol. 19, no 6, p. 218-219.

[168] LEUNG, Kwok Wa, FANG, X. S., PAN, Y. M., et al. *Dual-function radiating glass for antennas and light covers—Part II: Dual-band glass dielectric resonator*

antennas. IEEE transactions on antennas and propagation, 2012, vol. 61, no 2, p. 587-597.

[169] LEUNG, K. W., LUK, K. M., LAI, K. Y. A., et al. *Theory and experiment of a coaxial probe fed hemispherical dielectric resonator antenna.* IEEE Transactions on Antennas and Propagation, 1993, vol. 41, no 10, p. 1390-1398.

[170] MONGIA, R. Kumar et ITTIPIBOON, Apisak. *Theoretical and experimental investigations on rectangular dielectric resonator antennas*. IEEE Transactions on antennas and propagation, 1997, vol. 45, no 9, p. 1348-1356.

[171] KRANENBURG, R. A. et LONG, S. A. *Microstrip transmission line excitation of dielectric resonator antennas.* Electronics Letters, 1988, vol. 24, p. 1156.

[172] ZHANG, L.-N., ZHONG, S.-S., et XU, S.-Q. *Broadband U-shaped dielectric resonator antenna with elliptical patch feed*. Electronics Letters, 2008, vol. 44, no 16, p. 947-949.

[173] KRANENBURG, Roger A., LONG, Stuart A., et WILLIAMS, Jeffery T. *Coplanar waveguide excitation of dielectric resonator antennas.* IEEE Transactions on Antennas and Propagation, 1991, vol. 39, no 1, p. 119-122.

[174] GHOSH, Bratin, GHOSH, Kunal, et PANDA, Chandra Sekhar. *Coplanar waveguide feed to the hemispherical DRA*. IEEE transactions on antennas and propagation, 2009, vol. 57, no 5, p. 1567-1571.

[175] KISHK, Ahmed A., ITTIPIBOON, A., ANTAR, Y. M. M., et al. *Slot excitation of the dielectric disk radiator*. IEEE Transactions on Antennas and propagation, 1995, vol. 43, no 2, p. 198-201.

[176] LEUNG, Kwok-Wa, LUK, Kwai-Man, LAI, Kin YA, et al. *Theory and experiment of an aperture-coupled hemispherical dielectric resonator antenna*. IEEE Transactions on Antennas and Propagation, 1995, vol. 43, no 11, p. 1192-1198.

[177] PAN, Y. M. et ZHENG, S. Y. *A low-profile stacked dielectric resonator antenna with high-gain and wide bandwidth*. IEEE Antennas and Wireless Propagation Letters, 2015, vol. 15, p. 68-71.

[178] PAN, Y. M. et ZHENG, S. Y. *A low-profile stacked dielectric resonator antenna with high-gain and wide bandwidth.* IEEE Antennas and Wireless Propagation Letters, 2015, vol. 15, p. 68-71.

[179] KISHK, Ahmed A. et HUANG, Wei. *Use of electric and magnetic conductors to reduce the DRA size*. In : 2007 International workshop on Antenna Technology: Small and Smart Antennas Metamaterials and Applications. IEEE, 2007. p. 143-146.

[180] TAM, Matthew et MURCH, Ross David. *Half volume dielectric resonator antenna designs*. Electronics Letters, 1997, vol. 33, no 23, p. 1914-1916.

[181] KISHK, Ahmed A. et HUANG, Wei. *Size-reduction method for dielectric-resonator antennas.* IEEE Antennas and Propagation Magazine, 2011, vol. 53, no 2, p. 26-38.

[182] POZAR, David M. *Microwave engineering*. John Wiley & sons, 20110.

[183] POZAR, David. *Considerations for millimeter wave printed antennas*. IEEE Transactions on antennas and propagation, 1983, vol. 31, no 5, p. 740-747.

[184] RUVIO, Giuseppe, KILDAL, P.-S., et MACI, Stefano. *Modal propagation in ideal soft and hard waveguides.* In : IEEE Antennas and Propagation Society International Symposium. Digest. Held in conjunction with: USNC/CNC/URSI North American Radio Sci. Meeting (Cat. No. 03CH37450). IEEE, 2003. p. 438-441.

[185] ATTIA, Hussein, ABDELGHANI, M. Lamine, et DENIDNI, Tayeb A. *Wideband and high-gain millimeter-wave antenna based on FSS Fabry–Perot cavity*. IEEE Transactions on Antennas and Propagation, 2017, vol. 65, no 10, p. 5589-5594.

[186] KILDAL, P.-S., ZAMAN, Ashraf Uz, RAJO-IGLESIAS, Eva, et al. *Design and experimental verification of ridge gap waveguide in bed of nails for parallel-plate mode suppression.* IET Microwaves, Antennas & Propagation, 2011, vol. 5, no 3, p. 262-270.

[187] ZHANG, Jing, ZHANG, Xiupu, et KISHK, Ahmed A. *Broadband 60 GHz antennas fed by substrate integrated gap waveguides.* IEEE Transactions on Antennas and Propagation, 2018, vol. 66, no 7, p. 3261-3270.

[188] KILDAL, P.-S., ZAMAN, Ashraf Uz, RAJO-IGLESIAS, Eva, et al. *Design and experimental verification of ridge gap waveguide in bed of nails for parallel-plate mode suppression*. IET Microwaves, Antennas & Propagation, 2011, vol. 5, no 3, p. 262-270.

[189] CHEN, Chao, CHEN, Jixin, et HONG, Wei. *Differentially fed dual-polarized 2-D multibeam dielectric resonator antenna array based on printed ridge gap waveguide.* IEEE Transactions on Antennas and Propagation, 2022, vol. 70, no 9, p. 7967-7977.

[190] ZARIFI, Davoud, FARAHBAKHSH, Ali, et ZAMAN, Ashraf Uz. *A gap waveguide-fed wideband patch antenna array for 60-GHz applications.* IEEE Transactions on Antennas and Propagation, 2017, vol. 65, no 9, p. 4875-4879.

[191] EL-DIN, MSH Salah, SHAMS, Shoukry I., ALLAM, A. M. M. A., et al. *Bow-tie slot antenna loaded with superstrate layers for 5G/6G applications.* In : 2021 IEEE

International Symposium on Antennas and Propagation and USNC-URSI Radio Science Meeting (APS/URSI). IEEE, 2021. p. 1561-1562.

[192] H. Attia, M. L. Abdelghani and T. A. Denidni, *Wideband and High-Gain Millimeter-Wave Antenna Based on FSS Fabry–Perot Cavity*, in IEEE Transactions on Antennas and Propagation, vol. 65, no. 10, pp. 5589-5594, Oct. 2017

[193] BAYAT-MAKOU, Nima et KISHK, Ahmed A. *Realistic air-filled TEM printed parallel-plate waveguide based on ridge gap waveguide*. IEEE Transactions on Microwave Theory and Techniques, 2018, vol. 66, no 5, p. 2128-2140.

[194] BAYAT-MAKOU, Nima et KISHK, Ahmed A. *TEM H-plane horn antenna based on TEM printed gap waveguide configuration.* In : 2018 IEEE International Symposium on Antennas and Propagation & USNC/URSI National Radio Science Meeting. IEEE, 2018. p. 1095-1096.

[195] SORKHERIZI, Milad Sharifi, DADGARPOUR, Abdolmehdi, et KISHK, Ahmed A. *Planar high-efficiency antenna array using new printed ridge gap waveguide technology*. IEEE Transactions on antennas and propagation, 2017, vol. 65, no 7, p. 3772-3776.

[196] ALI, Mohamed Mamdouh M., SHAMS, Shoukry I., et SEBAK, Abdel-Razik. *Printed ridge gap waveguide 3-dB coupler: Analysis and design procedure.* IEEE Access, 2017, vol. 6, p. 8501-8509.

[197] ATTIA, Hussein. *Analytical Prediction of the Radiation Characteristics of 2*2 Ridge Gap Waveguide Slot Antenna Array With Suppressed Grating Lobes at the V-band*. IEEE Access, 2019, vol. 7, p. 95132-95139.

[198] DESLANDES, Dominic et WU, Ke. *Single-substrate integration technique of planar circuits and waveguide filters*. IEEE Transactions on microwave theory and Techniques, 2003, vol. 51, no 2, p. 593-596.

[199] KILDAL, Per-Simon, ALFONSO, E., VALERO-NOGUEIRA, A., et al. *Local metamaterial-based waveguides in gaps between parallel metal plates.* IEEE Antennas and wireless propagation letters, 2008, vol. 8, p. 84-87.

[200] BRAZALEZ, Astrid Algaba, ZAMAN, Ashraf Uz, et KILDAL, Per-Simon. *Improved microstrip filters using PMC packaging by lid of nails.* IEEE Transactions on Components, Packaging and Manufacturing Technology, 2012, vol. 2, no 7, p. 1075-1084.

[201] RAJO-IGLESIAS, Eva et KILDAL, P.-S. *Numerical studies of bandwidth of parallel-plate cut-off realised by a bed of nails, corrugations and mushroom-type*

electromagnetic bandgap for use in gap waveguides. IET microwaves, antennas & propagation, 2011, vol. 5, no 3, p. 282-289.

[202] MUKHERJEE, Soumava, BISWAS, Animesh, et SRIVASTAVA, Kumar Vaibhav. *Bandwidth enhancement of substrate integrated waveguide cavity backed slot antenna by offset feeding technique.* In : 2013 IEEE Applied Electromagnetics Conference (AEMC). IEEE, 2013. p. 1-2.

[203] SERHSOUH, Imane, HIMDI, Mohamed, et LEBBAR, Hassan. *Design of coplanar slotted SIW antenna arrays for beam-tilting and 5G applications.* IEEE Antennas and Wireless Propagation Letters, 2019, vol. 19, no 1, p. 4-8.

[204] DADGARPOUR, Abdolmehdi, ZARGHOONI, Behnam, VIRDEE, Bal S., et al. *Beam tilting antenna using integrated metamaterial loading.* IEEE Transactions on Antennas and Propagation, 2014, vol. 62, no 5, p. 2874-2879

[205] SIFAT, Syed M., ALI, Mohamed Mamdouh M., SHAMS, Shoukry I., et al. *High gain bow-tie slot antenna array loaded with grooves based on printed ridge gap waveguide technology*. IEEE Access, 2019, vol. 7, p. 36177-36185

[206] M. M. M. Ali, I. Afifi and A. -R. Sebak, *A Dual-Polarized Magneto-Electric Dipole Antenna Based on Printed Ridge Gap Waveguide Technology*. in IEEE Transactions on Antennas and Propagation, vol. 68, no. 11, pp. 7589-7594, Nov. 2020

[207] DADGARPOUR, Abdolmehdi, BAYAT-MAKOU, Nima, ANTONIADES, Marco A., et al. *A dual-polarized magnetoelectric dipole array based on printed ridge gap waveguide with dual-polarized split-ring resonator lens.* IEEE Transactions on Antennas and Propagation, 2020

[208] ATTIA, Hussein, KISHK, Ahmed A., ABDALLA, Mahmoud A., et al. *Ridge gap waveguide antenna array with improved mutual isolation for millimeter wave applications.* International Journal of RF and Microwave Computer-Aided Engineering, 2021, vol. 31, no 11, p. e22831.

[209] SUN, Liangyu, ZAMAN, Ashraf Uz, YAN, Binyun, et al. *High-efficiency single-layer corporate-feed gap waveguide based circularly polarized antenna array with compact size.* AEU-International Journal of Electronics and Communications, 2024, p. 155341.

[210] YI, Hao, MU, Yajie, HAN, Jiaqi, et al. *Broadband millimeter-wave metasurface antenna array with printed ridge gap waveguide for high front-to-back ratio.* Journal of Information and Intelligence, 2023, vol. 1, no 1, p. 11-22.

[211] XIAO, Jun, TIAN, Jin, DING, Tongyu, et al. *A high-gain circularly polarized magnetoelectric dipole antenna array with metallic radiating structure for millimeter-wave applications.* Materials & Design, 2024, vol. 242, p. 112983.

[212] LIU, Zheng, QI, Shi-Shan, YU, Yingrui, et al. *W-band single-layer circularly-polarised antenna based on compact gap waveguide.* IET Microwaves, Antennas & Propagation, 2024.